Salt Transport Experiments in Fractured Media

Ibrahim Daher

Department of Chemical Engineering

Qatar Carbonates and Carbon Storage Research Centre

Imperial College London

London SW7 2AZ

United Kingdom

A dissertation submitted in fulfilment of the

requirements for the degree of Doctor of Philosophy of

Imperial College London

November, 2016

Declaration

I declare that this thesis,

Salt Transport Experiments in Fractured Media

is entirely my own work under the supervision of Dr. John Crawshaw, Prof. Geoffrey Maitland and Prof. Martin Trusler. This work was performed in the Department of Earth Science and Engineering at Imperial College London.

All published and unpublished materials used in the thesis have been given full acknowledgment. This work has not been previously submitted, in a whole or in part, to any other academic institution for a degree, diploma or any other qualification.

Ibrahim Daher

Department of Chemical Engineering

Imperial College London

January 29th 2017

Copyright Statement

‘The copyright of this thesis rests with the author and is made available under a Creative Commons Attribution Non-Commercial No Derivatives licence. Researchers are free to copy, distribute or transmit the thesis on the condition that they attribute it, that they do not use it for commercial purposes and that they do not alter, transform or build upon it. For any reuse or redistribution, researchers must make clear to others the licence terms of this work’.

Abstract

During the sequestration of CO_2 into down-hole rock formations, salt precipitation may occur due to the drying of the formation brine if the injected CO_2 is dry. This can negatively affect the performance of injection wells and can even lead to well clogging, which is a serious risk for such operations. Further, the salt deposition can alter the flow of the CO_2 in the formation altering the storage capacity. Therefore, it is very important to explore the effect on CCS (Carbon Capture and Storage) process of drying out and salt precipitation during CO_2 injection. This study is focused on CCS in fractured aquifers, which has received less attention than their un-fractured counterparts and particularly, the flow impairment associated with salt precipitation during the injection of dry CO_2. When CO_2 is injected into a conductive fracture network, the brine will rapidly be displaced from the fractures near the point of injection and the subsequent mass transfer between the matrix and the fracture; orthogonal to the flow direction in the fracture, is the major target of the project. The dry-out that occurs due to the evaporation of water from the brine filled region of the matrix into the under-saturated CO_2 filling the fracture can cause deposition of salt in the matrix or the fracture, locally reducing permeability.

This thesis reports on an investigation of the evaporative drying kinetics and salt precipitation using a combination of gravimetric and X-ray μ-CT techniques to measure the water and brine saturation, salt precipitation and distribution of salt deposition in two rocks; a sandstone, Bentheimer and a carbonate, Ketton.

Based on the experimental results for de-ionised water, two main regimes occur during the dry-out process: a capillarity driven regime which seems to be dominant for most of the dry-out process in the experiments, during which evaporation happens only at the surface of the fracture, followed by a diffusion limited regime after the liquid bridge to the surface breaks and pores near the surface become dry for the first time. In pure water, this results in an almost constant evaporation flux in the first regime followed by a mass loss that is linear when plotted against the square root of time. The experiments with brine were initially similar with an evaporative flux almost constant with time. However, a short time into the process the evaporative flux started to decrease approximately linearly with the square root of time, following the deposition of salt at the surface of the fracture.

At the end of gravimetric dry-out tests, μ-CT images were obtained showing that salt was mainly precipitated at the surface of the sample; however, relatively small amount of salt was

observed precipitated in the interior of the sample. The pore structure of the precipitated salt at the end of the dry-out tests maintained connectivity between the surface of the deposit and the rock matrix.

Dynamic μ-CT imaging of Bentheimer during brine drying showed that during the early stage of evaporation, salt was continuously deposited at the surface of the matrix. During this stage in the evaporation of brine, advection dominates the transport of dissolved salt, indicated by a large Peclet number, and this resulted in an increased salt concentration very local to the site of evaporation. The ongoing formation of an efflorescence therefore, is evidence for the continuity of the liquid connections to the outside of the sample, despite the evaporation becoming linear against the square root of time. Unfortunately, the liquid bridges to the surface were too small to be seen directly in the μ-CT imaging.

The volume of precipitated salt increased with time and this resulted in a change in the pore structure at the surface of the sample structure, consequently reducing the brine-drying rate. However, as the salt deposition and therefore the location of the evaporation continued to be at the exposed surface, vapour diffusion cannot account for the mass lost by evaporation becoming linear in the square root time as is usually stated. Some other mechanism must account for the observed behaviour and we speculate that the surface area for evaporation was reduced by the appearance of dry patched on the surface.

At a very late stage of evaporation, it was observed that no further salt precipitated at the surface of the sample; and subsequently, salt precipitation progressed with time towards the interior of the sample core with small amount of salt. At this stage the liquid connection to the surface must finally have broken and a true diffusion controlled process occurred. In the limited sample size used in this study, this mechanism accounted for only a small fraction of the total salt deposited.

From permeability measurements before and after the complete drying of the samples, it was demonstrated that the permeability of Bentheimer was reduced by 81 % from 2.2 D to 0.41 D by the salt deposition. However, Lattice Boltzmann simulations of single phase permeability in the segmented μ-CT images, showed a reduction by 54% from 2.27 D to 1.28 D at 6 μm scanned voxel resolution and 54% from 2.7D to 1.48D at 15um scanned voxel resolution. From these results, it can be concluded that salt precipitation during the injection of CO_2 into a fractured porous medial result in a significant reduction in formation permeability, but connectivity between the matrix and the fracture is maintained.

Acknowledgements

In the Name of Allah, most gracious and most merciful, by whom I would like to start my words with.

Firstly, I would like to express my sincere gratitude to my supervisor, Dr. John Crawshaw, for the assistance, continuous encouragement and support throughout the years of my PhD journey. He has been a tremendous mentor for me for allowing me to grow as a research scientist in the past four years. In addition, his guidance helped me in all the time of research, writing and his inspiring suggestions have been precious for the development of this thesis. John had confidence in me when I doubted myself as he was always believing in my work. Whenever he is free, his door is open to meet, talk, and discuss the ideas. Of the many great advices, I have learned from him is that to progress, I must leave room for doubt about science. This advice allowed me to question, explore, and research from different perspectives.

I thank Prof. Geoffrey Maitland, my second supervisor for his trust, offering valuable advice, his patience and guidance during the paperwork process. Thank you for your insightful discussions and spiritual support. He taught me how to fulfil a PhD work that I am today proud of.

I have great pleasure to thank the lab assistants Alexander Toth and Norman Nicholls, for their kind help in fulfilling my lab needs, supplies and providing me the proper lab tools to build the rig during the period of my research. You made the lab's atmosphere as friendly as possible.

A special thanks to my colleagues. The source of daily inspiration and joy during this research. Thank you for your support, encouragement, enthusiasm and love.

Many thanks to my employer, Qatar Petroleum, who granted me this opportunity to develop in my career path providing me the continuous overseas support in all forms and aspects. Without such an opportunity, I would not be able to move on and achieve my goals as a researcher and a petroleum engineer.

A special thanks to my family. Words can't express how grateful I am to both my parents, for their sacrifices and heartfully prayers in every step of my journey. Those prayers for me were what sustained me this far. I can't forget my beloved daughter, Laura, whom her presence in my life is the reason to cheer me up through hard moments and days of this journey.

My last thanks but not least goes to the rest of my family, brother and sisters, as well as my friends, for their encouragement throughout this journey and support through all the difficulties.

Contents

Declaration 1
Copyright Statement 2
Abstract 3
Acknowledgements 5
Contents 7
List of Figures 9
List of Tables 17
1 Introduction 18
1.1 Background 18
1.1.1 Carbon Dioxide Emissions and Climate Change 18
1.1.2 CO_2 Capture and Storage 22
1.1.3 CO_2 Trapping Mechanisms 24
1.1.4 Current and Planned CC Projects in Saline Aquifers 25
1.2 Research Motivation 27
1.3 Thesis Objectives 27
1.4 Thesis Structure 28
2 Review of Evaporation and Salt Precipitation from Porous Media 30
2.1 Evaporation Process from Porous Media 30
2.1.1 Boundary Conditions and Dry-out Regimes from Porous Media 30
2.1.2 The Effect of Salinity on Dry-out Periods 52
2.2 Chapter Summary 65
3 Experimental Set-up 67
3.1 Rocks Characterisation and Fluids Properties 67
3.2 Experimental Set-up and Test Procedures 70
3.2.1 Gravimetric Based Dry-out Experiment 71
3.2.2 µ-CT Based Dry-out Experiment 74
3.3 Micro- Computed Tomography Imaging and Image Processing 76
3.3.1 Image Processing 78
3.3.2 Image processing routine: 6 µm data 80
3.3.3 Image processing routine: 15 µm data 84
4 Evaporation and Salt Precipitation: Results and Discussions 86
4.1 Gravimetric Dry-out Tests Results and Discussions 86
4.1.1 Gravimetric Evaporation Tests Matrix 86
4.1.2 Dry-out during Evaporation of Pure De-ionised Water Results and Discussions 87
4.1.3 Dry-out during Evaporation of Brine Results and Discussions 97

4.2 In situ μ-CT Images Analysis for Dry-out and Salt Precipitation 111
4.2.1 μ-CT Image Analysis for De-ionised Water Dry-out at 6 μm voxel size 112
4.2.2 μ-CT Image Analysis for Brine with 6.4 Molal at 6 μm voxel size 114
4.2.3 μ-CT Image Analysis for Brine with 6.4 Molal at 15 μm voxel size 118
4.3 Pore-scale modelling 122
4.3.1 Network modelling 126
5 Conclusions and Recommendations 128
5.1 Conclusions 128
5.2 Recommendations 132
6 Bibliography 133

List of Figures

Figure 1-1 CO_2 Concentration (ppm) with time (year) (Blunt, 2010) 19

Figure 1-2 The trend of CO_2 Concentration and Temperature Anomaly (the departure from a reference value of long term average) from 1950-2011 (El-Maghraby, 2013)..... 19

Figure 1-3-CO_2 Phase behaviour (Gunter et al., 1997; Moore & Slobod, 1955)..... 22

Figure 1-4 Source for which CCS might be Relevant (Metz et al., 2005)..... 23

Figure 1-5-CO_2 Storage Options (Metz et al., 2005)..... 24

Figure 1-6 Location of sites where activities relevant to CO_2 storage are planned or under way (Metz et al., 2005)..... 25

Figure 2-1 Sketch of the thick liquid films in a capillary tube of square cross section and drying periods by Chauvet et al., (2009)..... 32

Figure 2-2 Column packed with sand with an average particle size of 0.224 mm to determine the onset of stage 2 (Shokri & Or, 2011) 34

Figure 2-3 Conceptual diagram of first-stage evaporation by Lehmann et al., (2008)..... 36

Figure 2-4 Schematic of test and the location of evaporation and percolation fronts by Yiotis et al., (2012)..... 37

Figure 2-5 Experimental results for a typical drying curve in the 30-cm-long tube for a packing of 150–200 μm beads saturated with pentane (Yiotis et al., 2012). 38

Figure 2-6 Liquid saturation with time (data point in this figure was obtained from 2-D drying tests from Laurindo and Prat (1998)..... 39

Figure 2-7 Schematic of the drying problem considered and characteristics drying regime by Yiotis et al., (2006) 41

Figure 2-8 Experimental procedures to study the drying-out of a sandstone core under a continuous flux of gas by André et al., (2014) 43

Figure 2-9- Slices of CT images of the homogeneous Bentheimer sandstone (a) prior to and (b) post experiment and (c) 3D representation of dry core and precipitated salt. Precipitated salt is represented by the white color, gray represents the soil matrix and gas is shown by the black color by Roels et al., (2014) 45

Figure 2-10- Salt precipitation profile along the core after dry-out (Roels et al., 2014)..... 46

Figure 2-11 CT scan imaging for Brine saturation at different times obtained for short

Bentheimer core by Roels et al., (2016). The brine saturation represents both the presence of brine and solid salt. After 15.5 h of injection, complete clogging of the injection well can be observed (dark red)..... 47

Figure 2-12 CT scan images at various times for a homogeneous Bentheimer core and b layered Bentheimer and Berea core (Roels et al., 2016)..... 47

Figure 2-13 Post experiment μ-CT scans taken at 0.8 cm from the top from a short Bentheimer core and b layered core by Roels et al., (2016). White color represents higher density (solid salt) and black color represents lower density (CO_2). Solid salt was found a accumulated around the injection well and b distributed along the domain..... 48

Figure 2-14 Pressure drop vs. time for three experiments by Roels et al., (2016) 49

Figure 2-15 Schematic of the experimental setup by (Ott et al., 2015) and more details are provided in (Ott et al., 2012)..... 50

Figure 2-16 μ-CT data recorded with pseudo pore-scale resolution during CO_2 flooding by Ott et al., (2015)..... 51

Figure 2-17 Microscopic model of fluxes controlling the precipitated salt location by Ott et al., (2015) 52

Figure 2-18 Spatial distribution of salt precipitation (NaCl) in heterogeneous half-divided column. The white material is the precipitated salt. The fine-textured half is fully covered with salt, while the coarse half is still visible by Nachshon et al., (2011a) 54

Figure 2-19 Salt precipitations in homogenous columns at low (a) and high evaporation rates by Nachshon et al., (2011b) 55

Figure 2-20 2D Average water saturation versus time for convective and diffusive drying test by Peysson et al., (2011) 56

Figure 2-21 Drying rate ξ (kg m-2 hr-1) versus average water saturation for convective and diffusive drying test by Peysson et al., (2011) 57

Figure 2-22 Drying rate in kg m-2 h-1 versus average saturation in the diffusion-driven..... 57

Figure 2-23 (a) Cumulative precipitated salt as a function of the cumulative mass of liquid water lost by evaporation. The legend indicates the initial salt concentration in each evaporating sand column. (b) Time dependence of the cumulative precipitated salt in each sand column by Norouzi Rad et al., (2013) 59

Figure 2-24 The SEM images of the evolution structural of the salt precipitation at the surface of the sample for NaCl solution of 3.5 Molal and that after after (left) 18 hours and (right) 168 hours with magnification factors of (a) and (b) 150, (c) and (d) 500 and (e) and (f)

2000 by Norouzi Rad et al., (2013)..... 59

Figure 2-25 Normalized water content at time t (mt/mt0) as a function of time (min) for different sample sizes (large, medium, and small) at two different relative of: (RH =20% and 50%) (Desarnaud et al., 2015) 60

Figure 2-26 Zooming in SEM microphotographs of salt crystals at the surface of sandstone at the end of drying of sandstone saturated with salt solution (Desarnaud et al., 2015)..... 61

Figure 2-27 Examples of efflorescence at the end of drying process for salt concentration equals to 25%: (a) range #1 (5–50 μm), (b) range #6 (300 μm) by Eloukabi et al., (2013) .. 62

Figure 2-28 Examples of evolution of evaporated mass as a function of time by Eloukabi et al., (2013). (a) bead size ranges from (5-50μm) (crusty) and (b) bead size ranges from (50-62μm) (patchy) (C_o is salt concentration) 63

Figure 2-29 Crust and patchy efflorescence patterns obtained by changing the size of the beads forming the porous medium by Veran-Tissoires & Prat (2014)..... 65

Figure 3-1 Two dimensional cross sections of three dimensional micro-CT images of samples. (a) Bentheimer sandstone. (b) Ketton carbonate..... 68

Figure 3-2 a) MICP curve for Bentheimer sandstone. b) Pore throat radii distribution based on measurements of mercury injection capillary pressure (Andrew, 2015)..... 69

Figure 3-3 MICP curve for Kenton carbonate. b) Pore throat radii distribution based on measurements of mercury injection capillary pressure (Andrew, 2015)..... 70

Figure 3-4 Examples of drilled cylindrical Bentheimer sandstone..... 71

Figure 3-5 Schematic flow diagram representing the apparatus for gravimetric based dry-out experiments 72

Figure 3-6 Photo represents the oven with equipped desiccator and micro-fan used for drying out test. 73

Figure 3-7 Schematic representation of highly sensitive experimental apparatus for in situ image based dry-out experiments 74

Figure 3-8 Schematic Details of specially made end metal fitting with dual inlet..... 75

Figure 3-9 (a) Image of laboratory based Zeiss Versa XRM-500 at Department of Chemical Engineering, Imperial College, London. This micro-CT imaging facility is used in this study. (b) The core holder is mounted on the stage in between the source and detector inside the lead x-ray enclosure..... 77

Figure 3-10 Schematic representation of principle of X-ray micro-computed tomography ... 77

Figure 3-11 Image processing of the dry rock sample. (a) Two-dimensional vertical cross-section of a raw image. Here, black and grey represent pores and rock respectively. (b) Filtered image using nonlocal means edge-preserving filter. (c) Two-phase segmented image with dark blue and light blue as pores and rock respectively..... 81

Figure 3-12 Three- and four-phase segmentation. (a) & (b) Filtered image of the air-brine-rock (3-phase) and air-brine-rock-salt (4-phase) systems respectively. (c) & (d) Segmented images of Figure 3.12 (a) & Figure 3.12 (b) respectively. 82

Figure 3-13 Brine layer correction. (a) Filtered image. (b) 3-phase segmented image with unwanted brine layer. (c) Isolated brine phase. (d) Brine and Air after rock and brine dilation. (e) Isolated air phase. (f) Final corrected image. 83

Figure 3-14 Disconnected brine cluster analysis. The brine from Figure 3.12 (c) was isolated, and the disconnected brine clusters were labelled with different colours and label values. . 84

Figure 3-15 Image processing routine for 15 μm dataset. (a) Two-dimensional vertical cross-section of a filtered image containing air (black), brine (dark grey) and rock (light grey). (b) Three-phase segmented image. Here red, green and blue represent air, brine and rock phases respectively. The white dotted box indicates the region where a subset was taken for comparison with the 6 μm dataset..... 85

Figure 4-1 Cumulative mass loss of De-ionised water for different Bentheimer sandstones porosities with time (hrs) at different air temperatures 88

Figure 4-2 Saturation of De-ionised water for Bentheimer sandstone at different air temperatures..... 89

Figure 4-3 Saturation of de-ionised water in Bentheimer sandstone at 90 °C and 95 °C air temperatures in different sample dimensions as in Table 4-2..... 90

Figure 4-4 Average saturation of de-ionised water in Bentheimer at different air temperatures in different samples dimensions as in Table 4-2..... 91

Figure 4-5 Average cumulative mass loss of De-ionised water for for Bentheimer samples of different length at temperature 60°C, RH~0% 92

Figure 4-6 Zoom in average cumulative mass loss of De-ionised water for Bentheimer samples of different length at temperature 60°C, RH~0% 93

Figure 4-7 Average saturation of de-ionised water for Bentheimer samples of different length at temperature 60°C, RH~0% 93

Figure 4-8 Average saturation of de-ionised water for different Bentheimer porosities with square root of time (hrs) for different samples dimensions at temperature 60°C, RH~0% ... 94

Figure 4-9 Cumulative mass loss of de-ionised water for Bentheimer sandstone and Ketton carbonate with time (hrs) for 80mm sample length at temperature 60°C and 12mm diameter, RH~0% 95

Figure 4-10 Average saturation of De-ionised water for Bentheimer sandstone and Ketton carbonate with time (hrs) for 80mm sample length at temperature 60°C and 12mm diameter 96

Figure 4-11 Average saturation for de-ionised water with square root of time for Bentheimer and Ketton samples for 80mm sample length at temperature 60°C, RH~0%..... 97

Figure 4-12 Average cumulative loss for Bentheimer for De-ionised water, Brine (3.0 Molal and 6.4 Molal) with time (hrs) for 40mm sample length at temperature 60°C and 12mm diameter, RH~0%..... 98

Figure 4-13 Zoom in Bentheimer cumulative loss for De-ionised water, Brine (3.0 Molal and 6.4 Molal) with time (hrs) for 40mm sample length at temperature 60°C and 12mm diameter, RH~0% 99

Figure 4-14 Average saturation for De-ionised water, 3.0 Molal and 6.4 Molal with time [hrs] for 40mm sample length at temperature 60°C and 12mm diameter..... 100

Figure 4-15 Evaporation flux for de-ionised water, Brine (3 Molal and 6.4 Molal) versus average saturation for 40mm sample length at temperature 60°C and 12mm diameter, RH~0% 102

Figure 4-16 Evaporation flux for de-ionised water, Brine (3 Molal and 6.4 Molal) versus vapour pressure for 40mm sample length at temperature 60°C and 12mm diameter, RH~0% 102

Figure 4-17- µ-CT images for Bentheimer for Brine (6.4 Molal) at the end of the Dry-out Test (250hrs) for 40mm sample length at air temperature 60°C and 12mm diameter 103

Figure 4-18 µ-CT raw images (at 2 µm voxel size) for precipitated salt for Bentheimer for 6.4 Molal brine concentration for 40mm sample length at temperature 60°C and 12mm diameter, RH~0% (white is salt)..... 104

Figure 4-19 µ-CT segmented images at 2 µm voxel size for Bentheimer for precipitated salt for 6.4 Molal brine concentration for 40mm sample length at temperature 60°C and 12mm diameter, RH~0%..... 105

Figure 4-20 Average saturation for de-ionised water, Brine (3.0 Molal and 6.4 Molal) versus square root of time for 40mm sample length at temperature 60°C and 12mm diameter 106

Figure 4-21 Average cumulative loss for Ketton for De-ionised water, Brine (3.0 Molal and

6.4 Molal) with time (hrs) for 40mm sample length at temperature 60°C and 12mm diameter, RH~0% 107

Figure 4-22 Average saturation for Ketton for De-ionised water, Brine (3.0 Molal and 6.4 Molal) with time (hrs) for 40mm sample length at temperature 60°C and 12mm diameter, RH~0% 108

Figure 4-23 Zoom in average saturation for Ketton for De-ionised water, Brine (3.0 Molal and 6.4 Molal) with time (hrs) for 40mm sample length at temperature 60°C and 12mm diameter, RH~0% 108

Figure 4-24 Average saturation for Ketton for de-ionised water, Brine (3.0 Molal and 6.4 Molal) with square root of time (hrs) for 40mm sample length at temperature 60°C and 12mm diameter, RH~0% 109

Figure 4-25 Average saturation for Ketton and Bentheimer for Brine (3.0 Molal and 6.4 Molal) with time (hrs) for 40mm sample length at temperature 60°C and 12mm diameter, RH~0% 109

Figure 4-26 μ-CT segmented images at 2 μm voxel size for Ketton carbonate for precipitated salt for 6.4 Molal brine concentration for 40mm sample length at temperature 60°C and 12mm diameter, RH~0% 110

Figure 4-27 Dynamic 6 μm voxel size Image with time for Bentheimer for De-ionised water in 40mm sample length with 12mm diameter at 60°C air temperature and RH~0% near the surface 112

Figure 4-28 Saturation profile versus sample distance from the surface with time [hrs] using μ-CT dynamic images for De-ionised water for Bentheimer in 40mm sample length with 12mm diameter at 60°C air temperature and RH~0% 113

Figure 4-29 Average saturation comparison between μ-CT images and gravimetric test for Bentheimer for De-ionised water with time [hrs] in 40mm sample length with 12mm diameter at 60°C air temperature and RH~0% 113

Figure 4-30 Brine (6.4 Molal) saturation and salt precipitation volume versus distance from exposed face with time using μ-CT dynamic images at 6 μm voxel size for Bentheimer in 40mm sample length with 12mm diameter at 60°C air temperature and RH~0% 114

Figure 4-31 Precipitated salt of 6.4 Molal NaCl solution at different time steps using μ-CT dynamic images at 6 μm voxel size for Bentheimer at 60°C air temperature and RH~0%. (Dark blue: grains, Red: pore phase, light blue: salt and green: brine solution) 115

Figure 4-32 Precipitated salt of 6.4 Molal NaCl solution at different time steps using μ-CT

dynamic images at 6 μm voxel size for Bentheimer at 60°C air temperature and RH~0%. (Dark blue: grains, Red: pore phase, light blue: salt and green: brine solution) 115

Figure 4-33 Precipitated salt of 6.4 Molal NaCl solution at the surface of the sample with different time steps using μ-CT dynamic images at 6 μm voxel size for Bentheimer in 40mm sample length with 12mm diameter at 60°C air temperature and RH~0%. (Dark blue: grains, Red: pore phase, light blue: salt and green: brine solution) 116

Figure 4-34 μ-CT images at 6 μm voxel size for the evolution of salt precipitated (light blue 39.7hrs, dark blue 67 and red & 85.5 hrs) and pore continuity for 6.4 Molal NaCl solution for Bentheimer 117

Figure 4-35 Brine (6.4 Molal) saturation and salt precipitation volume versus distance from exposed face with time using μ-CT dynamic images at 15 μm for Bentheimer in 40mm sample length with 12mm diameter at 60°C air temperature and RH~0% 119

Figure 4-36 Precipitated salt of 6.4 Molal NaCl solution different time steps using μ-CT dynamic images at 15 μm voxel size for Bentheimer in 40mm sample length with 12mm diameter at 60°C air temperature and RH~0%. (Dark blue: grains, Red: pore phase, light blue: salt and green: brine solution) 120

Figure 4-37 The evolution of salt Precipitated 6.4 Molal NaCl solution at the surface of the sample with different time steps using μ-CT dynamic images at 15 μm voxel size for Bentheimer. At 29.4hrs (light blue), at 41.6hrs (dark blue), at 54.6hrs (in red) and at 111hrs (in green) 121

Figure 4-38 2D segmented (xz orientation) slice of 3D pore-scale image of Bentheimer sandstone acquired at 15 μm voxel resolution during the dry-out experiments. (a) Sub-volume (668 x 128 x 110 voxels) to calculate salt layer LB single phase permeability. (b) Sub-volume (500 x 500 x 500 voxels) to calculate matrix LB single phase permeability. The dark blue represents grain phase, light blue represents salt deposition and red colour represents pore phase. 122

Figure 4-39 2D segmented (xz orientation) slice of 3D pore-scale image of Bentheimer sandstone acquired at 6 μm voxel resolution during the dry-out experiments. (a) Sub-volume (500 x 500 x 110 voxels) to calculate salt layer LB single phase permeability. (b) Sub-volume (500 x 500 x 500 voxels) to calculate matrix LB single phase permeability. The dark blue represents grain phase, light blue represents salt deposition and red colour represents pore phase. 123

Figure 4-40 2D binary (xz orientation) slice of 3D pore-scale image of Bentheimer sandstone acquired at 15 μm resolution for LB single phase permeability simulation. (a) Sub-volume to

calculate salt layer permeability (b) Sub-volume to calculate matrix permeability. The black colour represents pore space and white colour represents grain + salt deposited. 124

Figure 4-41 Calculated LB single phase permeability for Bentheimer sandstone scanned at 6 µm voxel resolution. (a) Matrix permeability and (b) Salt layer permeability 124

Figure 4-42 Calculated LB single phase permeability for Bentheimer sandstone scanned at 15 µm voxel resolution. (a) Matrix permeability and (b) Salt layer permeability. 125

Figure 4-43 Frequency distribution of Bentheimer sandstone scanned at 6 µm voxel resolution. (a) Pore radius and (b) Throat radius. 127

Figure 4-44 Frequency distribution of Bentheimer sandstone scanned at 15 µm voxel resolution. (a) Pore radius and (b) Throat radius. 127

List of Tables

Table 1-1 Summary of CO_2 Reduction Strategies (Leung et al., 2014)..... 21

Table 1-2 Summarise the Current and Planned Projects of CO_2 in Saline Aquifers (Leung et al., 2014)..... 26

Table 3-1 Basic information about each rock type..... 68

Table 3-2 Basic petrophysical properties and chemical composition of each rock type 68

Table 4-1-Gravimetric dry-out tests series..... 86

Table 4-2-Bentheimer Sandstone characteristics and sample dimensions..... 87

Table 4-3-Bentheimer Sandstone characteristics and sample dimensions..... 91

Table 4-4 Pore space network properties of Bentheimer sandstone for selected matrix sub-volume scanned at 6 μm voxel resolution. 126

Table 4-5 Pore space network properties of Bentheimer sandstone for selected matrix sub-volume scanned at 15 μm voxel resolution..... 127

Chapter 1

1 Introduction

This chapter provides background on the CO_2 capture and storage (CCS) process, including carbon dioxide emission and its impact on climate change, CO_2 sequestration and geological storage type and a brief summary of CO_2 trapping mechanism and CO_2 CCS projects is given here. Finally, this chapter includes the thesis key objectives and thesis structure.

1.1 Background

1.1.1 Carbon Dioxide Emissions and Climate Change

The growth in population and economy is the key driver for the severe demand in energy. Between 2010 and 2035, the world population will likely increase from 6.8 billion to 8.6 billion, which means additional 1.6 billion people, will need energy (Falkowski et al., 2000; Orr Jr, 2004; Solomon et al., 2007). An obvious consequence of the population growth is an increase in the usage of fuel, particularly conventional fossil fuels such as coal, oil and natural gas. The excessive fuel burning will result in a severe increase in the emission of CO_2.

Figure 1-1 shows the predicted and measured atmospheric carbon dioxide concentrations. The dashed line from 1980 to 2008 is the concentration measured in Hawaii (Blunt, 2010). The solid line is a prediction based on past and possible future use of fossil fuels. The coloured lines indicate the contributions of oil, gas and coal. This assumes that half the CO_2 generated when the fuel is burnt remains in the atmosphere—the other half dissolves in the sea or is absorbed by the land surface and terrestrial biosphere. Until 2008, the estimated total contribution of fossil fuel matches the measured rise in concentration. 2008 is taken as a baseline and predictions of future concentrations are based on current trends in production.

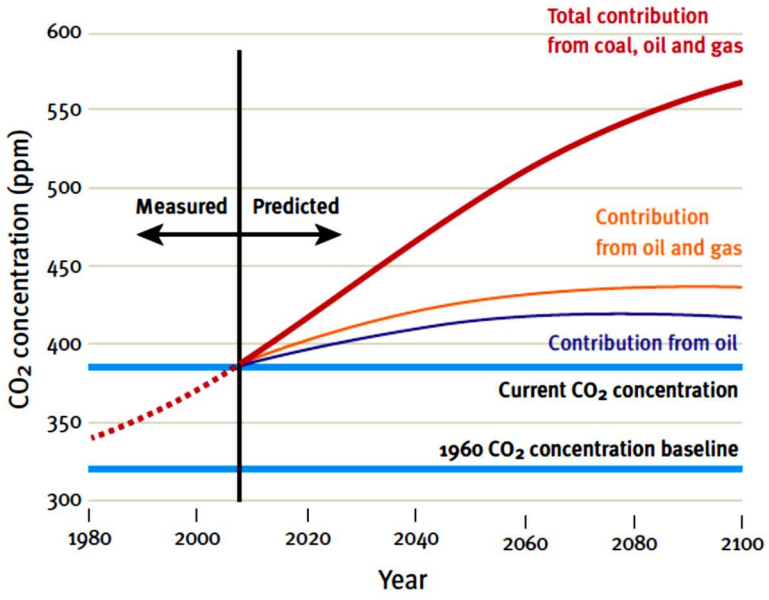


Figure 1-1 CO_2 Concentration (ppm) with time (year) (Blunt, 2010)

The global average temperature is greatly influenced by number of factors including the greenhouse gases; however amongst the greenhouse gases, CO_2 has the greatest influence (Falkowski et al., 2000; Orr Jr, 2004; Solomon et al., 2007). Studies have demonstrated that increasing atmospheric CO_2 concentration (ppm) is correlated to mean global temperature increases, Figure 1-2.

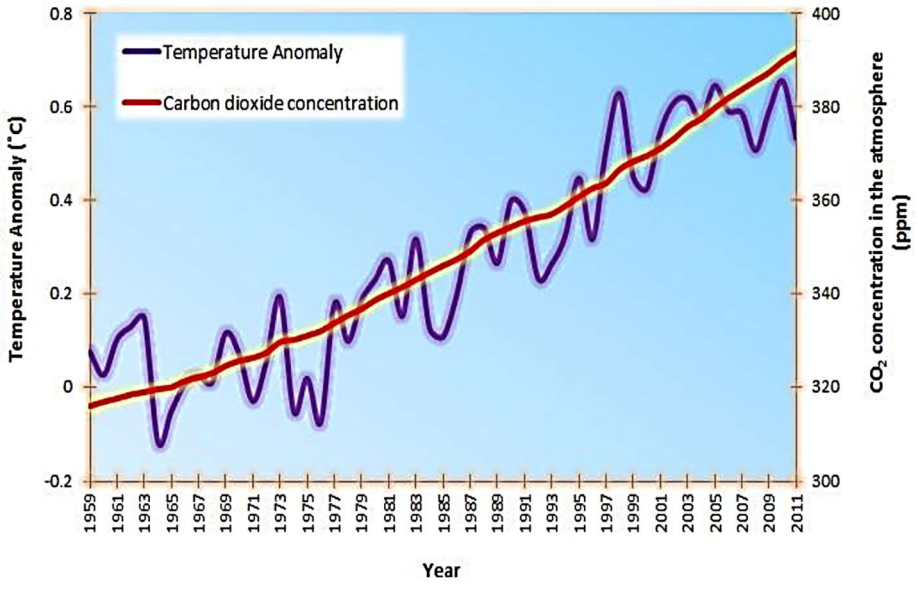


Figure 1-2 The trend of CO_2 Concentration and Temperature Anomaly (the departure from a reference value of long term average) from 1950-2011 (El-Maghraby, 2013)

Recent investigations have shown that inconceivable catastrophic changes in the environment will take place if the global temperatures increase by more than 2° C (3.6° F). A warming of 2° C (3.6° F) corresponds to a carbon dioxide (CO_2) concentration of about 450 ppm (parts per million) in the atmosphere. As of beginning of 2007, the CO_2 concentration was already at 380 ppm and it is increasing on average 2 - 3 ppm each year, so that the critical value will be reached in approximately 20 to 30 years from now (Tans & Keeling, 2010). It is predicted that unless the atmospheric CO_2 concentration is stabilised or even reduced the consequences of the associated changes to the earth's climate system could be severe. Therefore, aggressive cuts to CO_2 emissions are required to achieve this (Hoffert et al., 2002; Wigley et al., 1996). However, reducing the emission of the CO_2 significantly encounters with several challenges including;

- The emissions of carbon dioxide result mainly from fossil fuel combustion and 85% of primary power demand is met by burning fossil fuels.
- Stabilising the earth's atmospheric CO_2 concentration at 550 ppm (roughly double the level before the industrial revolution) would require global energy sources in 2050 capable of zero carbon emissions to be equal in magnitude to current global energy supplies in their entirety (Wigley et al., 1996).

Several approaches have been considered and implemented by various countries in order to reduce or stabilise CO_2 emissions, including;

- Improve energy efficiency and promote energy conservation.
- Increase usage of low carbon fuels, including natural gas, hydrogen or nuclear power.
- Deploy renewable energy, such as solar, wind, hydropower and bioenergy.
- Apply geoengineering approaches, e.g. afforestation and reforestation.
- CO_2 capture and storage (CCS).

Table 1-1 compares the application areas, advantages and limitations of these different approaches. Based on the below Table 1-1, carbon dioxide capture and storage (CCS) is considered a crucial strategy for meeting CO_2 emission reduction targets which relies upon geological carbon dioxide storage (Leung et al., 2014).

Table 1-1 Summary of CO_2 Reduction Strategies (Leung et al., 2014)

Strategy	Application area/sector	Advantages	Limitations
Enhanced energy efficiency and energy conservation	Applied mainly in commercial and industrial buildings.	Energy saving from 10% to 20% easily achievable.	May involve extensive capital investment for installation of energy saving device.
Increase usage of clean fuels	Substitution of coal by natural gas for power generation.	Natural gas emits 40–50% less CO_2 than coal due to its lower carbon content and higher combustion efficiency; cleaner exhaust gas (lower particulates and sulphur dioxide emissions).	Higher fuel cost for conventional natural gas. Comparable cost for shale gas.
Adopt clean coal technologies	Integrated gasification combined cycle (IGCC), pressurized fluidized bed combustor (PFBC) etc.to replace conventional combustion.	Allow the use of coal with lower emissions of air pollutants.	Significant investment needed to rollout technologies widely.
Use of renewable energy	Hydro, solar (thermal), wind power, and biofuels highly developed	Use of local natural resources; no or low greenhouse and toxic gas emissions.	Applicability may depend on local resources availability and cost. Power from solar, wind, marine etc. are intermittent and associated technologies are not mature; most current renewable energies are more costly than conventional energy.
Development of nuclear power	Nuclear fission adopted mainly in US, France, Japan, Russia and China. Nuclear fusion still in research and development phase.	No air pollutant and greenhouse gas emissions.	Usage is controversial; development of world's nuclear power is hindered due to the Fukushima Nuclear Accident in 2011, e.g. Germany will phase out all its nuclear power by 2022.
Afforestation and reforestation	Applicable to all countries.	Simple approach to create natural and sustainable CO_2 sinks.	Restricts/prevents land use for other applications.
CCS	Applicable to large CO_2 point emission sources.	It can reduce vast amount of CO_2 with capture efficiency >80%.	CCS full chain technologies not proven at full commercial scale.

1.1.2 CO_2 Capture and Storage

- **CO_2 Properties**

CO_2 is normally found in the atmosphere in the gaseous phase; refer to the CO_2 phase diagram, Figure 1-3**.** From the phase diagram, at intermediate temperatures (between the triple point and critical points) CO_2 can exist as three distinct phases; solid, liquid and gas, with chemical and thermo-physical properties varying slowly and continuously within each phase field and discretely at the boundaries between them. Above the critical point at 7.40 MPa, 304.25 K (Taber, 1969), however, the distinction between a liquid phase and a gas phase disappears. Supercritical fluids tend to have densities similar to liquids, nonetheless have viscosities similar to those of gases (Morrow et al., 1988). Higher densities allow for a larger amount of CO_2 to be injected for a given increase in pressure, preventing rock hydro-fracture and the possible compromise of seal formations (Ennis-King & Paterson, 2002; Valvatne & Blunt, 2004). It is in this phase, therefore, that most CCS projects envision CO_2 existing in the subsurface. As the petrophysical properties of CO_2 are a strong function of temperature, pressure and salinity, experimental research into the subsurface behaviour of this CO_2 requires experiments to be made at these realistic conditions.

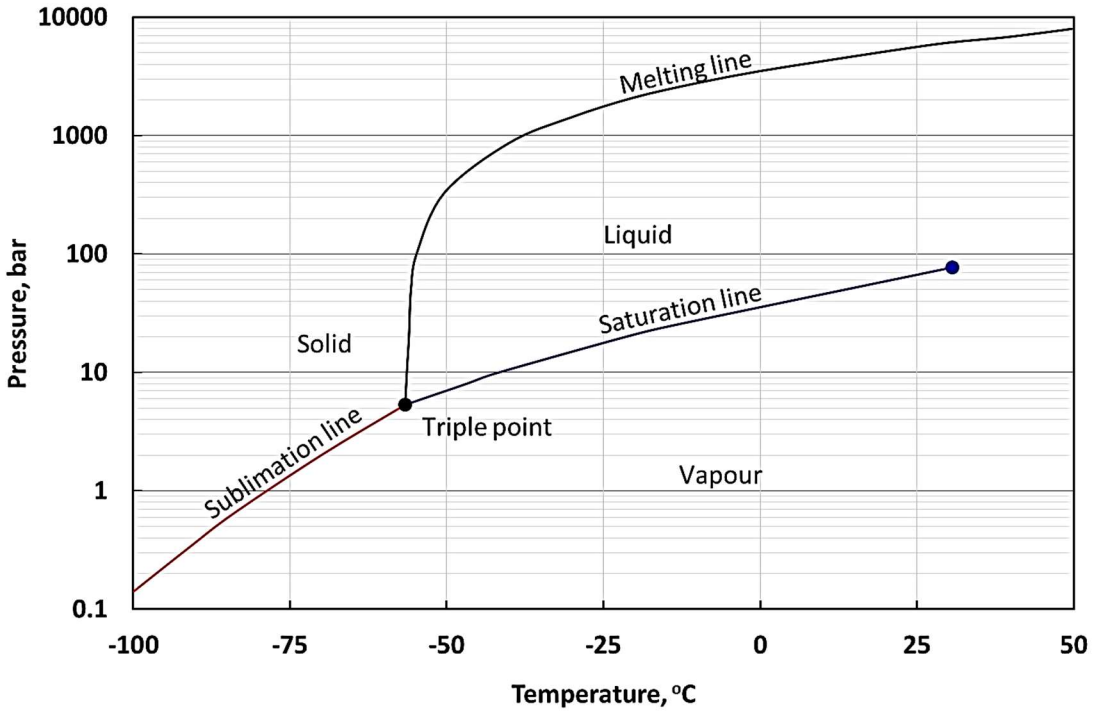


Figure 1-3-CO_2 Phase behaviour (Gunter et al., 1997; Moore & Slobod, 1955)

- **CO_2 Capture and Storage**

CO_2 Capture and Storage CCS is mainly applicable to large point source of CO_2 include large fossil fuel or biomass energy facilities, major CO_2-emitting industries, natural gas production, synthetic fuel plants and fossil fuel-based hydrogen production plants as shown in Figure 1-4. The process of CO_2 capture and storage (CCS) is consisting of three distinct processes including;

- First, separation of CO_2 from industrial and energy-related sources
- Second, transporting the captured CO_2 by pipeline or in tankers to a storage location; and
- Third, storing CO_2 underground and isolate it from atmosphere.

All three processes have been in use for decades, albeit not with the purpose of storing CO_2.

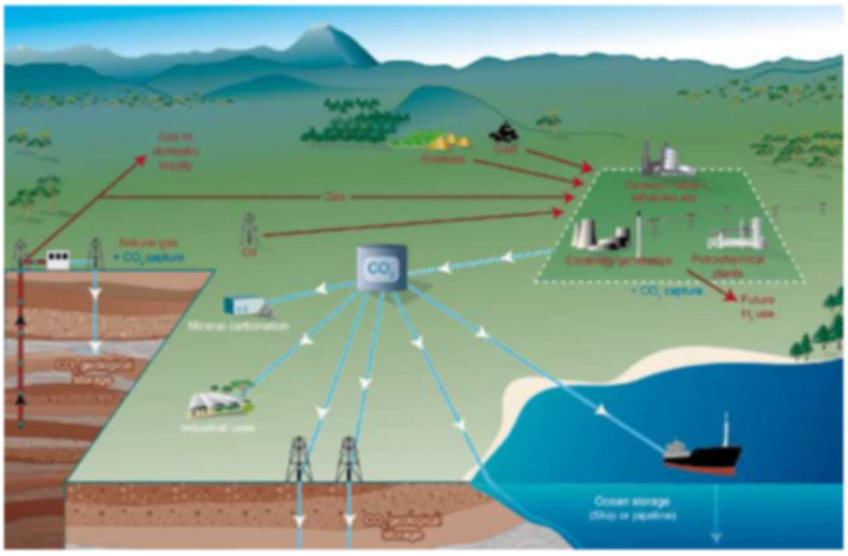


Figure 1-4 Source for which CCS might be Relevant (Metz et al., 2005)

CO_2 can be injected into geological storage sites, such as saline aquifers or depleted oil reservoirs (Moore & Slobod, 1955), where it will be trapped permanently. For CCS to be effective, it is necessary to ensure that CO_2 remains secure in the underground for hundreds to thousands of years (Bradshaw et al., 2007). Storage can be in deep oceans, depleted oil reservoir, coal beds, and saline aquifers, or even for enhanced oil recovery (Bachu, 2000), see Figure 1-4

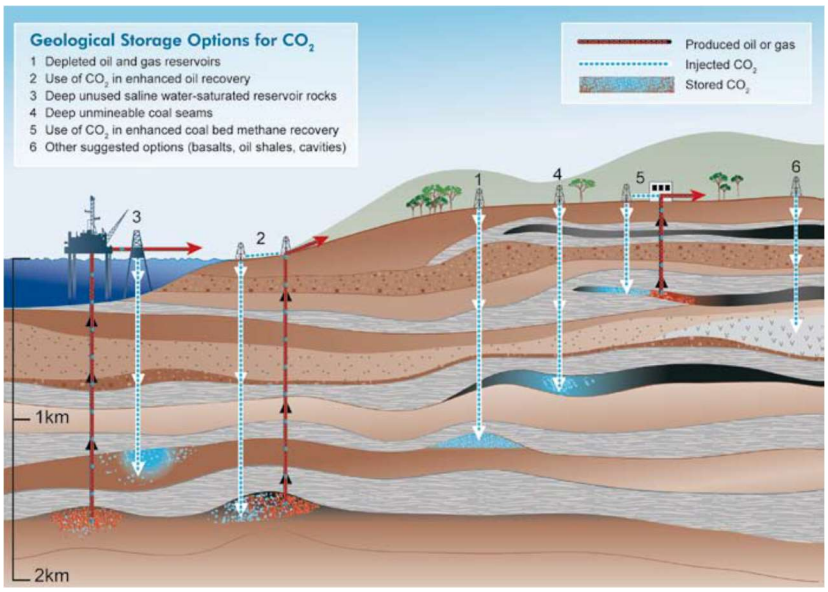


Figure 1-5-CO_2 Storage Options (Metz et al., 2005)

Saline aquifers have been identified as a preferred storage location for anthropogenic carbon dioxide emissions due to their enormous storage capacities and wide geographical spread areas both onshore and offshore (Bachu et al., 1994; Lide, 2004; Orr Jr, 2004).

However, despite the high potential for CO_2 storage, there is comparatively little knowledge about the CO_2 storage features of saline aquifers as compared to other geological sites such as coal seam sand oil fields primarily due to the lack of revenue associated with aquifer CCS in contrast to EOR applications. Deep aquifers at 700–1000m below ground level often host high salinity formation brines (Leung et al., 2014). And the storage of carbon dioxide in such formations must be carefully designed so that the carbon dioxide is trapped securely and will not escape to the surface. When selecting a saline aquifer storage site there should be a low permeable cap rock sealing in order to prevent CO_2 from escaping back to the atmosphere (Wollenweber et al., 2009).

1.1.3 CO_2 Trapping Mechanisms

CO_2 is sequestered in geological formations by three mechanisms: solubility trapping through dissolution in the formation water (Gunter et al., 1997; Reichle et al., 1999), mineral trapping through geochemical reactions with the aquifer fluids and rocks (Goldberg et al., 2001; Gunter et al., 1997; McPherson & Lichtner, 2001), and structural trapping the CO_2 plume by an impermeable formation (Bachu & Adams, 2003; Reichle et al., 1999). These mechanisms lead to storage of CO_2 as separate phase in pore spaces, dissolution in formation water and CO_2 converted to rock matrix.

1.1.4 Current and Planned CC Projects in Saline Aquifers

Figure 1-6 shows the CO_2 storage in saline formations and depleted oil reservoirs planned or underway around the world in 2005 (Metz et al., 2005).

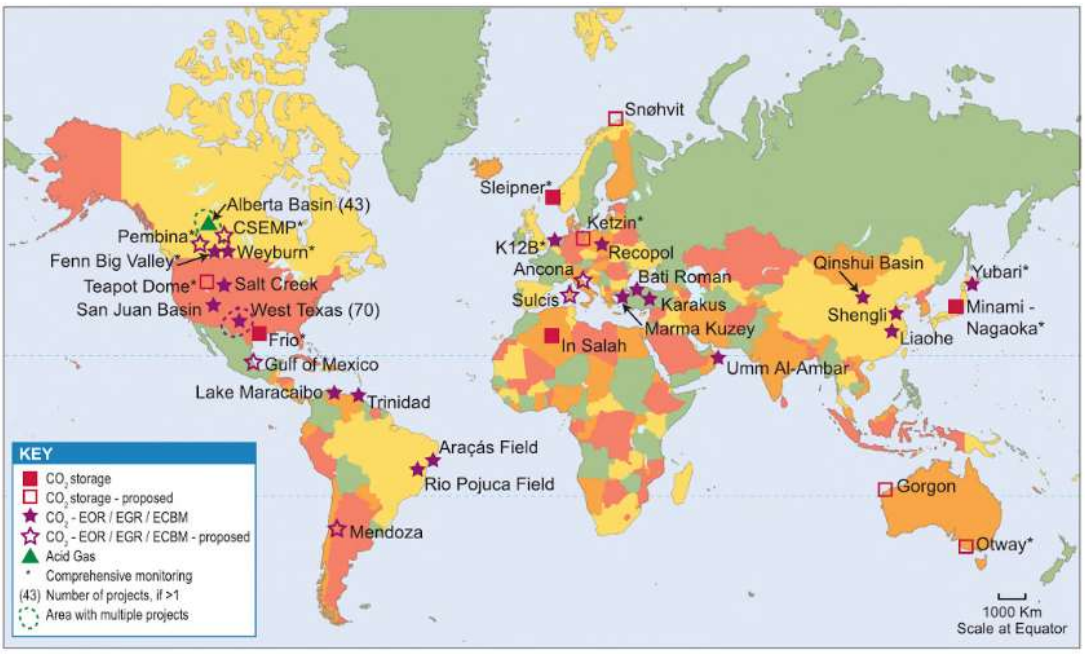


Figure 1-6 Location of sites where activities relevant to CO_2 storage are planned or under way (Metz et al., 2005)

The increasing demand for reducing CO_2 emissions due to strict legislations and the abundance of saline aquifers, make CO_2 storage in saline aquifers an attractive solution to reduce atmospheric emissions of CO_2. Table 1-2 summarises the current and planned project for CO_2 injection in saline formation (Leung et al., 2014).

Table 1-2 Summarise the Current and Planned Projects of CO_2 in Saline Aquifers (Leung et al., 2014)

Project Name	Location	Year of injection start	Max CO_2 injection (Mt/year)
Alberta Basin	Alberta & B.C. Canada	1990	**0.1**
Sleipner	North sea, Norway	1996	**1.0**
Frio	USA	2004	**0.1**
In Salah	Krechba, Algeria	2004	**1.3**
SnØhvit	Barents Sea, Norway	2008	**0.7**
MRCSP- Michigan Basin	Gaylord, MI, USA	2008	**0.2**
MRCSP- Cincinnati Arch	Kentucky, USA	2009	**0.2**
SECARB Early	Cranfield, MS,USA	2009	1.0
Mountaineer	West Virginia, USA	2009	0.1
MGSC Decatur	Decatur, IL, USA	2010	0.4
ZeroGen	Queensland, Australia	2012	0.7
Brindisi	Italy	2012	1.2
Gorgon	Barrow Island, WA, Australia D	2014	4.5
Latrobe Valley	Victoria, Australia	2015	13
Nagaoka	Japan	2015	0.007
Edwardsport	Indiana, USA	2015	1.0

The large storage capacity of deep saline aquifers has become a good option to store the captured CO_2. Aquifer formations are either sandstones or carbonates. Dry processed CO_2 is used during injection to avoid corrosion in pipelines. The fluid flow (CO_2) through a naturally fractured reservoir may be totally governed by the fracture system (Questiaux et al., 2010; Wennberg et al., 2008). Therefore, it becomes essential to investigate the interactions amongst the rock-brine (water) present in the aquifer and CO_2 in the context of a fracture system. It has been depicted that such interaction leads to dissolution and precipitation of minerals such as salts, which in turn affect the porosity and permeability of the rock.

The study of porosity and permeability has been given prime importance since it governs the storage or in other words prevents leakage of CO_2 back into the atmosphere. The literature presents lack in experiment based approaches towards understanding of these interactions.

1.2 Research Motivation

Based on the literature in the next chapter and to enhance our understanding for the dynamic mechanism of salt precipitation in porous media during drying periods and its effect on porous permeability, clogging and well injectivity different gravimetric and μ-CT tests were performed.

The gravimetric tests were focused on kinetics drying regimes for pure water and for NaCl solutions of 3.0 Molal and 6.4 Molal. The gravimetric tests were focused on the diffusive drying out regime. To assess the effect of temperature on the drying periods different air temperatures were used including; 30°C, 60 °C, 90 °C and 95 °C and at approximately relative air humidity. The effect of sample size on the evaporation rate and drying kinetics was assessed for short sample (20mm), medium sized samples (40mm and 80mm) and long sample (242mm) for 12mm in diameter. Also, the effect of different types of rocks characteristics on the drying out periods and on salt precipitation mechanisms were assessed for Bentheimer sandstone and Ketton carbonate.

μ-CT dynamic imaging tests were performed; the key objectives of the μ-CT dynamic imaging analysis were to understand the drying regime behaviour during the salt precipitation and assess the effect of the precipitated salt on the continuity of the hydraulic connectivity and liquid film detachment. Also, the μ-CT dynamic images were used to identify the salt precipitation location during the dry-out and concluded the impact of the precipitated salt on the permeability and assessed if the porous medium clogged.

1.3 Thesis Objectives

The overall goal of the experimental study in this thesis is to investigate the effect of injecting CO_2 into a fracture and study the mass transfer between matrix and fracture orthogonal to the flow direction in the fracture, also to investigate the dry-out that occurs due to the diffusion of water vapour from the brine saturated region of the matrix to the (assumed dry-filled with CO_2) fracture and the deposition of salt in the matrix or the fracture.

This investigation into the evaporative drying kinetics and salt precipitation in porous media was made through the use of a combination of gravimetric and X-ray μ-CT techniques to measure the water and brine saturation, salt precipitation and distribution in the test samples.

The main objectives of this thesis are:

- To review the literature on evaporative drying kinetics and salt precipitations in saline aquifers.
- To Measure the water or brine saturation using a gravimetric method and assess the effect of salt precipitation on the drying kinetics in Bentheimer and Ketton samples and by analysing the drying curve under test conditions.
- To measure the water or brine saturation and the deposition of salt crystals using the x-ray CT method and assess the effect of salt precipitation on the drying kinetics in Bentheimer and Ketton samples.

Based on the outcome from these objectives, a set of proposals for future study is also presented in chapter 5 in this thesis.

1.4 Thesis Structure

The remainder of this thesis is divided into 4 chapters, the content of which are described below.

Chapter 2, Review of Evaporative & Salt Precipitations in Porous Media

This chapter provides a selective background of the experimental investigations and the numerical approach to the evaporation, drying kinetics and salt precipitation in porous media. The chapter starts with describing the evaporation and drying kinetics stages in both capillary controlled and diffusive drying out regimes for pure water and brine solutions during evaporation from porous media. The drying kinetics and associated force balance including capillarity, viscosity and gravity forces are presented. In addition, the definitions of dimensionless numbers such as bond number, capillary number and Peclet number and their impact on the drying kinetics are presented. Then the effect of the precipitated salt on the enhancement and reduction of evaporation rate is presented. After that the chapter discusses the effect of efflorescent crusty-patchy formation during diffusive dry-out. This chapter presents the convective drying-out regime and the salt precipitation impairments on formation porosity-permeability as well as well injectivity clogging.

Chapter 3, `Experimental Set-up',

In the first part of this Chapter, the gravimetric test facility and testing procedures including the core-flooding cell and analytical balance arrangement are presented. The x-ray CT imaging

process facility and imaging processing techniques used to analyse the captured images are described in this chapter. This is followed by the parameters of the experimental test campaigns.

Chapter 4, `Results and Discussions

This chapter describes firstly the water, brine and salt precipitation results based on the gravimetric test method. The impact of the sand particles size, sample length and CO_2 temperature on the kinetic drying curve are presented in this chapter. The critical saturation and end effects on film connectivity are also addressed. The effect of salt precipitation on drying process is also presented. X-ray CT images of salt deposits obtained after drying for samples of different length saturated with brine are presented in this chapter. Finally, X-ray CT salt precipitation images obtained in situ during drying are presented together with the impact of the deposited salt on the sample porosity and permeability.

Chapter 5, `Conclusions and Recommendations for Future Work',

The thesis concluded by summarising the conclusions of all the previous chapters. A discussion of future work is also included.

Chapter 2

2 Review of Evaporation and Salt Precipitation from Porous Media

This chapter provides a selective background of the experimental investigations and the numerical approaches to the evaporation, drying kinetics and salt precipitation in porous media. The chapter starts with describing the evaporation and drying kinetic stages under diffusive drying out regime for pure water and brine solution during evaporation from porous media. The drying kinetics and associated force balance including capillarity, viscosity and gravity forces are presented. In addition, the definitions of dimensionless numbers including Bond number, capillary number and their impact on the drying kinetics are presented. Then the effect of the precipitated salt on the enhancement and reduction of evaporation rate is presented. After that the chapter discusses the effect of efflorescent crusty-patchy formation during diffusive dry-out. This chapter presents the convective drying-out regime and the salt precipitation impairments on formation porosity permeability as well as well injectivity clogging.

2.1 Evaporation Process from Porous Media

Evaporation from porous media is a complex pore scale transport processes affecting the liquid phase distribution and fluxes. Evaporation is a common important process for many industrial and engineering applications such as soil salinisation (relating to the excess accumulation of salts in soil), paper industry, building material, pharmaceutical applications, geological carbon storage and food preservation (Babalis & Belessiotis, 2004; Bickle, 2009; Farifteh et al., 2007; Fonseca & Scherer, 2015; Walters et al., 2014; Zhao et al., 2014).

2.1.1 Boundary Conditions and Dry-out Regimes from Porous Media

2.1.1.1 Diffusive Dry-out Regime from Porous Media

In porous media, evaporation is a multi-phase flow displacement process, which involves mass and energy transport including phase change, vapour diffusion and liquid flow. This process results in complex displacement patterns affecting drying behaviour and drying rates.

The evaporation rate from porous media and drying out stages are generally limited by atmospheric conditions and pore transport properties (Shokri, 2014; Van Brakel, 1980). The atmospheric demand is dependent on air flow boundary conditions such as air flow

velocity, air relative humidity and temperature. The evaporation rate depends on the air flow introduced to the sample.

Two types of air boundary conditions are discussed in this literature review, including: diffusive dry-out which is characterised by air flow past the surface of the fracture and convective dry-out which is characterised by direct air injection into the matrix.

Based on the interplay between the external air flow boundary conditions and the internal mass transfers during evaporation, the dry-out kinetics of porous media are divided into three main periods or stages of evaporation including; the first period is called constant rate period which depends on the external mass transfer, followed by the second period that is falling rate period. The last period is dominated by the internal mass transfer and is called receding front period.

Several researchers have investigated the dry-out kinetics periods of porous media (Chauvet et al., 2009; Idso et al., 1974; Laurindo & Prat, 1996; Lehmann et al., 2008; Philip, 1957; Sherwood, 1930; Shokri & Or, 2011; Van Brakel, 1980; Yiotis et al., 2012) investigated the drying periods during evaporation from porous media under ambient conditions.

For drying tests performed by passing air at the top of the sample and the saturated fluid was water, Sherwood (1930) reported two main drying periods. First stage “constant rate period” which was equal to the potential rate until the water content at the surface of the sample reached a “critical water content” and the falling rate period”. This “falling rate period” separated into a period limited by the transport of vapor through a viscous air film at the surface and a period that was controlled by the transport of vapor and liquid through the porous medium to the surface.

Philip (1957) investigated the evaporation from porous media under ambient condition and diffusive air flow boundary. In his study, Philip concluded that the first period; “constant rate phase”; was controlled by the atmospheric conditions whereas the second period; “falling rate phase”; was governed by conditions within the porous media. He divided the falling rate period into a period that is independent of atmospheric conditions and heat flow and into a final period sensitive to the heat flux.

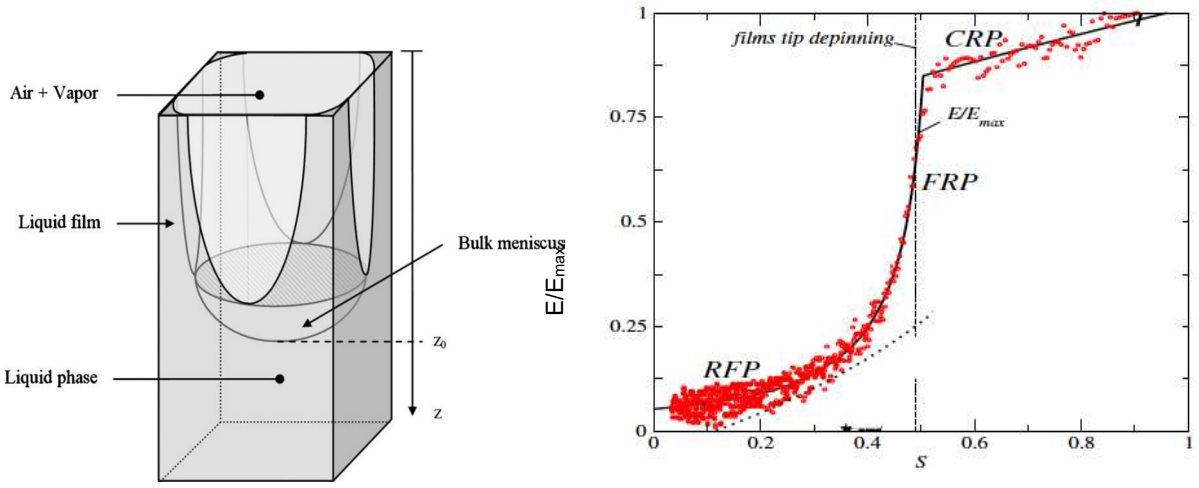
Similarly, Idso et al., (1974) established three drying kinetics stages, the first period was a constant drying rate controlled by atmospheric conditions, a first falling period limited by

transport of water to the surface, and a last period with very small water transport dominated by adsorption and evaporation of water from water films at the surface.

Further investigations in the liquid film detachment “film depinning” and the transition between the different stages of drying kinetics were assessed by Chauvet et al., (2009). They performed drying experiments in a single capillary square tube and under atmospheric conditions as shown in Figure 2-1 (a).

They introduced three main stages comprising a first period, called the constant rate period (CRP), which depends on the external mass transfer, followed by a second period, the falling rate period (FRP). The last period is dominated by the internal mass transfer and is called the receding front period (RFP). Chauvet et al., (2009) stated that the CRP was associated with a liquid film connection to the exposed surface, however, this constant rate period ends when the hydraulic continuity with the surface is disrupted when gravity and viscous forces overcome the capillary driving force as shown in Figure 2-1 (b).

Based on the test, Chauvet reported that the constant rate period was not exactly constant but slowly decreased (almost linearly) and this was due to the film thickness decrease in the tube entrance region during the CRP (Figure 2-1 b). Thus, the liquid was transported within the liquid films up to the sample surface because of the capillary forces and the thinning of the liquid film resulted in the slow decrease in the evaporation rate.



(a) square capillary tube **(b) drying periods (E/E$_{max}$ vs. Saturation)**

Figure 2-1 Sketch of the thick liquid films in a capillary tube of square cross section and drying periods by Chauvet et al., (2009)

The second period FRP (Falling Rate Period) was characterised by sharp drop in the drying rate. In the falling rate period the evaporative demand was larger than the flow capacity through the continuous liquid network.

Chauvet et al., (2009) also concluded that the CRP-FRP transition essentially coincides with the film depinning whereas the wetting phase became disconnected and that is due to the rupture of the thin films, hence the liquid no longer reaches the entrance of the system during the FRP.

During the third period (RFP), the liquid menisci receded from the surface to a level below the surface and form a new vaporisation plane referred to as the secondary drying front which was defined as the interface between the wet and dry zone and this period of the drying kinetic was characterised by square root of time. The transition from the FRP to RFP periods was controlled by internal mechanisms.

The transition between constant drying period (RCP) and falling rate period (RFP) was investigated by several researchers. Shokri and Or (2011) conducted evaporation tests using rectangular glass columns. The objectives of the experiments were to estimate the depth of the vaporisation plane that defines vapor diffusion length at the onset of stage-2

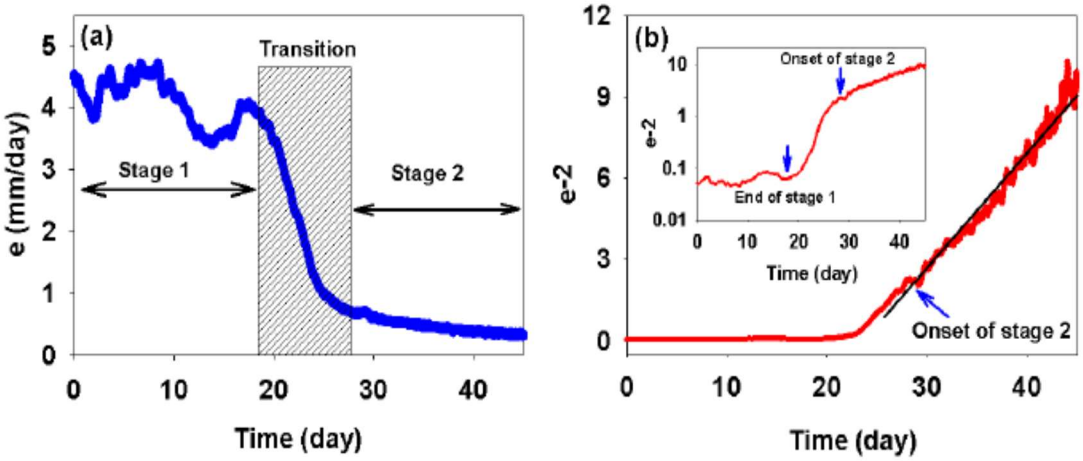
The height of the columns they used was 250 mm, with a width of 75 mm, and 10 mm in thickness). The sand and glass beads were uniformly packed particles with size distribution ranged from 0.025mm to 0.771mm. Columns were only open at the top to allow evaporation at room ambient conditions.

Figure 2-2 (a) shows an example of the analysis performed on data of the column packed with sand with an average particle size of 0.224 mm to determine the onset of stage 2. The Figure 2-2 (a) shows that during the early evaporation, noted as stage 1, the rate was relatively constant, followed by a much lower value.

After, 19 days, the transition (hatched zone) between the stage 1 and stage 2 evaporation regime started. During this transition, the evaporation rate decreased sharply which means disconnection in the liquid film from the surface of the sample was established.

The complete detachment of the liquid films from the surface indicated the onset of stage 2 evaporation whereas a new vaporization plane at a level below the surface of the sample was formed.

Figure 2-2 (b) shows the inverse of the square of evaporation rate versus time. In this figure, the onset of stage 2 was indicated by the intercept between the linear regression and the curve. In Figure 2-2 (b), the inset illustrates the same data, but in the log-scale to highlight and distinguish between stage-1, transition period, and stage 2 evaporation.



(a)drying rate versus time (day) **(b) inverse of the square of evaporation rate**

Figure 2-2 Column packed with sand with an average particle size of 0.224 mm to determine the onset of stage 2 (Shokri & Or, 2011)

Shokri & Or's (2011) findings offered the predictability of the depth of vaporisation plane at the onset of stage 2 evaporation, hence prediction of the diffusion controlled evaporation rate. Further Lehmann et al., (2008) explored on the conditions required for sustaining stage 1 evaporation, focusing on the importance of the liquid film evaporation regime.

Lehmann et al., (2008) used sand-filled cylindrical Plexiglas columns (diameter of 54 mm and length of 50–350 mm) and rectangular Hele-Shaw cells (260 mm in length, 10 mm in thickness, and 75 mm in width) in his experiments to quantify the evaporation rates. The top boundary of the columns and cells is open to the atmosphere.

Different particle sizes were used in the evaporation experiments ranging from 0.1–0.5 mm "fine" and 0.3–0.9 mm "coarse" to measure the evaporation under several atmospheric evaporative demands from columns with different lengths (50-350mm).

In their experimental investigations, Lehmann et al., (2008) focused on stage 1 and stage 2 evaporations regimes. They introduced a characteristic length (L_{cap}) where the transition in the evaporation rate happens from a first stage that was a liquid-flow based limited only by vapour

exchange with air to a second stage based on the diffusion of vapour through a medium (square root of time).

In addition, the hydraulic connectivity between the receding drying front and evaporating surface will break at a characteristic length (L_{cap}). The characteristic length (L_{cap}) combines the characteristic length for the gravity force (L_G) and viscous dissipation characteristic length (L_V). The gravity length L_G can be expressed as function of Bond number per:

$$L_G = \frac{r_2}{Bo}\left(\frac{2}{\gamma} - 2\right) \qquad \text{Equation (1)}$$

where:

L_G: the gravity length

r_2: radius of the large pore

γ: pore size ratio $\frac{r_1}{r_2}$

r_1: radius of the small pore

Bo: Bond number as in equation (3)

Bond number (Bo) expresses the relative importance of gravitational to capillary forces and is given by this equation (Laurindo & Prat, 1998);

$$Bo = \frac{\Delta\rho\, g\, {r_2}^2}{\sigma} \qquad \text{Equation (2)}$$

where:

$\Delta\rho$: the difference between the liquid density and the gas density

g: the acceleration due to gravity

σ: the surface tension

The capillary number for flow in porous media Ca is the ratio between viscous and capillary forces as in above Equation (1). Based on capillary force, the viscous length is proportional to the capillary number:

$$L_v = \frac{r_2}{Ca}\left(\frac{2}{\gamma} - 2\right) \qquad \text{Equation (3)}$$

Lehmann et al., (2008) stated that in capillary-driven liquid flow, the extent of the film region depends on water-filled fine pores, drying front depth, and viscous resistance to flow through liquid films at the surface. A gas phase tended to displace the liquid in large pores, while liquid was retained in the smallest pores at the surface.

Figure 2-3 shows a conceptual diagram for drying kinetics stages from porous media. Lehmann et al., (2008) reported that the lowest evaporation corresponded to cool and humid conditions 21 °C and 58% humidity whereas the highest initial evaporation rate occurs at high temperature and low humidity 28 °C and 31% humidity.

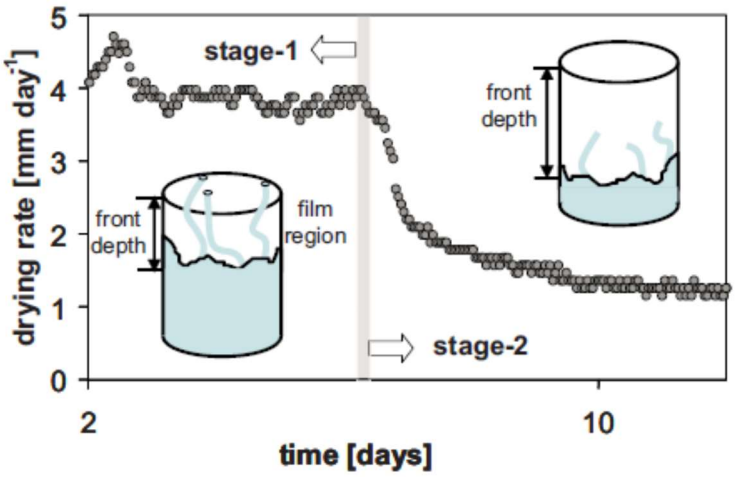
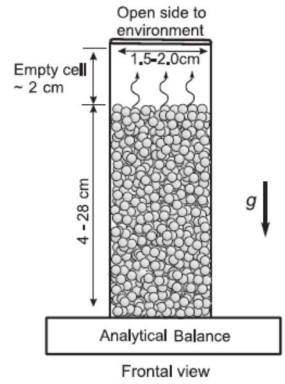


Figure 2-3 Conceptual diagram of first-stage evaporation by Lehmann et al., (2008)

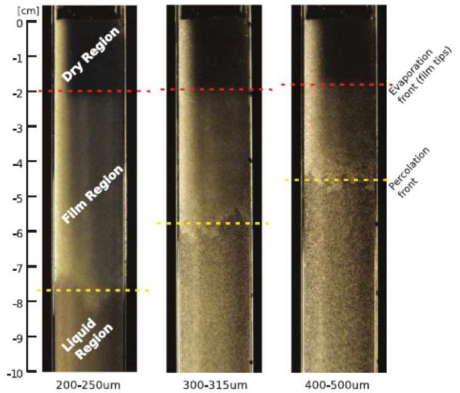
Lehmann et al., (2008) concluded that the connected liquid films controlled the flow of liquid to the drying front and the duration of stage 1.

The extent of the film region, which determined the transition between the constant rate period and the falling rate periods in drying was investigated by Yiotis et al., (2012). Their experimental investigations were performed using a bead pack which was initially saturated with volatile hydrocarbons. The packings were placed in thin glass cells (akin to a Hele-Shaw cell) keeping the top side open and exposed to the ambient environment, see Figure 2-4 (a).

The beads were left to dry at environmental conditions. The height of the cell ranged from 60mm to 300mm. The average size of the glass bead ranged from 100 to 850 μm. Figure 2-4 (b) shows the (Color line) the location of evaporation and percolation fronts in experiments with different bead sizes, from left to right,200–250 μm, 300–315 μm, and 400–500 μm.



(a) Schematic of packed column test set-up



(b) (Color online) The location of evaporation and percolation fronts in experiments with different bead sizes, from left to right,200–250 μm, 300–315 μm, and 400–500 μm

Figure 2-4 Schematic of test and the location of evaporation and percolation fronts by Yiotis et al., (2012)

Figure 2-5 shows the experimental results of the typical drying curve (normalized drying rate). The cross (+) shows the point at which the film region was detached completely from the surface of the sample. The inset shows the corresponding dimensional variables. The dashed line shows the theoretical (1/square root of time) dependence at later time.

Based on Figure 2-5 by Yiotis et al., (2012), the drying curve displays two clear drying periods. The first period where the liquid films were attached to the surface of the packings and known as constant rate period. (CRP). During the CRP, the evaporation process was controlled by the mass transfer within the empty, upper part of the cell. The second period was the falling rate period (FRP) where detachment of the films from the porous medium occurred.

The transition from CRP to FRP was found to coincide with the film tips detaching from the external surface and the development of a completely dry region of beads in the upper part of the packing. Yiotis et al., (2012) concluded from the tests that extent of the film region was found to be a function of a film-based capillary number, the Bond number Bo, and the Sherwood number.

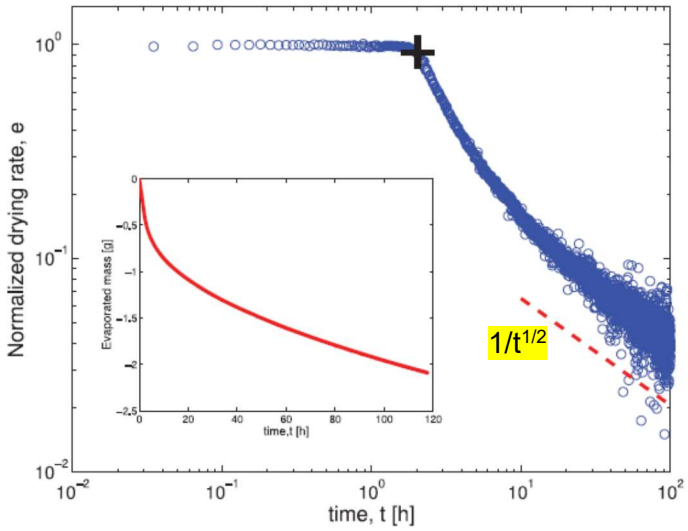


Figure 2-5 Experimental results for a typical drying curve in the 30-cm-long tube for a packing of 150–200 μm beads saturated with pentane (Yiotis et al., 2012).

(Shokri et al., 2009a, 2010a; Shokri et al., 2008b) performed detailed experimental investigations to understand the dynamic of the drying front from porous media and under atmospheric conditions. They demonstrated that during evaporation stage-1 (constant rate period-CRP), liquid menisci in fine pores at the surface remain coupled with atmosphere.

These hydraulically connected evaporating pores support a capillary pressure gradient and draw water from the porous medium interior to supply evaporative demand at the surface. However, at a certain depth of the drying front, the downward gravity and viscous forces overcome the upward capillary driving force, disrupting hydraulic continuity with the surface.

The disruption of hydraulic continuity marked the end of stage-1, and subsequently liquid menisci recede from the surface to a level below the surface and form a new vaporization plane referred to as the secondary drying front by Shokri et al., (2009a) who defined it as the interface between the wet and dry zone.

This transition marked the onset of stage-2 evaporation; a period with a lower evaporation rate limited by diffusion through the porous media (Lehmann et al., 2008; Shokri et al., 2009a, 2009b, 2010b) experimentally confirmed these mechanisms for stage-1 and -2 evaporation.

Another classification of the drying stages was based on pore numerical network scale models. The pore scale model was used to investigate the evolution of the phase distribution from porous medium during drying periods.

Laurindo and Prat (1998) performed evaporation experiments in two-dimensional transparent micromodels under quasi-isothermal conditions. The tests were compared to numerical pore network models.

The study was devoted to the evolution of the phase distribution during drying from porous medium. The tests were performed under atmospheric conditions which implied evaporation rates were relatively low and heat transfer was negligible between the sample and flowing air at the top of the sample.

The 2D transparent micromodels were 140*140 networks containing 39,000 ducts which includes seven classes of width ranging from 0.1 to 0.6 mm that were randomly distributed. The cross section of each duct representing a throat had a rectangular shape with a constant 1 mm depth. The saturated liquid was hexane.

For the numerical analysis, Laurindo and Prat (1998) used the standard pore network simulator. The simulator was based on an invasion algorithm combining elements of the invasion percolation algorithm. The capillary and gravity effects were considered. Significant differences in the drying curves were observed as a function of the Bond number (whether Bo =0 or Bo <0 or Bo >0).

Based on Bond number value, Laurindo and Prat (1998) considered three basic cases. The first case was the one where gravity forces were negligible and capillary effects dominated the process (Bo = 0), see Figure 2-6.

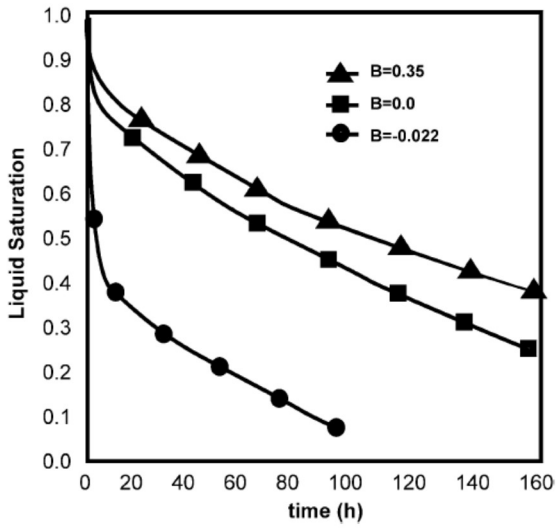


Figure 2-6 Liquid saturation with time (data point in this figure was obtained from 2-D drying tests from Laurindo and Prat (1998)

In the second case, the gravity forces tended to destabilise the invasion process (Bo < 0), see Figure 2-6. In this case, the external diffusive layer resistance to transfer during this first period controlled drying rate. Therefore, this case tended to be the fastest drying rate.

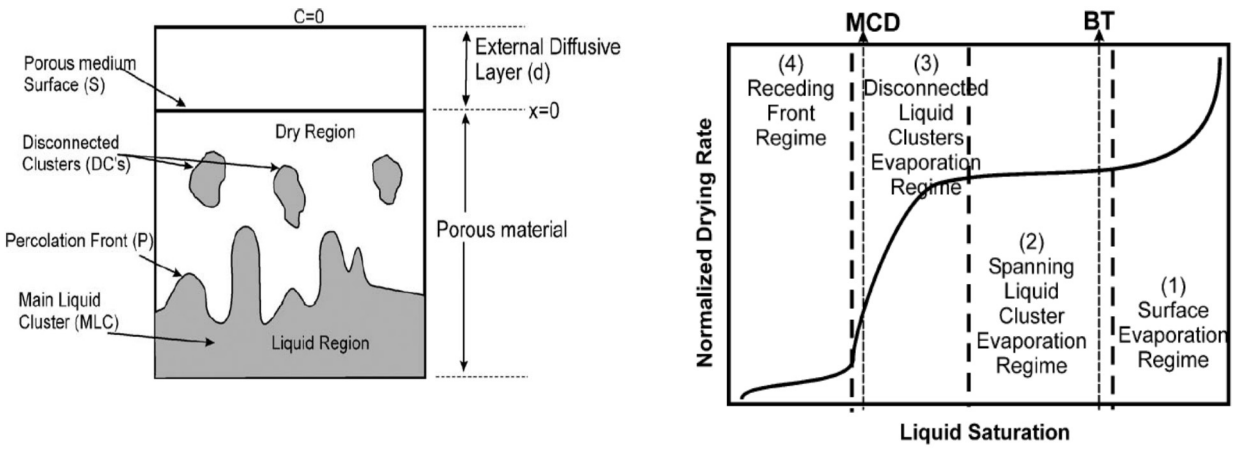
The third case was the one where the gravity forces tended to stabilise the invasion process (Bo > 0) see Figure 2-6. This was characterised by a receding fractal invasion front of finite extension. The internal resistance to transport within the zone of the network invaded by the gas phase determined the drying rate. Therefore, this case had the slowest drying rate.

Laurindo and Prat (1998) concluded that three regions could be distinguished, including; fully saturated regions, cluster regions where isolated liquid clusters were present and dry regions where gas phase invaded all the ducts and there was no liquid cluster.

The four drying regimes reported above were confirmed by Yiotis et al., (2006) who studied the drying curve periods using 3-D pore network models. This model accounted for the effect of capillarity and buoyancy at the liquid–gas interface and for diffusion through the porous material and through a boundary layer over the external surface of the material.

The numerical analysis focused on the periods that were developed in the drying of capillary porous media, particularly the constant rate period (CRP) and the falling rate period (FRP). The study considered the isothermal drying of a 3-D cubic pore network. This 3-D model was initially saturated with hexane.

The top side of the pore network was open to the ambient condition, the rest of the other sides were contained and impermeable to mass transfer. Figure 2-7 (a) shows schematic of the different component of the drying from porous media considered in the 3-D pore network model. In this figure, the C was referred to vapor concentration at the surface of the pore network (x=0).



(a) Schematic of the drying problem considered

(b) Characteristic drying regimes when capillarity controls the process

Figure 2-7 Schematic of the drying problem considered and characteristics drying regime by Yiotis et al., (2006)

Based on the pore network modelling results, Yiotis et al., (2006) identified four drying regimes as shown in Figure 2-7 (b). During the initial surface evaporation regime, the evaporation occurred at the surface of the sample. Only liquid pores located at the surface were invaded and the space available for diffusion in the porous medium was negligible. During this regime, the drying rate decreased sharply until the gas cluster was large enough and vapor diffusion through the gas phase commenced. The end of this regime occurred close to the gas breakthrough point BT as shown above in Figure 2-7 (b).

The second regime started after the gas breakthrough (BT) as shown in above Figure 2-7 (b). During this stage the evaporation rate at the open boundary was exactly balanced by the flow through the main liquid cluster MLC, see Figure 2-7 (a).

The main liquid cluster MLC covered most of the surface and only a small number of disconnected liquid clusters DCs exist. Due to the spanning of the main liquid clusters (MLC), the average position of the drying front remained practically constant. This regime corresponded to the constant rate period (CRP) where the capillarity controlled the movement of the liquid-gas interface.

The third drying regime or the disconnected liquid clusters evaporation regime began when the number of disconnected liquid clusters (DCs) at the surface became sufficiently large and the drying rate from the DCs become comparable to the drying rate from the main liquid cluster (MLC).

The fourth drying regime occurred when the open surface became dry and diffusion took place through the dry zone. The liquid–gas interface receded in the porous medium (RFP). This period started after the main cluster disconnected (MCD) point.

2.1.1.2 Convective Dry-out Regime from Porous Media

Similarly, the diffusion drying regime, several researchers performed convective drying out regimes where air was injected directly to the sample. The evaporation periods under salinity conditions and impact of salt precipitation on the different stages were reported.

The precipitation of solid NaCl (halite) around a CO_2 injection well and the effect of NaCl (halite) precipitation in the well injectivity was studied by Giorgis et al., (2007) for a pilot test of CO_2 injection in a depleted Italian gas reservoir. The simulation of supercritical CO_2 injection was simulated with TMGAS TOUGH2 (multicomponent GASes) using 1D radial and 2D radial grids.

The TMGAS can simulate the two-phase flow of a gas mixture in equilibrium with a sodium chloride brine, including the modelling of halite precipitation/dissolution following the EWASG approach (equation of state for water, salt and gas). Verma and Pruess (1988) (V&P) permeability-porosity pore network model was used to capture the effects of salt precipitation on formation permeability and injectivity losses.

Depending on the initial liquid saturation, two different behaviours of evaporation and salt precipitations were assessed when brine has low mobility and sufficient mobility.

Giorgis et al., (2007) found that for the case of the immobile brine with a constant value of aqueous phase saturation Sw=0.15, the evaporation and precipitation fronts migrate in the interior of the formation and the halite precipitation was uniformly distributed. At this low mobile brine, there was insignificant effects on well injectivity because the effect of gravity was negligible relative to the injection pressure gradient.

However, Pruess and Müller (2009) investigated the fundamental aspects of drying and salt precipitation in saline aquifers as a result of CO_2 injection using numerical simulations. The numerical simulations were performed with a single injection well in idealized 1D and 2D radial geometries. The simulations analysis was performed with reservoir simulation code TOUGH2 which was improved with a fluid property module ‘‘ECO2N’’.

The ‘‘ECO2N’’ fluid properties model provided accurate fluid properties for the system

water/CO_2/NaCl for temperatures in the range from 10 to 110°C, pressures up to 600 bar, and salinity to full halite saturation as used in previous modelling analysis performed by Pruess & Spycher (2007). They concluded that the key mechanisms affecting the dry-out and salt precipitation process during the CO_2 injections were the displacement of brine away from the injection well by the injected CO_2, evaporation of brine into the flowing CO_2 stream, up flow of CO_2 due to gravity effects (buoyancy), backflow of brine toward the injection point due to capillary pressure gradients that oppose the pressure gradient in the CO_2-rich (''gas'') phase, and molecular diffusion of dissolved salt. The different mechanisms operate on a range of spatial scales.

Pruess and Müller (2009) reported that in depleted gas reservoirs and saline aquifers and in the vicinity of the injection well, the continuous injection of dry CO_2 may cause complete formation dry-out which eventually lead to salt precipitation which agreed with the work reported previously by (André et al., 2007; Fuller et al., 2006; Giorgis et al., 2007; Hurter et al., 2007; Pruess & García, 2002).

André et al., (2014) presented a numerical modelling analysis that could reproduce the experimental results of the drying of brine-saturated sandstone cores by gas injection in the laboratory. The laboratory test set up is presented in Figure 2-8.

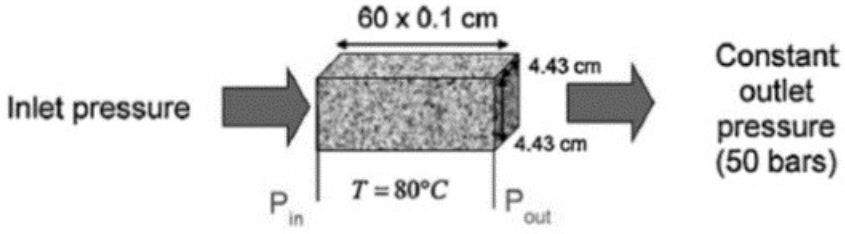


Figure 2-8 Experimental procedures to study the drying-out of a sandstone core under a continuous flux of gas by André et al., (2014)

In the laboratory, nitrogen was injected into Vosges sandstone cores that were encapsulated in X-ray transparent cells and placed in an oven under controlled temperature (80°C). The cell was composed of a membrane in order to confine the core at a pressure of 50 bar. In this test, local water saturation was measured using X-ray attenuation techniques. The volume of expelled water and outlet gas was measured.

André et al., (2014) performed the laboratory tests by applying pressure to the core initially saturated with a 35 g/L of brine. The pressures values were 120 mbar, 800 mbar and 1500 mbar. Another set of test was performed by applying a constant difference pressure of 300

mbar which was imposed to the core initially saturated with a150 g/L of brine.

For the first test, the gas/water flow displacement and rapid gas breakthrough was reported and at low gas rate. For the highest pressure, drying was very rapid and lasting only few hours. For the constant difference pressure test of 300mbar, a rapid gas breakthrough was observed with an increase of the gas flow rate.

André et al., (2014) concluded the work by demonstrating the important role of both capillary forces and salinity of the initial brine on the changes in permeability. The tests addressed the addressed the relationship between different parameters including salt deposits, gas injection and the capillary properties of porous medium subjected to non-wetting fluid location. A sufficiently high gas injection rate overcame the capillary forces and limited the precipitation of salts in the vicinity of well.

Roels et al., (2014) experimentally and numerically investigated the salt precipitation in porous rock caused by the evaporation of water into injected gaseous phase CO_2. The CO_2 was injected in brine-saturated Bentheimer sandstone. The test results were compared with the numerical simulations and the discrepancy between experimental and modelling results regarding salt precipitation was presented and discussed.

For the purpose of the numerical work, the TOUGH2 reservoir simulator with the equation of state module ECO2N was implemented. In addition to the TOUGH2/ ECO2N, Roels et al., (2014) developed a numerical code (kinetic model) with an alternative approach on evaporation.

The drying tests were performed in cores with a diameter of 1.0 cm and a length of 3.0 cm. The sandstone core and the holder were developed such that they could be positioned vertically in the Nanotom µ-CT (micro computed tomography) scanner. Every few hours a 3D scan was taken without interrupting the test.

As part of the sample preparation procedures, the flooding experiment was performed in a homogeneous Bentheimer sandstone core. After pre-flushing the core with CO_2 to remove air from the core sample, the sample core was filled with brine.

The brine (saturated potassium-iodide solution) was injected from the bottom of the core. In addition, the CO_2 injection was started from the top of the core at a rate of 5 mL/min. Both temperature and pressure drop over the core were measured continuously.

Figure 2-9 (a,b,c) shows two slices obtained by µ-CT scanning for the homogeneous

Bentheimer sandstone. Figure 2-9 (a) before the dry-out experiment and Figure 2-9 (b) after the dry-out experiment. In the μ-CT scans in Figure 2-9, the precipitated salt was clearly visible as bright spots in the pore space compared to the initially dry rock.

Approximately 2000 slices were reconstructed along the core length resulting in a 3D image as shown in Figure 2-9 (c). On the right-hand side, only solid salt within the pore space was presented, while the initial rock was shown on the left.

Roels et al., (2014) reported that salt formation was observed in formation in small as well as large pores and a uniform distribution throughout the core Figure 2-21 (c). The location of salt precipitation was crucial to the connectivity of the flow path.

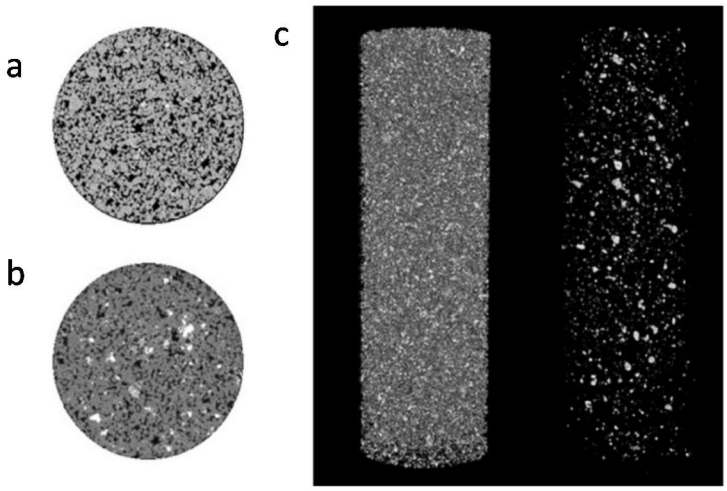


Figure 2-9- Slices of CT images of the homogeneous Bentheimer sandstone (a) prior to and (b) post experiment and (c) 3D representation of dry core and precipitated salt. Precipitated salt is represented by the white color, gray represents the soil matrix and gas is shown by the black color by Roels et al., (2014)

Roels et al., (2014) compared the salt precipitation profile along the core at the end of the test with the numerical results, (see Figure 2-10). They concluded that the simulation and experimental results were compatible for most of the domain. In Figure 2-10, the discrepancy between the simulation and tests at the inlet was due by an overestimation of the capillary end effect by the model as stated by Roels et al., (2014).

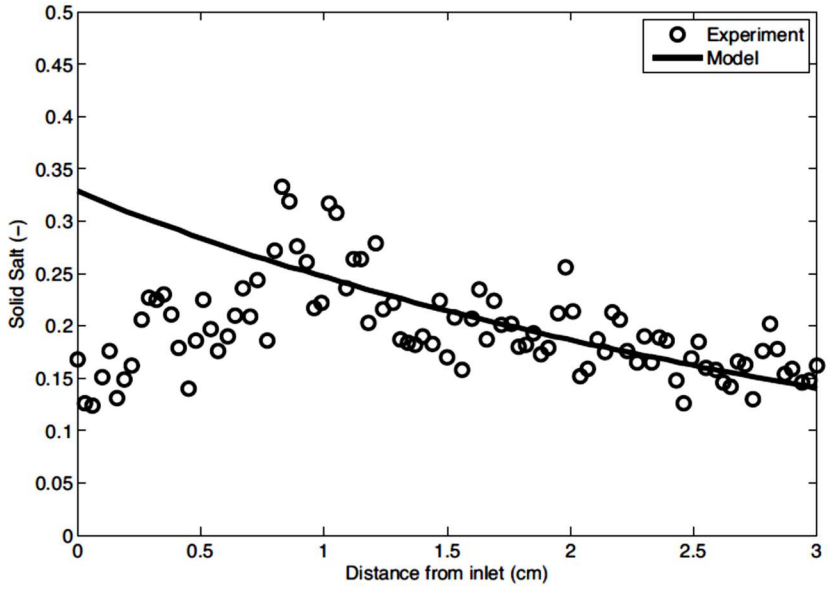


Figure 2-10- Salt precipitation profile along the core after dry-out (Roels et al., 2014)

Further Roels et al., (2016), performed further experimental investigations on the capillary driven flow of dissolved salt to the drying zone during CO_2 injection in homogenous coarse textured and in cores in porous media using Bentheimer and Berea sandstones. Different sample lengths were used for the tests (4cm and 9cm) with 0.1cm in diameter. And dynamic μ-CT (micro computed tomography) scans were taken during the evaporation tests. The porosity of the Bentheimer sandstone was 0.21 ± 0.01 and 1.3 ± 0.1 × 10−12 m^2 permeability whereas Berea sandstone was 0.21 ± 0.01 porosity and 2.4 ± 0.1 × 10−13 m^2 permeability.

The layered cores consisted of a coarse-textured layer overlaying a fine textured layer. The CO_2 was injected in the upper part of cores and bottom part of cores functioned as brine sources. The procedural steps for the core flooding experiments were as explained in (Roels et al., 2014).

For the short Bentheimer core, Roels et al., (2016) reported that after the injection of CO_2, the main drying mechanism was evaporation of water into the gaseous phase as shown in Figure 2-11. In this figure, after 15.5 hours of CO_2 injection, complete clogging of the injection well was observed (the clogging is represented as the dark red color in Figure 2-11).

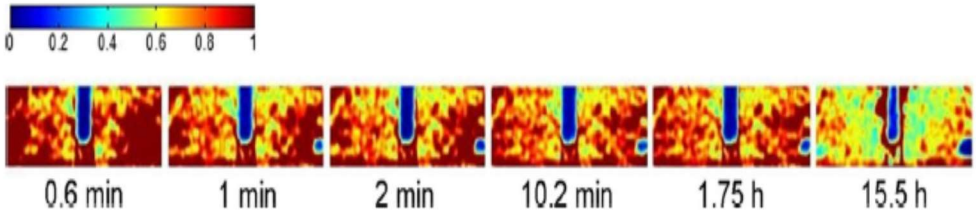


Figure 2-11 CT scan imaging for Brine saturation at different times obtained for short Bentheimer core by Roels et al., (2016). The brine saturation represents both the presence of brine and solid salt. After 15.5 h of injection, complete clogging of the injection well can be observed (dark red)

For the long cores, homogenous Bentheimer sandstone core and the layered core consisting of Bentheimer and Berea, Roels et al., (2016), presented the dry-out scans in Figure 2-12. In Figure 2-12, the first scans from the left-hand side, which were taken at 1 min and 10 min after CO_2 injection started, showed the remaining brine saturation after CO_2 breakthrough.

From the CT scans, it can be observed that in both homogenous Bentheimer sandstone core (Figure 2-12a) and layered core consisting of Bentheimer and Berea (Figure 2-12b), CO_2 initially did not spread into the lower part of the cores. It was clearly visible from Figure 2-12b, that the Berea layer was not penetrated by CO_2 injection at all. However, after approximately 98 hours of the drying process, the dry-out of the lower parts of the cores became visible and was more pronounced in the homogeneous Bentheimer core. At 142 hour, dry-out of the lower part of the Berea sandstone became significant.

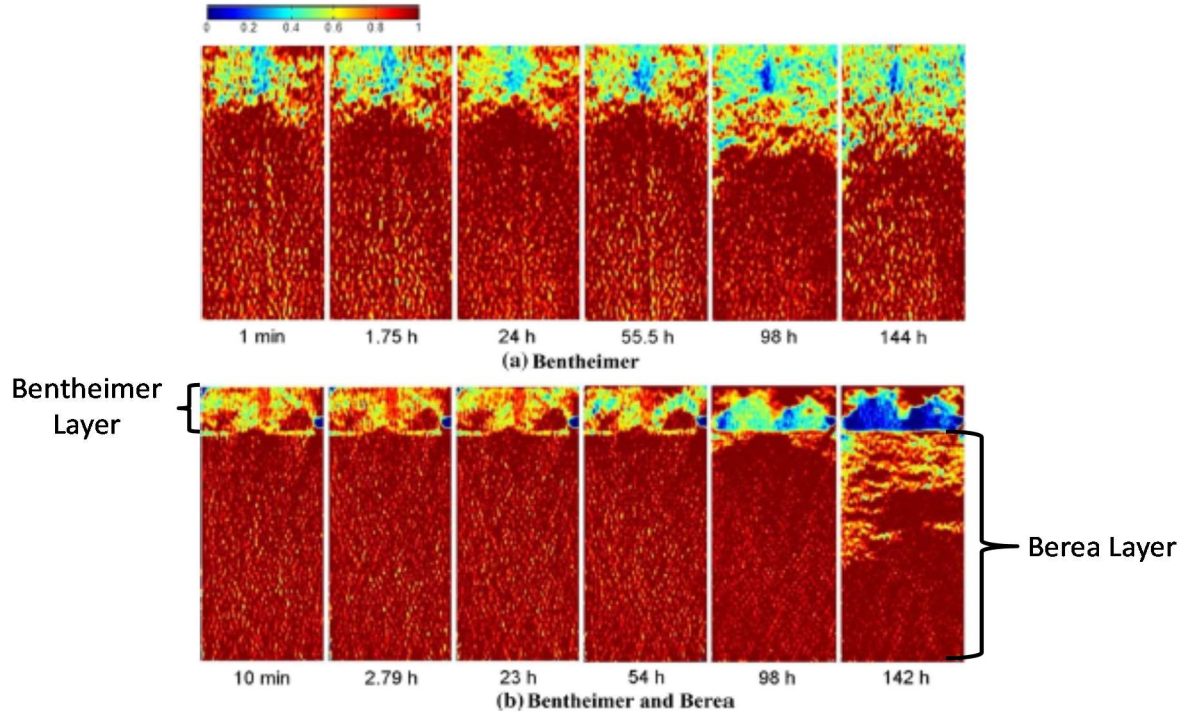


Figure 2-12 CT scan images at various times for a homogeneous Bentheimer core and b layered Bentheimer and Berea core (Roels et al., 2016)

Roels et al., (2016) reported that solid salt was not quantified directly from the CT scans. Despite that, the results indicated that the precipitation of salt in the case of the Bentheimer sandstone, formed throughout the upper part of the core. For the case of the layered core, the salt precipitation was observed only near the top (dark red in Figure 2-12b).

For the well injectivity and well clogging, Roels et al., (2016) reported ,using the CT scan images, that in the short Bentheimer core, the injection well was completely clogged before complete dry-out was reached in the core as shown in Figure 2-13a. The light gray color in the outer part of the core shows pore spaces filled with brine. For the layered core, salt precipitated throughout the Bentheimer layer and reduced the available pore space dramatically. However, complete clogging near the injection well as reported in short Bentheimer core did not occur (Figure 2-13b).

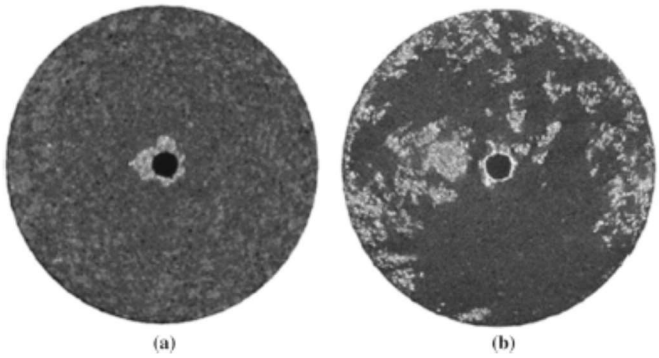


Figure 2-13 Post experiment μ-CT scans taken at 0.8 cm from the top from a short Bentheimer core and b layered core by Roels et al., (2016). White color represents higher density (solid salt) and black color represents lower density (CO_2). Solid salt was found a accumulated around the injection well and b distributed along the domain

The pressure drop between injection well and outlets was measured during the dry-out tests as reported by Roels et al., (2016) (see Figure 2-14). In Figure 2-14, the dashed line represents the measured pressure drop for the short homogenous core, the black line represents the measured pressure drop for the long homogenous Bentheimer core and the line with symbols shows the measured pressure drop in the long-layered core. They reported that in all tests, salt precipitations caused an increase in pressure drop due to a decrease in rock permeability.

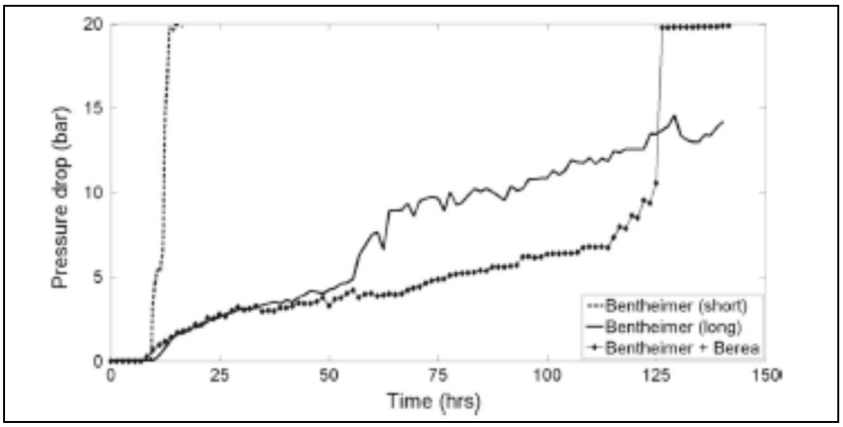


Figure 2-14 Pressure drop vs. time for three experiments by Roels et al., (2016)

Ott et al., (2015) experimentally investigated the consequences of dry-zone formation in the vicinity of gas injection and production wells using core flood experiments. The tests results were verified using numerical analysis (TOUGH2). In the test the Berea sandstone with an average permeability of 500 mD and 22% porosity was used. The Berea sandstone was pre-saturated with NaCl-based high-salinity brine: 20 wt% NaCl and 2 wt% CsCl. The CsCl was added as a contrast agent as its X-ray absorption coefficient is high, leading to a high X-ray absorption contrast in µCT between the aqueous and the CO_2-rich phase. In the core flood tests, the dry SC CO_2 was injected from top to bottom into brine saturated sand stone samples until complete dry-out of the sample was achieved, see Figure 2-15).

During the core floods tests, effective permeability and fluid and salt saturations were monitored and measured. Gas flow rate and differential pressure were measured to calculate the effective permeability. The tests were performed under 100 bar pressure and 45^{o}C temperature.

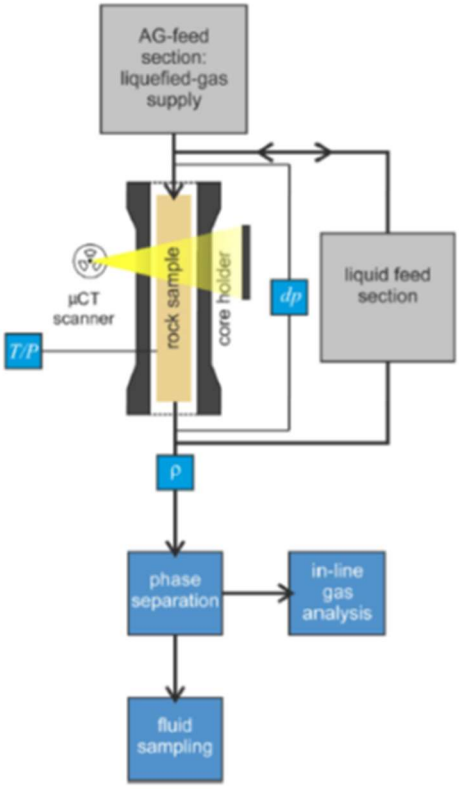


Figure 2-15 Schematic of the experimental setup by (Ott et al., 2015) and more details are provided in (Ott et al., 2012).

During injection, spatial and time evolution of saturation changes were monitored by means of micro computed tomography (μCT). CT scans were recorded in order to record the salt precipitation patterns.

Ott et al., (2015) reported the observed salt precipitation patterns using the recorded CT scans images as shown in Figure 2-16 (a-e). The images in Figure 2-16 shows μCT cross-sections (top row) and a 3D image. The CT scans images in Figure 2-16 shows the salt precipitation in the region of local precipitation between 0 and 5 cm from the inlet and Figure 2-16 represents the maximum salt saturation. The lower image: 3D represents the precipitation of salt at 0.25 cm from the inlet (orange-red) and the initial CO_2 percolation pattern (after 0.4 hour) was added at the right front corner of the 3D volume in blue. Based on the CT scan images, Ott et al., (2015) found that salt precipitated in the vicinity of the initially CO_2 occupied volume, leaving the initial CO_2 pathways essentially open.

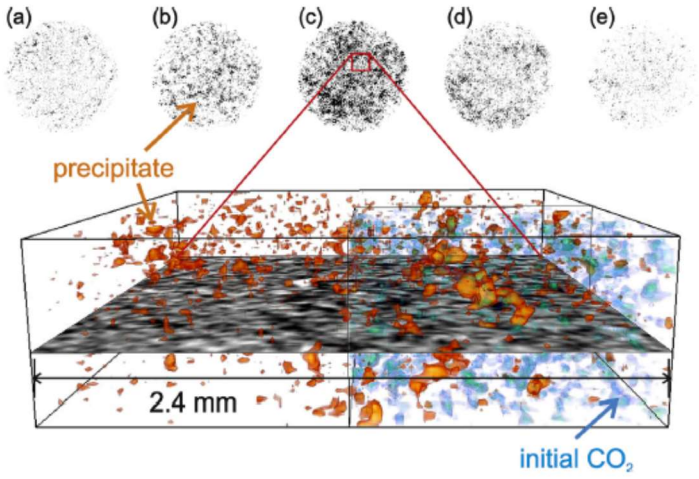


Figure 2-16 µ-CT data recorded with pseudo pore-scale resolution during CO_2 flooding by Ott et al., (2015)

Ott et al., (2015) reported that the experimental findings and numerical analysis showed that under a critical flow rate salt precipitated with an inhomogeneous spatial distribution. This was because of brine and solutes being transported in counter-current flow upstream where salt eventually precipitated.

Also, (Ott et al., 2015) stated that two mechanisms turned out to be of importance, including; 1) the macroscopic solute transport due to capillary pressure gradients, which determines the macroscopic salt distribution (see Figure 2-17), and 2) the pore-scale arrangement of fluid phases during viscous displacement and the drying process (see Figure 2-17). Figure 2-17 shows the microscopic model of fluxes controlling the precipitated salt location for the sandstone case (top row) and the carbonate case. The intergranular porosity refers to macroporosity and the intragranular porosity to microporosity. The letters (a) to (e) refer to the respective capillary pressure levels.

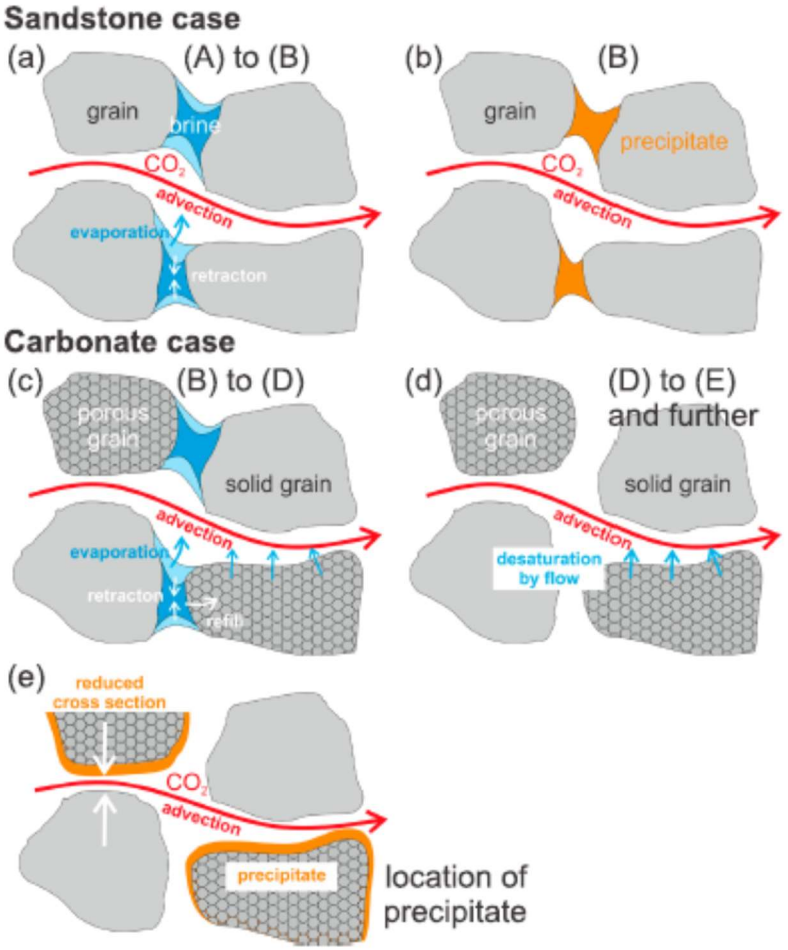


Figure 2-17 Microscopic model of fluxes controlling the precipitated salt location by Ott et al., (2015)

2.1.2 The Effect of Salinity on Dry-out Periods

The effect of salt precipitation on evaporation dynamics and on the different drying stages was investigated by several researchers. Nachshon et al., (2011b) and Nachshon et al., (2011a) assessed the salt precipitation under both the homogenous and heterogeneous conditions and three stages of evaporations under saline conditions were again identified.

In their experimental investigations, two types of salts were used, NaCl and Nal. For the tests, the transparent Poly Vinyl Chloride (PVC) sand columns, 25 cm in height and 5 cm in diameter were used. These columns were backed with homogenous fine Carlo Bernasconi AG (Switzerland) sands with 0.1mm–0.3 mm and homogenous coarse sand with 1mm–1.7 mm and heterogeneous sands (50% of fine and coarse).

An air gap allowed the phase changed of liquid water to vapor. Water content and retention measurements were performed and average pore length were calculated from the air entry pressure values.

The effect of salt on drying periods were summarised in two factors. First factor was the low vapour pressure associated with the salt present in the porous media sample and the second was the reduction of the vapour-diffusion coefficient because of the precipitated salt and the clogging of the core of sample by salt.

Both effect depended on the precipitated salt at the surface of the sample and both effects can be characterised by the Peclet (Pe) number which compares solute transport by advection toward the evaporation front to solute transport by diffusion. The Peclet number is defined as

$$Pe = \frac{U\,\xi}{D^*} \qquad \text{Equation (4)}$$

where U, ξ and D* are a characteristic velocity of the liquid in porous medium, a characteristic ion transport length and the effective diffusion coefficient of the salt in the porous material.

For Pe <<1 diffusive effects are dominant so that the concentration of salt ions remains nearly uniformly distributed throughout the medium.

For Pe=1, crossover behaviour was observed and there is accumulation of ions in the region close to the free surface where evaporation occurs.

When Pe>>1 convection dominates and the ion distribution is characterised by a narrow region of high salt concentration adjacent to the interface where drying occurs (Eloukabi et al., 2011; Sghaier et al., 2007).

Based on (Nachshon et al., 2011b; Nachshon et al., 2011a), three drying stages were identified. Stage 1-during this early evaporation, the drying out of brine solution exhibited a high evaporation rate with minor and gradual decreased in the evaporation rates which appeared to be the same as those for pure water.

Stage 2, the evaporation rate decreased progressively due to the formation of salt crust at the surface of the sample, resulting in decreased rates of evaporation compared to evaporation rates with pure water. However, stage-3 characterised by a further reduction in the rates of evaporation rate.

The transition from stage 1 to stage 2 was initiated when the precipitation of salts crust occurred and this was evidenced by a sharp decrease in the water salt evaporation rate.

However, both stage 1 and stage 2, and even the early stages of stage 3 occurred while the liquid was still hydraulically connected to the evaporation surface. This indicated that the sharp decrease in the salt-water evaporation during stage 2 and parts of stage 3 was because of the salt effect only (osmotic potential and salt precipitation).

In Nachshon et al., (2011b) studies, the selected NaCl solution concentration of 25% which was very close to the NaCl saturation concentration in a solution (26% by weight). The high NaCl concentration of 25% suppressed changes in evaporation rate due to any small changes in solution concentration, permitting the assumption of constant NaCl solution concentration equal to saturation. Thus, all changes in evaporation rate for the NaCl columns were mainly because of the salt precipitation.

Nachshon et al., (2011a) reported that in heterogeneous columns, more than 90% of the salt accumulated within the fine-textured portion as shown in Figure 2-18. In Figure 2-18, the spatial distribution of salt precipitation (NaCl) in heterogeneous half-divided column is illustrated. The white material in Figure 2-18 is the precipitated salt and the fine-textured half is fully covered with salt, while the coarse half was still visible.

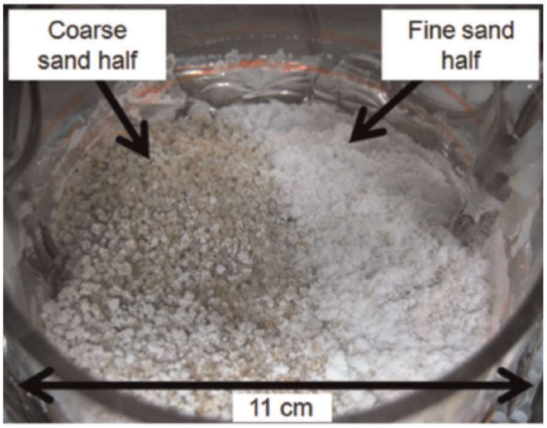


Figure 2-18 Spatial distribution of salt precipitation (NaCl) in heterogeneous half-divided column. The white material is the precipitated salt. The fine-textured half is fully covered with salt, while the coarse half is still visible by Nachshon et al., (2011a)

Under low evaporation conditions, the salt precipitation may accumulate at several discrete locations as well-developed crystals, leaving a large portion of the matrix surface free of salt (Figure 2-19a). Therefore, Nachshon concluded that for low potential evaporation conditions, salt was precipitated in larger, well organized crystals.

However, under high evaporation conditions crystallisation is likely to occur spontaneously all over the fine sand surface, resulting in homogeneous clogging of the surface (Figure 2-19b).

Nachshon et al., (2011b) concluded that denser efflorescent crust was observed for high evaporation rate at the surface. And this dense efflorescent crust exhibited higher resistance to vapour transport. Also, the high evaporation rate resulted in the crystallisation of amorphous and homogeneously distributed salt crystals over the evaporating media. Thus, the media was uniformly sealed by the precipitated salt crust.

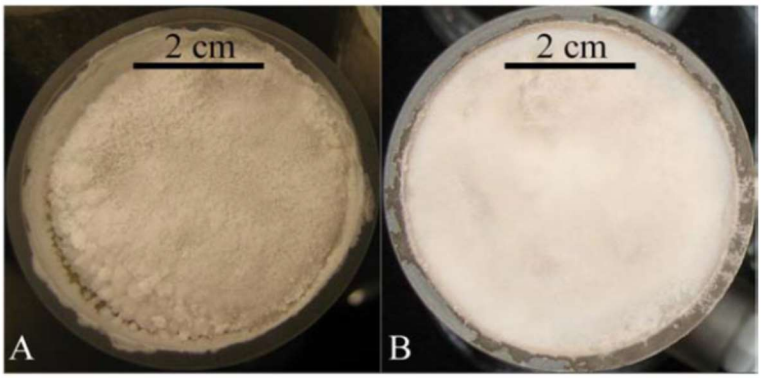


Figure 2-19 Salt precipitations in homogenous columns at low (a) and high evaporation rates by Nachshon et al., (2011b)

Nachshon et al., (2011b) and Nachshon et al., (2011a) stated that the porosity of NaCl crust, which was in the range of 1%–10%, was strongly affected by environmental conditions and this porosity depends on salt depends on salt crystallisation conditions and degree of compaction (Beauheim & Roberts, 2002; Casas & Lowenstein, 1989), 1989). Using the X-ray tomography from a NaCl efflorescence crust, Sghaier and Prat (2009) reported the NaCl porosity with pores dimensions in the range of one to a few tens μm.

Further, Peysson et al., (2011) experimentally investigated the drying rate evolution with time on Vosges sandstone and effect of salt precipitation on the drying rate. The tests covered two conditions of drying process, namely, convective and diffusive.

For diffusive drying conditions, no flow was imposed and the water vapour escape by diffusion, the outlet of the sample was left at the atmospheric pressure. The injection pressure of the gas was small because of the short length of the sample, its permeability, and the gas viscosity.

The drying tests were performed in cylindrical plug of diameter 14.5 mm and length 21 mm. The plug was fully saturated under vacuum with 30g/l NaCl brine. The temperature was carefully controlled in the (Nuclear Magnetic Resonance) NMR measurement zone and checked with a sensor in the glass tube holder (ranging from 30^{o}C to 60 ^{o}C).

Peysson used the Nuclear Magnetic Resonance (NMR) to measure and compare the drying rate dynamics in both convective and diffusive conditions. The used NMR spectrometer was a MARAN 23.7 MHz from Oxford Instruments equipped with a 18-mm diameter probe and 1D imaging capabilities.

From Figure 2-20, it shows that under diffusive drying regime, the average saturation decreased regularly with time except for the very end of the drying process for the three temperatures investigated (30, 45, 58 °C).

It can be from Figure 2-20 that residual saturation of Sw=0.04 cannot be removed even for longer test duration. The effect of temperature on the drying duration was very important, for example at 30 °C it took 300 hours to obtain drying to residual saturation, but only 20 hours at 58 °C.

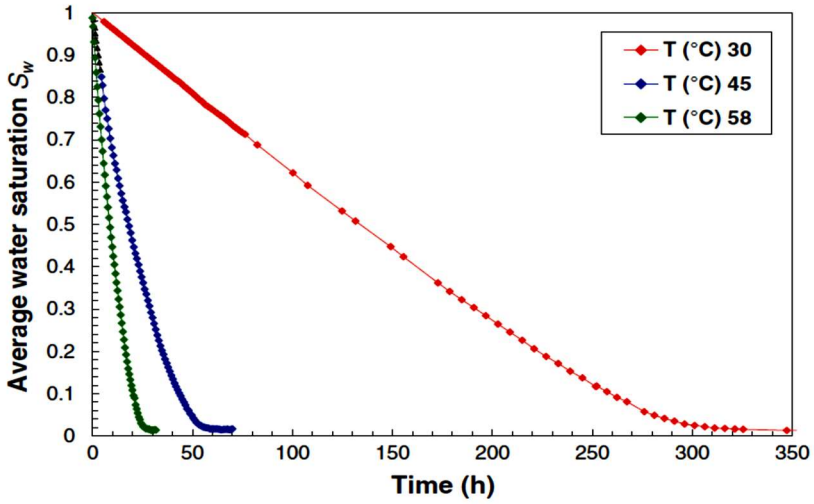


Figure 2-20 2D Average water saturation versus time for convective and diffusive drying test by Peysson et al., (2011)

Figure 2-21 shows the drying rate ξ (kg/m2/h) versus average water saturation under convective and diffusive drying conditions. For the diffusive-driven drying regime as shown in Figure 2-21, the drying rate was not strictly constant but decreases slowly until Sw=0.2 for the three-temperature investigated (30, 45, 58°C).

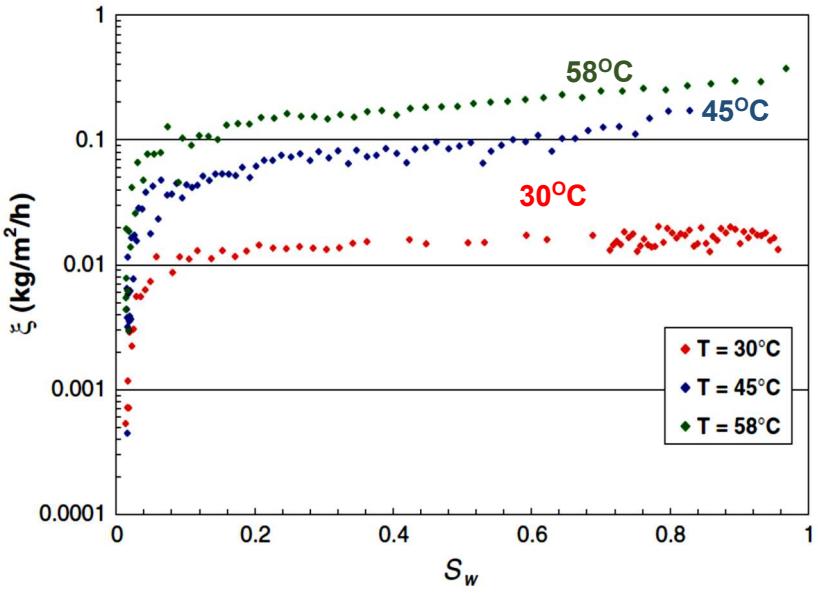


Figure 2-21 Drying rate ξ (kg m-2 hr-1) versus average water saturation for convective and diffusive drying test by Peysson et al., (2011)

Peysson stated that this interesting observation in the drying rates was due the formation of efflorescence at the surface of the sample which was in alignment with reported work by Sghaier et al., (2007) (see Figure 2-22). The calculated Peclet number Pe is 130 (Pe>>1) which confirmed the salt precipitation at the surface of the surface.

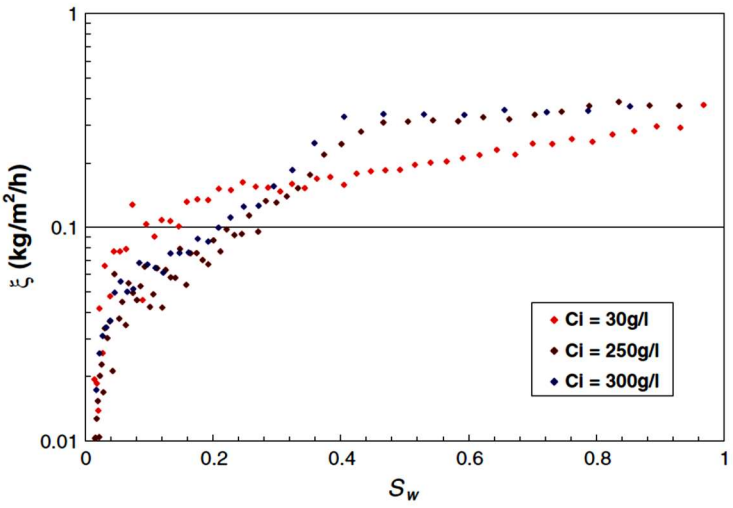


Figure 2-22 Drying rate in kg m-2 h-1 versus average saturation in the diffusion-driven drying regime for three initial NaCl concentrations at 58oC by Peysson et al., (2011)

Norouzi Rad et al., (2013) studied the dynamic of salt precipitation in three-dimensional porous media by using high resolution x-ray microtomography and scanning electron microscopy [HMXST x-ray microtomography system (at 70 kV and 140 μA) with spatial and temporal resolutions of 0.021 mm and 30 min].

The tests were performed using cylindrical columns with 35mm and 11 mm in diameter. The sample was saturated with NaCl solutions of 3.5 Molal (moles of NaCl/kg of water), 4.0 Molal, and 6.0 Molal. The used sand grain sizes ranged from 0.17 to 1.0 mm, with an average size of 0.58 mm. The tests duration of each round was approximately 24 hours.

Figure 2-23(a) illustrates the cumulative of salt precipitation versus the cumulative mass of liquid water lost due to drying. For higher sand concentration of 6.0 Molal, more salt precipitated at the surface for the same mass loss.

Figure 2-23(b) shows the precipitated salt for 3.5 Molal and 4.0 Molal NaCl solutions with time. From this figure, the salt precipitation rate (the *slope* of the line) initially changed with time, followed by a nearly constant value (confirmed by regression analysis).

This transition as explained by Norouzi Rad et al., (2013) corresponded to the time at which all evaporation spots served as the precipitation spots, therefore resulted in an increase to a relatively constant precipitation rate. They further stated that prior to the transition time, due to water evaporation, salt concentration continuously increased at the surface until it reached the solubility limit during brine evaporation. The evaporation spots continually changed to salt precipitation spots.

However, following this transition period in the drying regime, no change occurred in the number of the precipitation spots and salt precipitation continued to form in the already existing spots, resulting in salt precipitation rates relatively constant because of the constant evaporation rate.

Figure 2-24 shows the SEM images of the evolution structural of the salt precipitation at the surface of the sample for NaCl solution of 3.5 Molal and that after after (left) 18 hours and (right) 168 hours with magnification factors of (a) and (b) 150, (c) and (d) 500 and (e) and (f) 2000. The SEM images indicated that the precipitated salt had porous structure during stage 1 even after 18 hours and 1 week of evaporation. Figure 2-24 illustrates the SEM images of the precipitated salt at the surface with different magnification factors after 18 h and 1 week. However, in the later stage of evaporation, the structure of the precipitated salt was modified with salt pores being blocked by further salt precipitation.

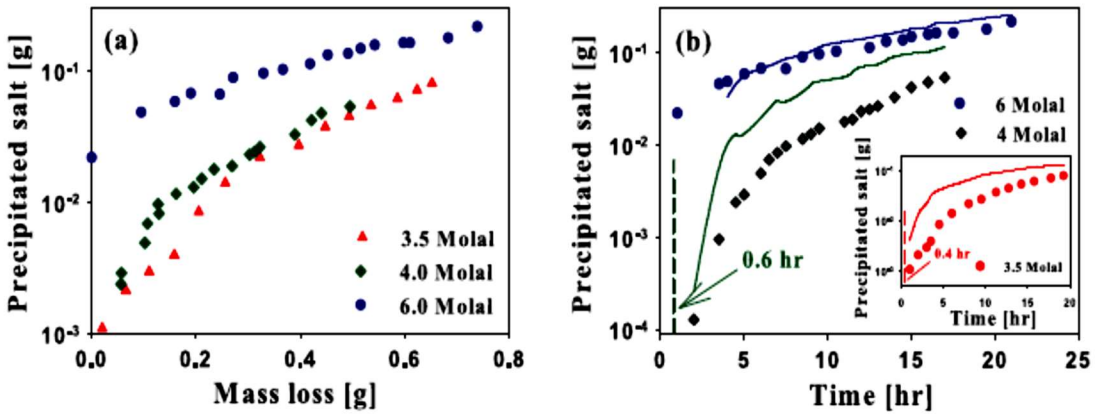


Figure 2-23 (a) Cumulative precipitated salt as a function of the cumulative mass of liquid water lost by evaporation. The legend indicates the initial salt concentration in each evaporating sand column. (b) Time dependence of the cumulative precipitated salt in each sand column by Norouzi Rad et al., (2013)

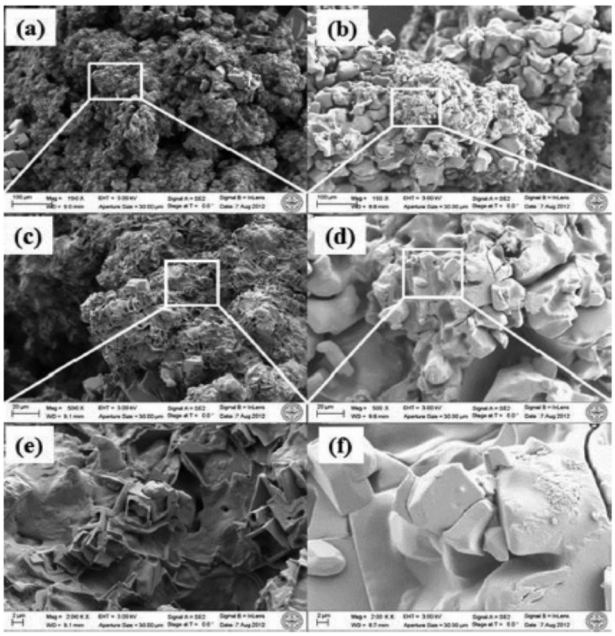


Figure 2-24 The SEM images of the evolution structural of the salt precipitation at the surface of the sample for NaCl solution of 3.5 Molal and that after after (left) 18 hours and (right) 168 hours with magnification factors of (a) and (b) 150, (c) and (d) 500 and (e) and (f) 2000 by Norouzi Rad et al., (2013)

Desarnaud et al., (2015) studied the mechanisms of salt precipitation from porous media, specifically the primary or secondary nucleation. They used NaCl contaminated sandstones. The tests were performed under different relative air humidity including 20% and 50% and air temperature was 21°C.

The objectives of the tests were to study the crystallisation pattern and the drying kinetics of saturated sandstones (porosity ~ 29%, and pore diameter dp~ 30 μm). To assess the impact of the sample size on the drying kinetics, different sample sizes were used [small (4mmx8mm),

medium (8.5mmx8.5mm) and large (20mmx40mm).
X-ray μ-CT was performed at the Centre for X-ray Tomography at the Ghent University (UGCT) using the scanner HECTOR. The resulting voxel size of the reconstructed datasets was 5 μm.

They reported three different regimes including (see Figure 2-25); capillary regime which characterised by a constant evaporation rate, a novel regime in which the evaporation rate decreases exponentially due to the crystal growth that reduces the evaporative surface area and diffusive regime, in which the evaporative flux scales as square root behaviour.

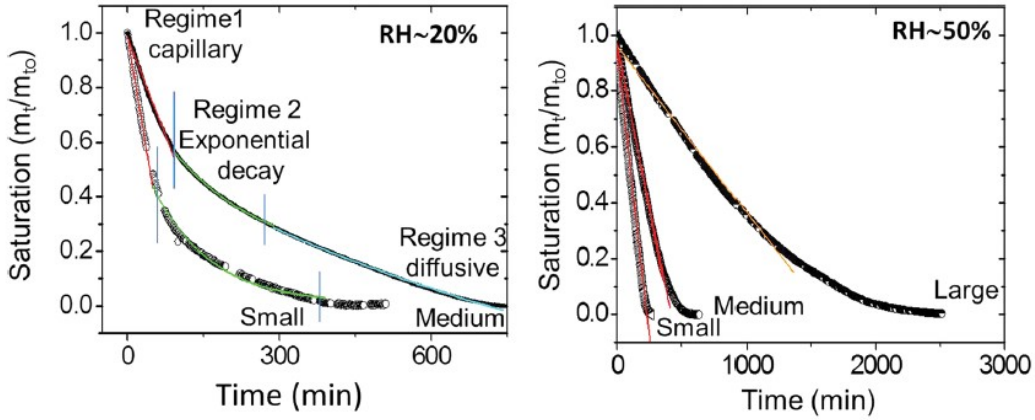


Figure 2-25 Normalized water content at time t (mt/mt0) as a function of time (min) for different sample sizes (large, medium, and small) at two different relative of: (RH =20% and 50%) (Desarnaud et al., 2015)

Figure 2-26 shows the SEM microphotographs of salt crystals at the surface of sandstone at the end of drying of sandstone saturated with salt solution. The top SME shows the drying at RH _20%. (a) and (b) formation of salt skin at the surface and (c) porous structure of this crust layer.

The bottom SEM shows the drying at RH 50%, (d) localised crystallisation. (e) crystallisation between grains probably in the capillary liquid bridges and (f) assemblies of several micro crystallites at the entrance of a pore (cauliflower structure).

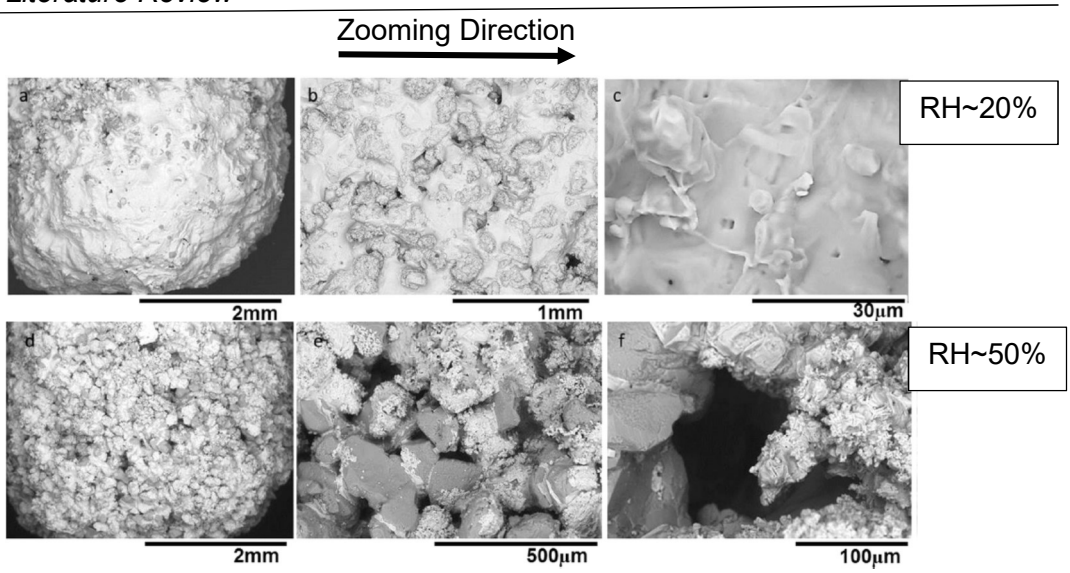


Figure 2-26 Zooming in SEM microphotographs of salt crystals at the surface of sandstone at the end of drying of sandstone saturated with salt solution (Desarnaud et al., 2015)

Desarnaud et al., (2015) reported that in the square root regime, the porous medium was almost completely covered with salt and the speed of the capillary flow through the small pores of the crust was insufficient to overcome the evaporation. In other words, the salt crystallisation was progressed towards the interior of the stone core.

However, in this study in chapter 4, the µ-CT imaging analysis demonstrated that precipitated salt occurred during the square root drying regime at the surface of the sample. This indicated that hydraulic connectivity was maintained to transport salt from the sample core to the surface. Note that some quantity of salt was precipitated in the sample core and that was during the later stage of the square root drying regime.

2.1.2.1 Efflorescent Crusty-Patchy Formation during Diffusive Dry-out

The efflorescent growth of salt during evaporation and the different type of efflorescent growth including crusty and patchy were investigated by several researches. Also, the transition efflorescent crusty–patchy was investigated.

Eloukabi et al., (2013) presented experimental investigation of the evaporation in porous media in the presence of dissolved salt (sodium chloride). Drying experiments were conducted for porous samples consisting of packing of approximately spherical glass beads initially saturated with a NaCl aqueous solution.

Different ranges of bead diameters were used including; (5–50 µm), (50–62 µm), (100–160 µm), (200–250 µm), (250–270 µm), 300 µm and these various ranges were referred to as

range #1, #2, #3, #4, #5 and #6, respectively. The sample used was Plexiglas cylinder with diameter 2 cm and depth 1 cm.

Drying experiments for the various ranges of bead sizes were performed for three initial salt mass fractions, namely 0% (pure water), 12.5% and 25%. It can be noted that the mass fraction 25% was close to the saturation salt mass fraction which was 26.6% for NaCl at 30°C.

Eloukabi et al., (2013) reported during the drying and under saline condition that the evaporation process was characterized by the development of efflorescence at the surface of the porous medium for all the salt concentrations and all the ranges of bead sizes. And two main types of efflorescence were identified in their study namely, the crusty and patchy.

Figure 2-27 shows an example of efflorescence at the end of drying process for salt concentration equal to 25%. Figure 2-27 (a) represents the salt efflorescent regime for range #1 (5–50 μm), and Figure 2-27 (b) represents the range salt efflorescent regime for #6 (300 μm).

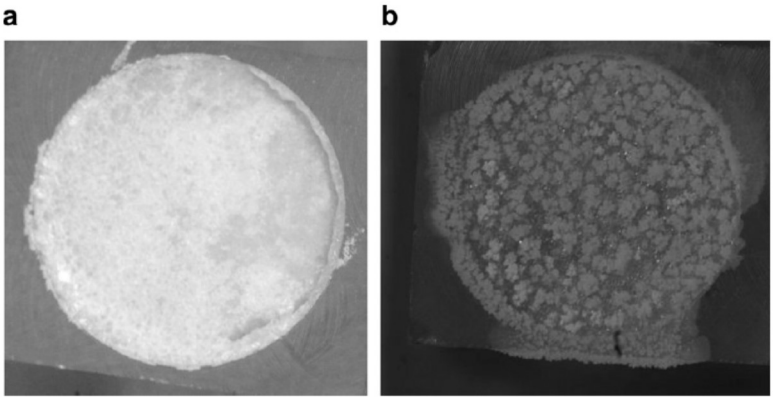


Figure 2-27 Examples of efflorescence at the end of drying process for salt concentration equals to 25%: (a) range #1 (5–50 μm), (b) range #6 (300 μm) by Eloukabi et al., (2013)

Eloukabi et al., (2013) found that for the ranges of smaller glass beads from ranges #1–#3, the efflorescence progressively formed a compact crust covering all the surface of porous medium at the end of drying.

However, for the larger bead sizes ranges from #4 to #6, the efflorescence formed patches with a significant fraction of the surface free. In drying, the fact that the larger pores get dry first as a result of capillary effects contributed to the onset of efflorescence at some specific locations at the surface rather than everywhere. In addition, Eloukabi et al., (2013) found that

the evaporation mass curves were different depending on whether the efflorescence was patch or crusty.

For crust efflorescent, the salt crust that formed at the surface of the porous medium severely limited the evaporation. The blocking of evaporation due to the formation of a crystallised salt crust at the surface of the porous medium was very effective with only a small fraction of the water initially presented in the medium evaporating as illustrated in Figure 2-28 which shows the effect of sand concentration on the evaporation rate and that for small beads sizes (efflorescence was crusty). However, for patchy efflorescent, the evaporation was not significantly limited by the presence of the crystallised salt at the surface of the porous medium. Moreover, the evaporation rate was even greater than with pure water. This was because of the enhanced evaporation surface corresponding to the outer surface of salt pores structures.

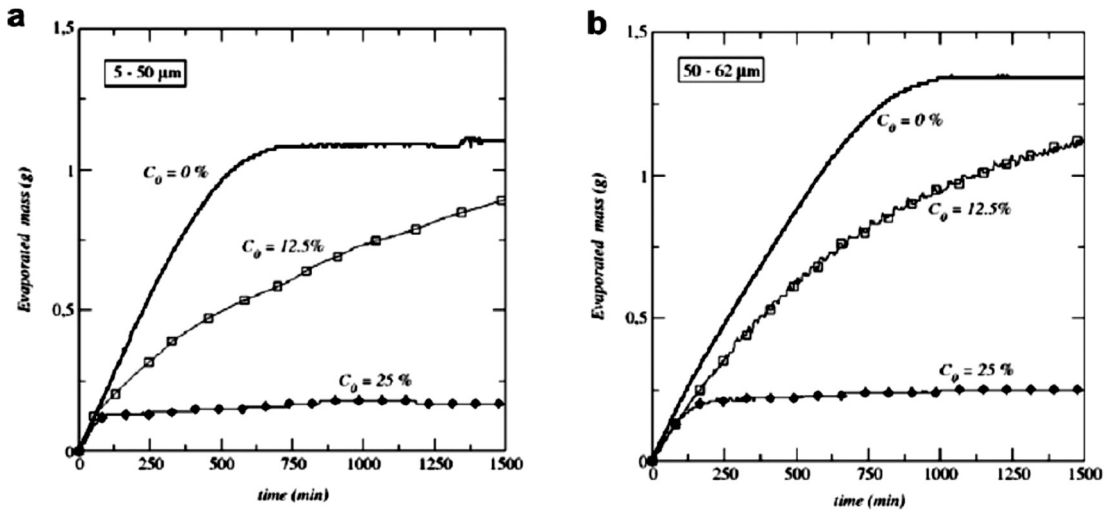


Figure 2-28 Examples of evolution of evaporated mass as a function of time by Eloukabi et al., (2013). (a) bead size ranges from (5-50µm) (crusty) and (b) bead size ranges from (50-62µm) (patchy) (C_o is salt concentration)

Further, the efflorescence growth was studied by Stephanie et al., (2012). Their simple visualisation experiment and Darcy's scale numerical simulations were focused on the impact of permeability and porosity contrasts on the efflorescence formation location.

Stephanie et al., (2012) demonstrated that the porosity was the most sensitive parameter and that efflorescence formed at the surface of the medium of lower porosity. They demonstrated that the efflorescence continued to grow at the surface of the lower porosity medium without spreading over the adjacent surface of the greater porosity medium.

Also, Veran-Tissoires and Prat (2014) studied the efflorescent crusty–patchy formation during the evaporation process and investigated in efflorescent crusty–patchy transition using a simple growth model of efflorescence. The evaporation tests were conducted using glass beads in a 50 mm long hollow cylinder of inner radius 19 mm which formed a porous medium.

The packing cylinder was saturated with a sodium chloride and the initial salt mass fraction was 25 %. The test temperature was controlled at approximately 22ºC and the relative humidity was approximately 7%. Four ranges of bead diameters are then used: (5–50 μm), (50–62 μm), (100–120 μm) and (1–1.125 mm).

Veran-Tissoires and Prat (2014) reported that depending on bead size two main efflorescence type were distinguished during the evaporation process as shown in Figure 2-29. For sufficiently fine porous medium, the efflorescence eventually formed a crust covering all of the porous medium surface, but for a sufficiently coarse, the efflorescence eventually formed a patch pattern as reported by Eloukabi et al., (2013).

In the “patchy” efflorescence, a significant fraction of the porous medium surface was observed remaining free of efflorescence. In Figure 2-29, the ‘crusty’ efflorescence is shown in *(b)* and *(d)* and the second ‘patchy’ efflorescence is shown in *(f)* and *(h).*

Veran-Tissoires and Prat (2014) concluded from the experimental investigations that the patchy efflorescence increased the evaporation rate whereas the crusty efflorescence significantly reduced the evaporation rate which agreed with Eloukabi et al., (2013). The numerical analysis by Veran-Tissoires and Prat (2014) suggested that both the viscous resistance to the flow within the efflorescence and the reduction of water activity at the efflorescence external surface, which both increased with decreasing pore sizes contributed to the patchy–crusty transition.

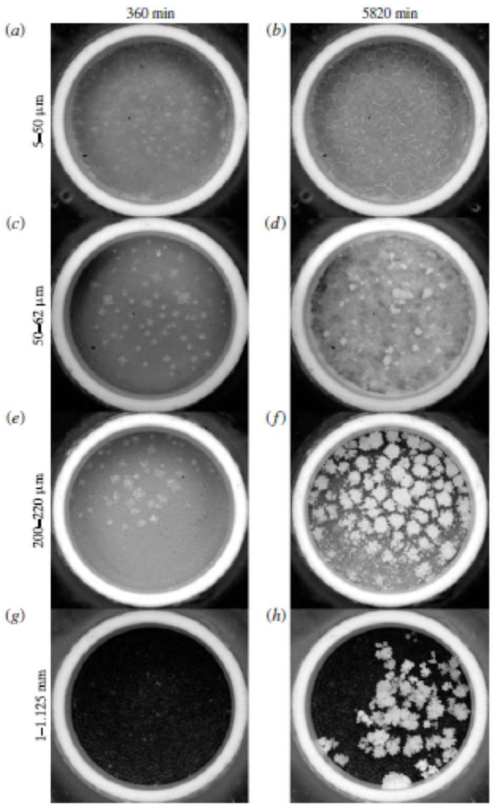


Figure 2-29 Crust and patchy efflorescence patterns obtained by changing the size of the beads forming the porous medium by Veran-Tissoires & Prat (2014)

2.2 Chapter Summary

This chapter provides selective detailed reviews from previous experimental investigations and numerical simulations on the evaporation process and salt precipitation during dry-out in porous media. The drying kinetics during evaporation from porous media for both water and saline conditions were discussed.

The effect of capillarity, viscosity and gravity forces on the different stages of the dry-out stages was addressed through the magnitudes of the dimensionless Bond number, capillary effect and Peclet numbers. The coupling of the evaporation mechanism and salt precipitation location were also explored in this chapter.

Finally, the loss of porosity, permeability, and well injectivity caused by the salt precipitation during formation dry-out were discussed.

The key physics controlling the process were summarised as follows:

- For water – the constant rate period linked to evaporation at the surface and capillary transport of liquid to the surface. The falling rate period and finally the receding front period characterised by square root time dependence and the diffusive transport of water in the vapour phase in the matrix.

- For salt – the development of efflorescence and the consequent reduction of evaporation rate in the crusty configuration. The observations of the location of the salt deposit (patchy/crusty) and the relationship to the pore size heterogeneity.

- When Pe>>1 convection dominates and the ion distribution is characterised by a narrow region of high salt concentration adjacent to the interface where drying occurs.

- The growth of the precipitated salt on the surface can be either patchy or crusty formation. The patchy efflorescence increased the evaporation rate whereas the crusty efflorescence significantly reduced the evaporation rate. The numerical analysis by Veran-Tissoires and Prat (2014) suggested that both the viscous resistance to the flow within the efflorescence and the reduction of water transport at the efflorescence external surface, which both increased with decreasing pore sizes contributed to the patchy–crusty transition.

Chapter 3

3 Experimental Set-up

In this work, we will study the dry-out mechanism during the evaporation process of the De-ionised water and brine solution from porous media. The associated salt precipitation during the drying of brine solution from porous medial was also investigated. In Chapter 3, the experimental apparatus for both water and brine solution tests are presented in this chapter.

For this study, two different classes of experimental set-ups were used in order to generate the drying out and salt precipitation results from porous media: (a) Gravimetric based dry-out experiment and (b) Image based dry-out experiment. The µ-CT images have used to verify the dry-out results obtained from the gravimetric tests.

In Section 3.1, the rock characterisation and properties including sample length, sample width, rock porosity and permeability are presented. The gravimetric based dry-out test set-up for water and brine solution including sample preparation, fluids flooded through the rock, test conditions and procedures are presented in Section 3.2. In Section 3.3, the image based dry-out experiment for brine solution and salt precipitation in porous media are presented. Section 3.3 presents a detailed description of the µ-CT equipment used in this study. The µ-CT image processing methods used to generate the images are presented in Section 3.3.

3.1 Rocks Characterisation and Fluids Properties

Bentheimer sandstone and Ketton carbonate rocks were used for both gravimetric tests and micro-CT in-situ experiments as shown in Figure 3-1. Mercury Injection Capillary pressure (MICP) and X-ray powder diffraction (XRD) were conducted on respective samples to characterize the pore space and mineralogical composition. Tables 3-1 and 3-2 show the basic information, petrophysical properties and mineralogical composition of each rock type.

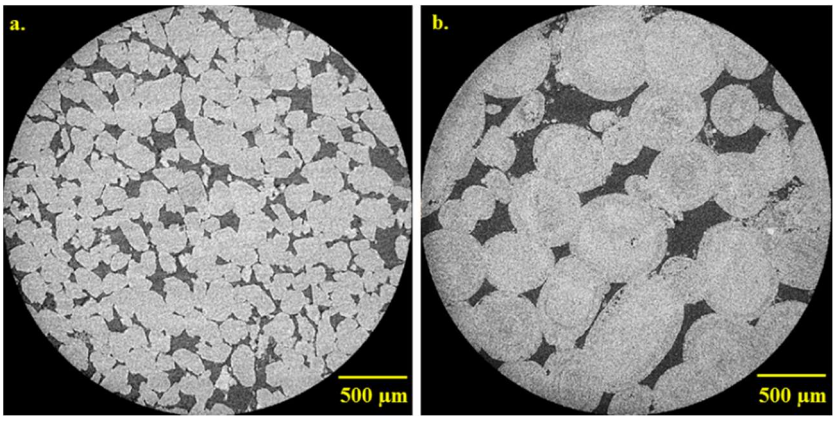


Figure 3-1 Two dimensional cross sections of three dimensional micro-CT images of samples. (a) Bentheimer sandstone. (b) Ketton carbonate

Table 3-1 Basic information about each rock type

Sample	Rock type	Geological group	Place of Origin	Age (million years)
Bentheimer	Sandstone	Bentheimer Sandstone Member	Bad bentheimer, Germany	133-140
Ketton	Carbonate	Upper Lincolnshire Limestone Member	Ketton, Rultand, UK	169-176

Table 3-2 Basic petrophysical properties and chemical composition of each rock type

Sample	MICP Porosity [%]	MICP Permeability [m2]	Calcite [%]	Quartz [%]	K-feldspar [%]	Clay [%]
Bentheimer	20	1.875×10^{-12}	-	95	4	1
Ketton	23.37	2.807×10^{-12}	99.1	0.9	-	-

Figure 3-2 shows the MICP curve for Bentheimer sandstone sample with a well-defined unimodal peak in the pore-throat size distribution representing the total connected porosity exist in the macroporosity with very little microporosity.

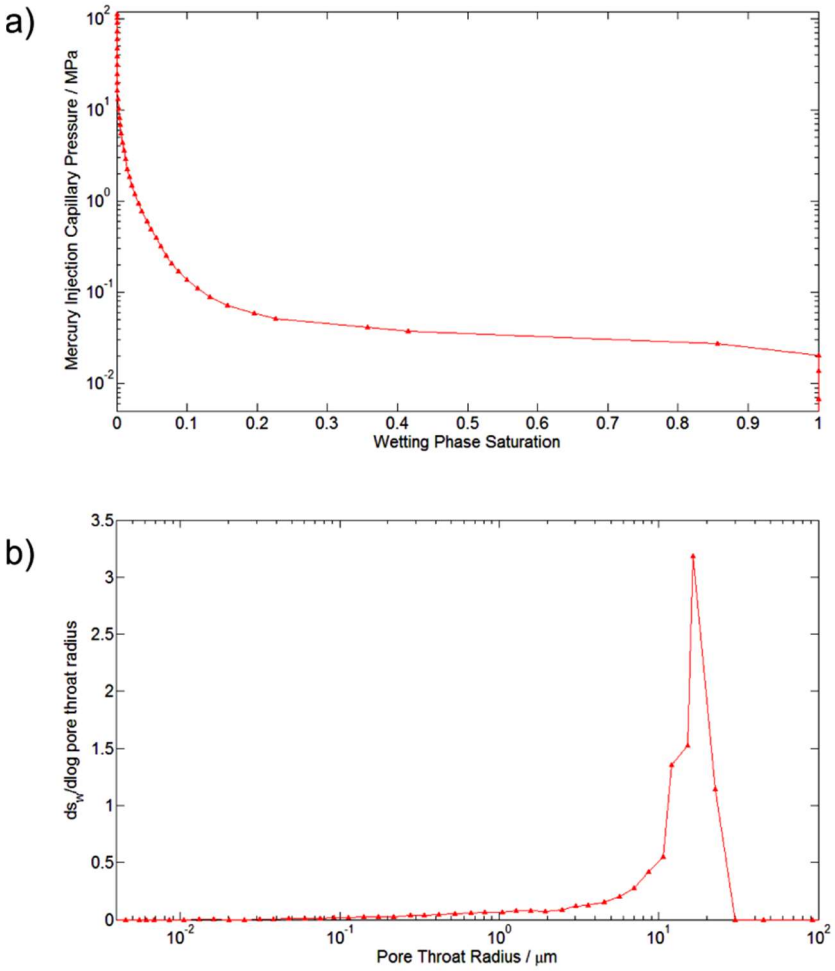


Figure 3-2 a) MICP curve for Bentheimer sandstone. b) Pore throat radii distribution based on measurements of mercury injection capillary pressure (Andrew, 2015)

Figure 3-3 shows the MICP curve for Ketton carbonate which show a bimodal distribution in the pore-throat size distribution, clearly indicating the pore space is composed of both macro and microporosity. As an approximation, 50 % of the pore-throats are from of pores and throats of less than 1 µm in diameter.

Two types of fluids were used in this study: De-ionised water and brine solution. The salt concentration used was 3 Molal and 6.4Molal. The salt used was Sodium Chloride NaCl.

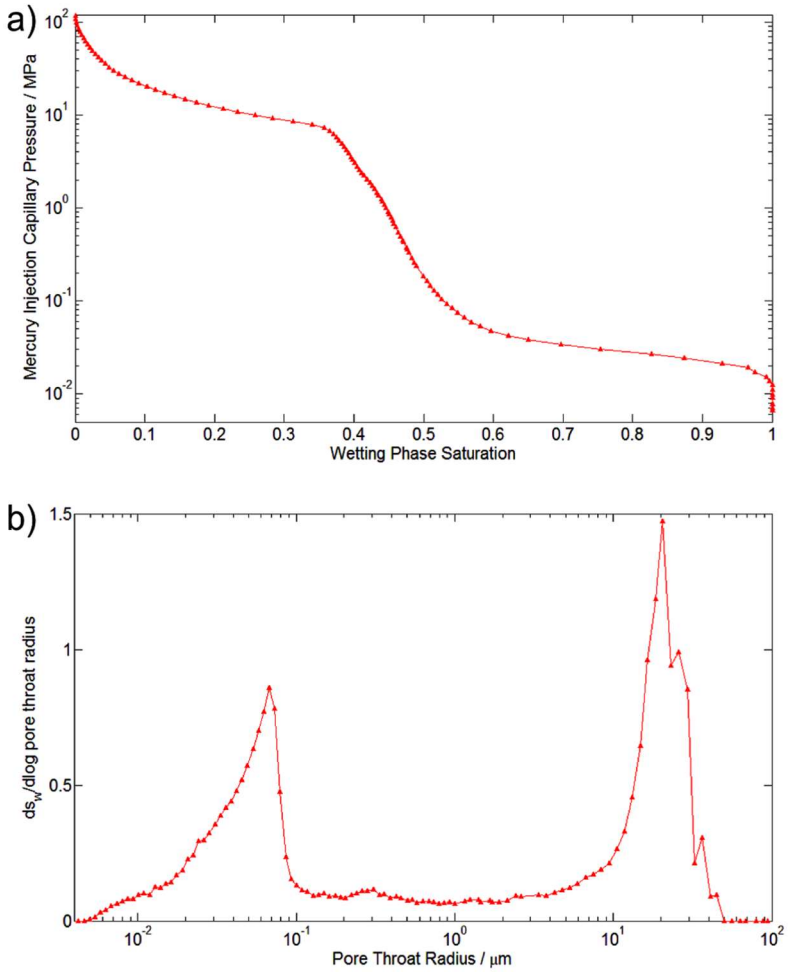


Figure 3-3 MICP curve for Kenton carbonate. b) Pore throat radii distribution based on measurements of mercury injection capillary pressure (Andrew, 2015)

3.2 Experimental Set-up and Test Procedures

In this study, two different experimental set-ups were used to obtain results from dry-out experiments which are as follows – (a) Gravimetric based dry-out experiment and (b) Image based dry-out experiment. Using the manual head drilling equipment, cylindrical cores of Bentheimer sandstone and Ketton carbonate samples were drilled as shown in Figure 3-4.



Figure 3-4 Examples of drilled cylindrical Bentheimer sandstone

Successively, the drilled core samples were allowed to dry into a vacuum oven set at 60°C for 12 hours. In both experimental set-ups, the core sample was wrapped with two layers of aluminum foil with both ends left open.

The wrapped sample was then inserted in a silicon tube to be able to apply a pressurised confining fluid. Table 3 provides a summary of core dimensions used in the respective experimental set-up.

3.2.1 Gravimetric Based Dry-out Experiment

The experimental apparatus was set-up by placing the wrapped core sample inside the Hassler flow cell as shown in Figure 3-5. The flow cell with the core sample was then attached to the flow lines using ISCO pumps and CO_2 gas cylinder and as shown in Figure 3-5.

Prior to any injection, all the flow lines were evacuated sequentially using the vacuum pump. Brine (Composition) and De-ionised water was then filled into the ISCO pumps (pump A and B) for core flood injection and confining fluid respectively. A confining pressure was applied using pump B (De-ionised water).

Initially, the core sample was flooded with 100 pore volumes of CO_2, followed by the introduction of brine from the pump A at the ambient temperature. The core sample was then flooded with 100 pore volumes of brine ensuring 100% saturation of core.

The single-phase permeability was measured using the Darcy flow equation (5) by injecting fluid at five different flow rates and monitoring the pressure drop across the length of the sample using the connected absolute pressure transducers. Once the core flooding

experiment was completed, the core sample was then sealed with impermeable layers and then placed inside the oven as shown in Figure 3-6.

$$q = -\frac{K\ A\Delta P}{\mu L} \qquad \text{Equation (5)}$$

where q is the flow rate, K is absolute permeability, A is the surface area of the sample, L is the length of the sample, μ is the phase viscosity, and the ΔP is the pressure gradient

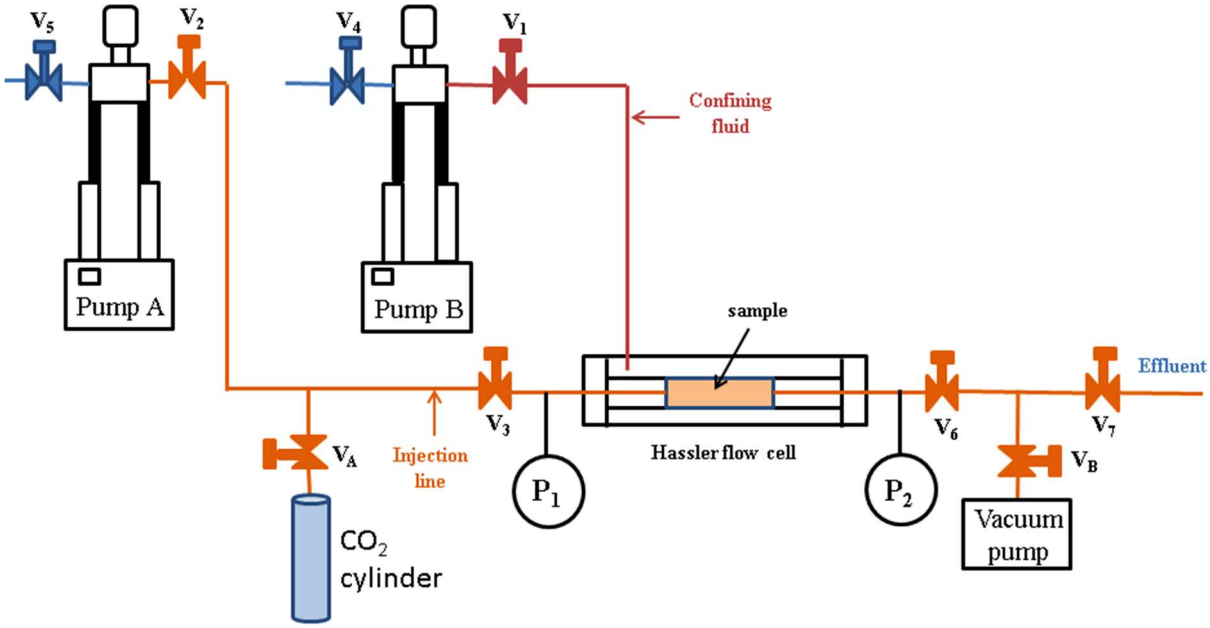


Figure 3-5 Schematic flow diagram representing the apparatus for gravimetric based dry-out experiments

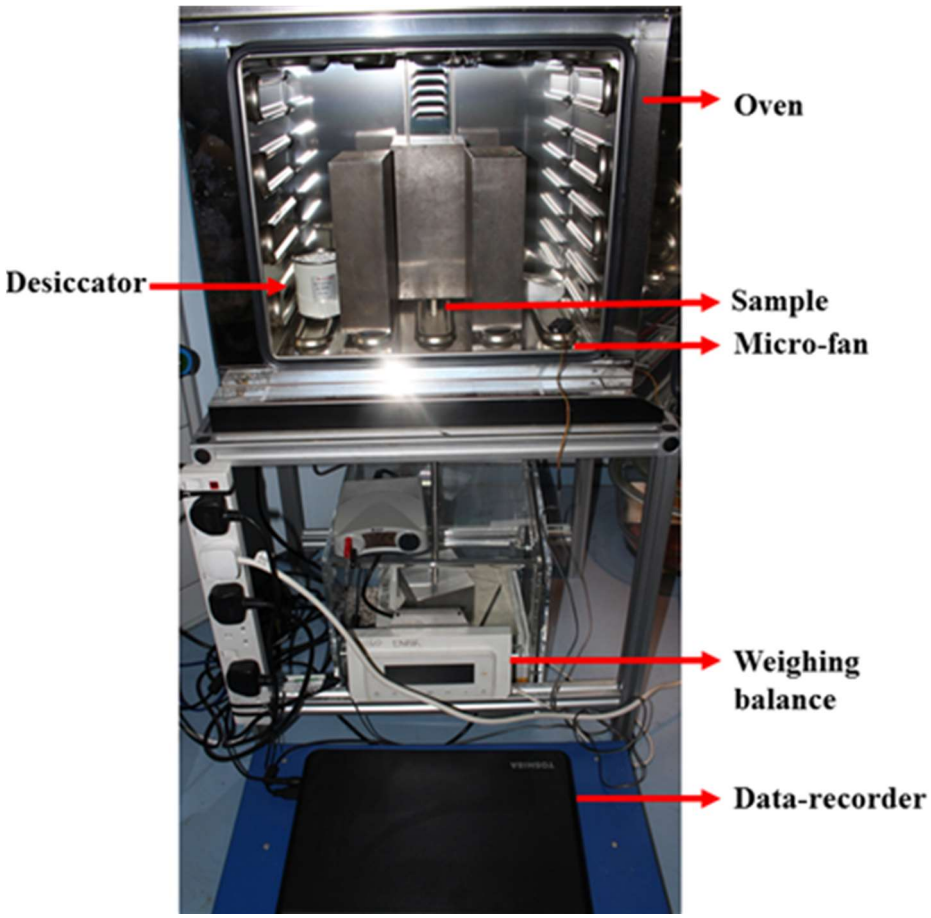


Figure 3-6 Photo represents the oven with equipped desiccator and micro-fan used for drying out test.

The temperature in the oven was increased sequentially from 30°C to 95°C followed by the drying out test. The oven was equipped with desiccants so as to ensure that the air humidity was zero throughout the drying out experiment.

The oven used sited with a micro-fan to guarantee a continuous air flow over the sample as shown in above Figure 3-6.

A hole was drilled at the bottom of the oven to place the sample on the ceramic tube for measuring the water content during the drying test which was connected to the weighing balance. The balance was then connected to a data recorder to read the mass loss using the software SartoCollect. Once the sample reached oven temperature, the top part was removed and mass loss was recorded. The permeability to gas (CO2) at the end of the drying out process were obtained.

3.2.2 µ-CT Based Dry-out Experiment

Image based dry-out experiments were performed using a highly sensitive experimental apparatus as shown in Figure 3-7, in conjunction with lab based Micro-Computed Tomography (Xradia Versa XRM 500) to image in-situ pore scale images of salt deposits in the core samples, further details about the Micro-Computed Tomography is provided later in this chapter in section 3.3.

The basic protocol for each experiment conducted in the micro-CT is given here. Firstly, the wrapped core sample was attached to the end cap metal fittings connecting the core to the pore-fluid flow lines.

The novel set-up of specially made end cap metal fitting at the injection side is shown in Figure 3-8 which has dual inlet ports. It helps to avoid the injection of CO_2 into the core sample matrix, but instead it assists the principle of flow of CO_2 injection through the fracture to achieve the important requirement of this study.

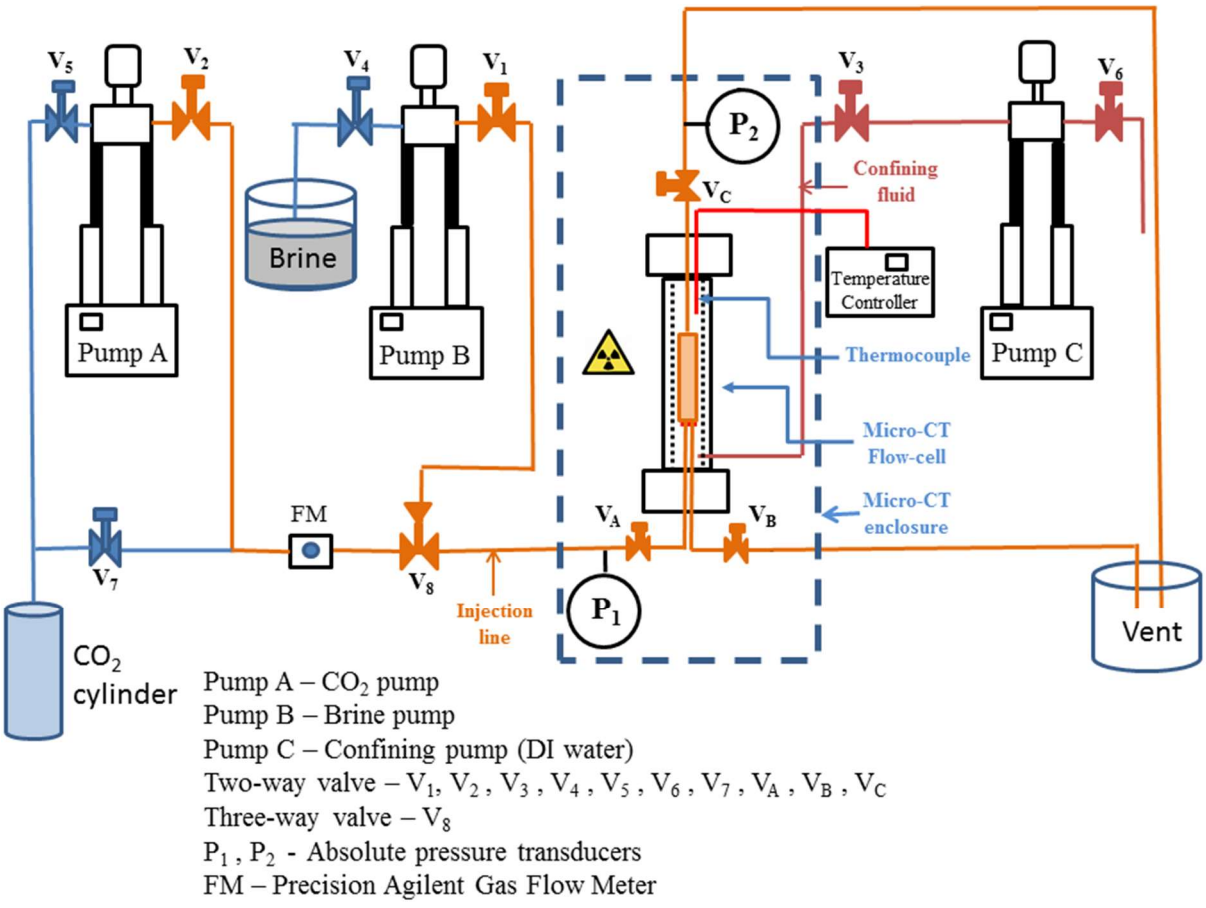


Figure 3-7 Schematic representation of highly sensitive experimental apparatus for in situ image based dry-out experiments

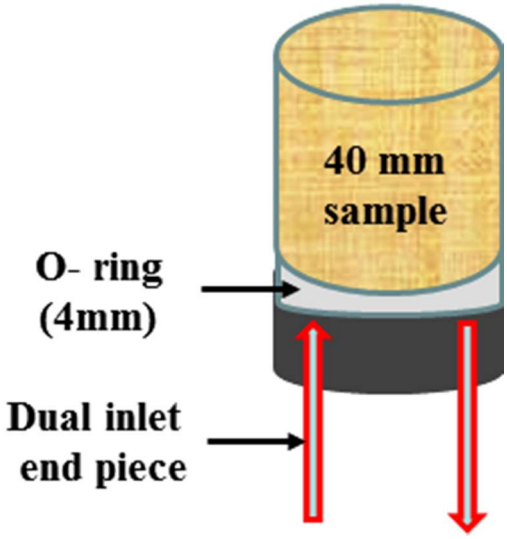


Figure 3-8 Schematic Details of specially made end metal fitting with dual inlet

A flexible heating jacket made up of an extremely thin polyimide (Kapton) heating film was used to surround the core holder. The temperature was measured using a thermocouple sitting in the confining annulus of the flow cell.

The temperature was controlled using a custom built proportional integral derivate (PID) controller which was connected to thermocouple and heating film. The experimental temperature was set at 60°C. The assembled flow cell was clamped inside the micro-CT machine using the stage core holder.

The detailed steps are as follows:

1. The confining annulus of the flow cell was first injected with confining fluid (DI water) and then pressurised at 2 MPa.

2. Open the valve V_A and close the valve V_B. The core sample was then flooded with continuous flow of CO_2 at constant pressure of 1 MPa directly from the cylinder.

3. At this time, X-ray 3D tomography of the core sample was obtained. The voltage was set at 110 kV and power at 10 W for obtaining 3D micro-CT scans.Two sets of 3D micro-CT scans were obtained – scanning the entire diameter of the core sample in the field of view (15 µm), and Higher voxel resolution (6 µm) – zoomed particularly at the inlet of the sample.

4. After obtaining the dry core scans, the core is flooded with 100 pore volumes of brine ensuring the core is fully saturated. The single-phase permeability was measured using the Darcy flow equation by injecting fluid at five different flow rates and monitoring the pressure drop across the length of the sample using the connected absolute pressure transducers.

5. Step 3 was repeated to obtain 3D micro-CT scans of wet core sample.

6. Close the outlet valve V_C and open the dual inlet valve V_A and V_B.

7. The dry-out experiment was then performed by injecting CO_2 directly from the cylinder at very high flow rates (640ml/min) to ensure the humidity is minimal. The flow rate was monitored using precision Agilent gas flow meter connected to the flow loop lines.

8. Step 3 was repeated to obtain 3D micro-CT scans of dry-out core until the end of the experiments. (continuously)

9. Now, shut the CO_2 cylinder. Open the outlet valve V_C and close the dual inlet valve V_B.

10. The final single phase gas permeability was then measured using the pump A by flowing CO_2 at five different flow rates and monitoring the pressure drop across the length of the sample.

11. Reconstruct the scans using the versa software and image processing was done on this images to analyse the evolution of liquid distribution and salt deposition which will be explained fully in the next section.

3.3 Micro- Computed Tomography Imaging and Image Processing

The advent of X-ray computed tomography has made it possible to directly image and reconstruct the complex 3D internal structure of the porous materials. It has been used in medical applications, with recent development in micron scale imaging.

In this study, laboratory based micro-CT scanner Zeiss Versa XRM-500 X-Ray Microscope (see Figure 3-8) located at Imperial College, London was used to obtain 3D pore-scale images of porous media.

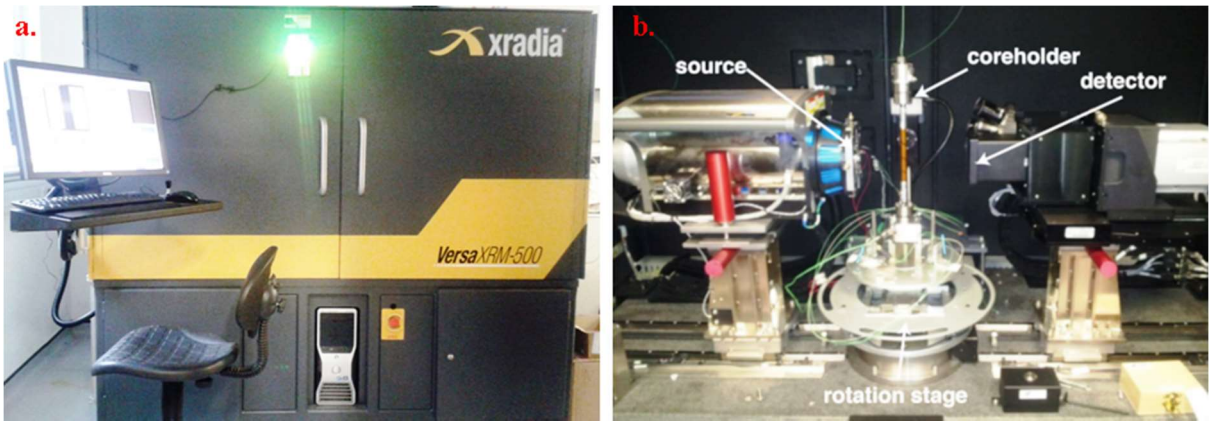


Figure 3-9 (a) Image of laboratory based Zeiss Versa XRM-500 at Department of Chemical Engineering, Imperial College, London. This micro-CT imaging facility is used in this study. (b) The core holder is mounted on the stage in between the source and detector inside the lead x-ray enclosure

The Zeiss Versa XRM-500 micro-CT consists of an x-ray source, scintillator, objective lens and a camera centred around a rotation stage that is enclosed by a lead x-ray enclosure and controlled by Zeiss proprietary imaging software Scout and Scan as shown in Figure 3-10.

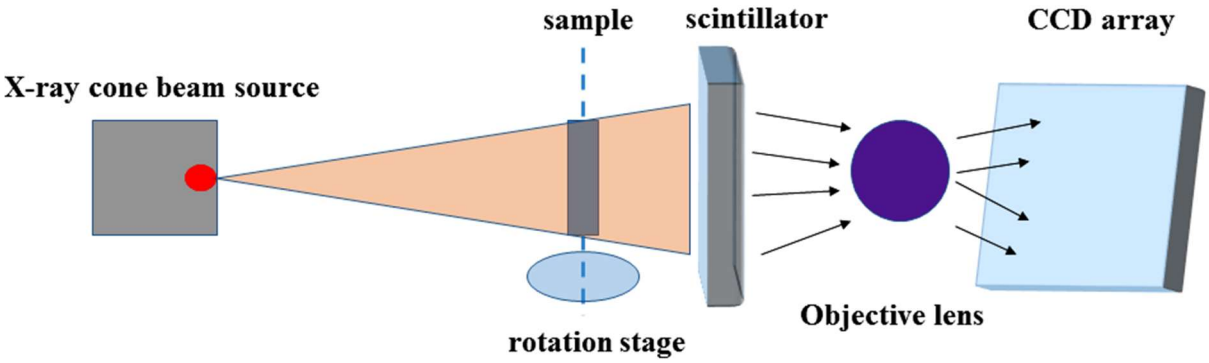


Figure 3-10 Schematic representation of principle of X-ray micro-computed tomography

The X-ray source produces a polychromatic X-ray beam and the projection data (3000 projections) were collected with a cone beam along the circular trajectory. The system uses x-rays to penetrate through the sample and the sample absorbs the part of the X-rays while the rest pass through the sample and hit the scintillator which fluoresces in the visible spectrum.

A pixelated digital image is generated by this visible light which is focused by the objective onto the CCD. The pixel intensity value of the digital image is a function of the number of x-rays that are absorbed by the scintillator. The voltage was set at 110kV and power at 10W for obtaining the entire library of 3D micro-CT scans acquired in this study.

The detector was set as close to the sample as possible. This maximizes the signal – noise ratio and minimizes the phase contrast. In this cone beam set-up, the voxel resolution was controlled by the proximity of the sample to the beam or X-ray source.

3.3.1 Image Processing

After acquiring the 3D pore-scale images, image processing acts as a link to connect grey scale micro-CT data to be fully analysed and extract key petrophysical properties. Image processing consists of two main stages, including; image enhancement and image segmentation as described below.

3.3.1.1 Image Enhancement

The signal to noise ratio of acquired micro-CT images can be improved using image enhancement by removing artefacts causing misclassification of different phases during segmentation (Gonzales & Wintz, 1987). In the literature there are many digital filters available like edge-preserving noise reduction, mean, Gaussian (Gonzales & Wintz, 1987) and anisotropic diffusion (Perona & Malik, 1990).

These filters work on the principle of smoothing and blurring algorithms. In the mean filter, each voxel's greyscale value is replaced with the mean value of its neighbour while the Gaussian filter works in the same way using the Gaussian weighted mean.

These filters work well for reducing noise but in this study images consist of multiple discrete phases and these filters tend to blur phase boundaries leading to ambiguous segmentations. In our study, the best filter algorithm is chosen to smooth out the noise while preserving the phase boundaries (edges) of genuine resolvable features and to remove less important information at the same time.

The most promising and recently developed denoising algorithm is the non-local means filter used in this study which combat the limitation of simple filters (Buades et al., 2005; Buades et al., 2008). Non-local means filter is a linear filter where the greyscale of a certain voxel is replaced by the average of the grey-scales of other voxels.

In contrast to the standard mean filter, the edges are preserved by assigning each voxel a weight proportional to an index measuring the similarity of the weighted voxel to the voxel being replaced within the search area which could be as large as the entire image. The filter

is very computationally expensive, therefore uses a small local search window and implemented in two-dimensions.

In this study, raw 3D reconstructed images were filtered using the non-local means edge preserving filter within Avizo Fire 8.1 (www.vsg3d.com). The 3D image data sets were acquired subsequently at different stages of experimental cycles such as dry state, wet state and continuously during the dry-out sate.

The time scale to perform these in-situ experiments is quite large and this leads to small movements in the sample and imaging equipment. This may cause difficulties in analysis of images at different state compared with reference dry scans. Thus, all the images were registered to a reference image of choice (in this case an initial dry scan).

The registration technique used is normalised mutual information which starts with a user-supplied initial guess. The mutual information is then weighted by the similarity and uses the closest value to align the image (Li, 1990).

All the 3D data sets acquired at different states are registered with the reference dry scanned image. During the dry-out experiments, it is necessary to compare the acquired 3D data sets in the time series and hence the images must be resampled after image registration. A registered image is realigned to a reference image. During this process the voxels are translated, rotated, scaled such that the transformed image grid is no longer aligned to the grid of the reference image.

In order to realign the grid, the registered image is resampled along the reference grid. There are 3 main types of resampling module present within the Avizo 8.1. Lanczos resampling method is the most robust resampling method than nearest neighbour and standard resampling method.

The Lanczos method performs a multivariate interpolation of the registered image by mapping each sample point to a translated and scaled copy of the Lanczos kernel which is then evaluated at the new grid point (Burger et al., 2009; Lanczos, 1950). Once the images were registered and resampled, the difference imaging method was applied to time series data sets which helped to evaluate changes in structure and fluid arrangements by analysing the change in greyscale value in each successive image. This method has been successfully applied to the micro-CT data sets analysing the physics of salt precipitation (Ott & Oedai, 2015) and characterising the microporosity in the sample (Buffiere et al., 2010).

3.3.1.2 Image Segmentation

A process to decide which phase each voxel in 3D micro-CT image belong to is called segmentation. Different segmentation method exist to help automate the segmentation process such as global thresholding, region growing –local segmentation and watershed segmentation. The simplest method of segmentation is global thresholding.

The globally defined grey-scale threshold is assigned to one phase and any grey-scale above the threshold is applied to another. This method is more effective for images with exactly two distinct phases and high signal to noise ratio. However global thresholding does not work for noisy images or for multiple discrete phases due to voxel misidentification, particularly at the phase boundaries causing errors called partial volume effects.

In the past, geological CT images are segmented into pore and grain space using the complex segmentation methods. A two-phase high precision bead pack was segmented using the K-means cluster analysis algorithm (Porter & Wildenschild, 2010).

The converging active contours (CAC) segmentation method was effectively used on sandstone (Knackstedt et al., 2006; Sheppard et al., 2004). Otsu's thresholding algorithm in ImageJ software was used by (Gharbi & Blunt, 2012) to segment 3D dry carbonate rock images into binary images consisting of pore and grain phase. In general, the main aim of all these segmentation methods is to differentiate the phases by detecting similarities and discontinuities in intensity grey value and partitioning the phases accordingly with the help of different edge detection algorithms and labelling similar regions of each phase.

In this study, a seeded watershed algorithm was used to segment 3D micro-CT images which relies not only on the intensity of an image but also on the gradient magnitude of an image with the seed generated by the use of 2D histograms (Andrew et al., 2013; Jones et al., 2009; Shah et al., 2015).

3.3.2 Image processing routine: 6 µm data

The tomographic images were reconstructed using proprietary software provided by Zeiss and processed using Avizo-9 software. Figure 3-11 – Figure 3-14 show a complete workflow of image processing and segmentation procedure, which is described in the following sections.

3.3.2.1 Image processing and segmentation of the dry rock (dry scan)

Figure 3-11 (a) shows a two-dimensional vertical cross-section of a raw tomogram of dry a Bentheimer sample (before saturating with brine/water). The image was cropped to remove

the distorted outer regions and external walls.

Firstly, the image was filtered with a non-local means edge preserving filter to improve signal-to-noise ratio Figure 3-11 (b). The tomogram was then segmented into two phases with a seeded watershed algorithm based on the grey-scale gradient and grey-scale intensity of each voxel Figure 3-11 (c).

The rock phase in Figure 3-11 (c) (light blue) was used as a mask for time-series dataset containing brine and salt phases as well; this is explained further in the next section.

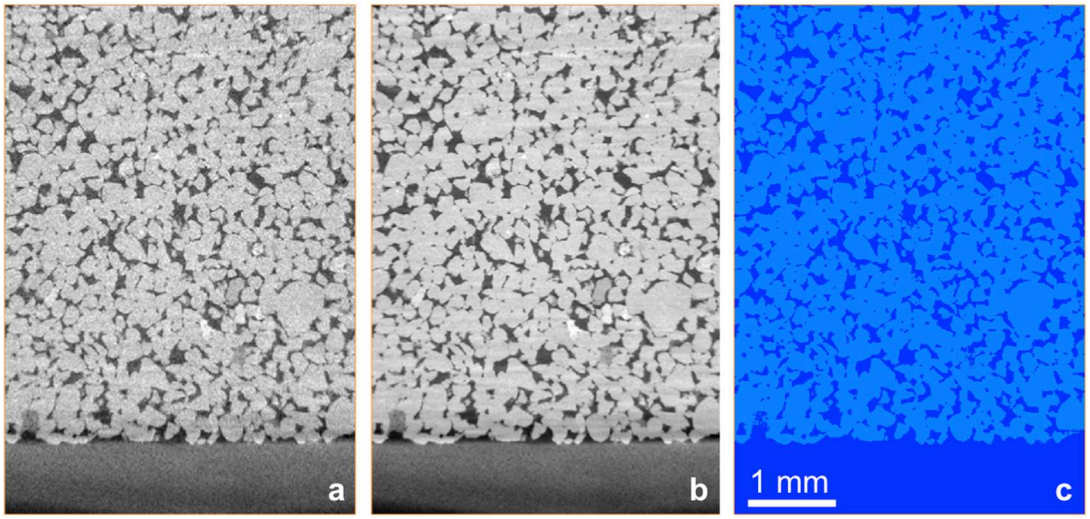


Figure 3-11 Image processing of the dry rock sample. (a) Two-dimensional vertical cross-section of a raw image. Here, black and grey represent pores and rock respectively. (b) Filtered image using nonlocal means edge-preserving filter. (c) Two-phase segmented image with dark blue and light blue as pores and rock respectively.

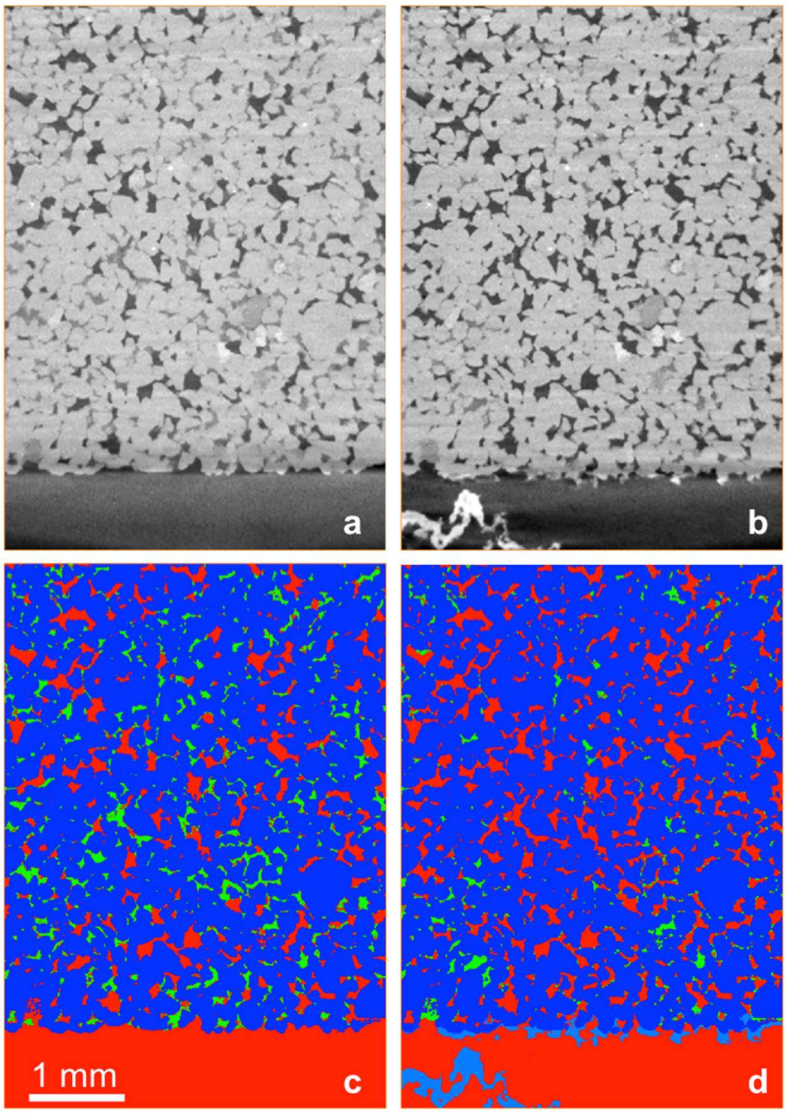
3.3.2.2 Three-phase segmentation of the brine-air-rock system

For segmenting the three-phase data containing brine/water (dark grey), air (black) and rock (light grey) phases (shown in Figure 3-12 a), the image was first segmented (here called initial-segmented) into air and the rest of the phases (air as label-1 and the rest as label-2) using a watershed algorithm. The rock mask from **Error! Reference source not found.**Figure 3-11 (c) was then applied as a mask (by making the rock phase as label-0) on the initial-segmented image.

An arithmetic filter (A+1) was applied to obtain the rock as label-1, air as label-2 and brine as label-3 (here A is the image to be processed), therefore, resulting in a three-phase segmented image, shown in Figure 3-12 (c). In some images, it was noticed that the initial-segmentation created an unwanted brine layer between air and the rock phases Figure 3-13 (b). To correct this brine layer, the brine phase was isolated Figure 3-13 (c).

The grain phase was expanded into the brine phase by dilating the grain phase by 1 pixel. This removed the unwanted brine layer, but also removed some portions of the actual brine phase. To correct this, the brine was dilated by 1 pixel. An arithmetic filter (A+1) was applied on it, and finally the actual grains were applied as a mask on it, which resulted the air phase as label-1 and the brine phase as label-2, as shown in Figure 3-13 (d)

Although, this treatment expanded the brine phase back but removed 1 pixel layer of air phase adjacent to the brine phase Figure 3-13 (d). To correct for it, the air phase was isolated (Figure 3-13 (e), and was dilated by 1 pixel. An arithmetic filter (A+1) was applied on it, and the grains were applied as mask on it to obtain the final corrected image Figure 3-13



(f).

Figure 3-12 Three- and four-phase segmentation. (a) & (b) Filtered image of the air-brine-rock (3-phase) and air-brine-rock-salt (4-phase) systems respectively. (c) & (d) Segmented images of Figure 3.12 (a) & Figure 3.12 (b) respectively.

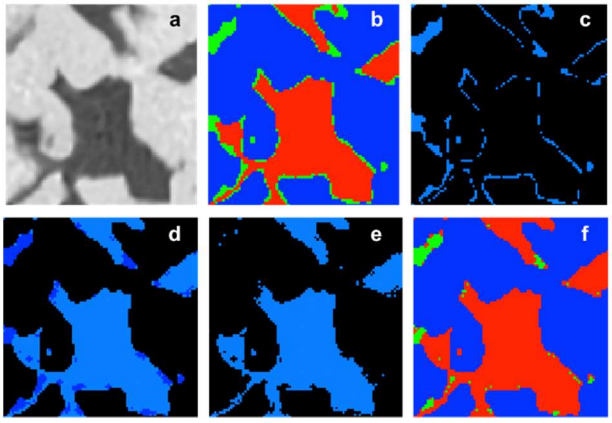


Figure 3-13 Brine layer correction. (a) Filtered image. (b) 3-phase segmented image with unwanted brine layer. (c) Isolated brine phase. (d) Brine and Air after rock and brine dilation. (e) Isolated air phase. (f) Final corrected image.

3.3.2.3 Four-phase segmentation of the brine-air-rock-salt system

For segmenting the four-phase data containing brine/water (dark grey), air (black), rock (light grey) and salt (white) phases Figure 3.12 (b), the image was first segmented into two-phases, i.e., salt with the highest attenuation (white colour in Figure 3.12 (b) and the rest of the phases.

This segmentation is here termed as Seg-1. The salt phase from Seg-1 was used as a mask in the next step. Similar to the salt segmentation, the air phase (black) and the rest of the phases Figure 3.12 (b) were segmented from the filtered image using a watershed algorithm. Here, this segmented image is called as Seg-2.

The salt from the previous step (from Seg-1) was applied as a mask on the air-segmented image Seg-2, resulting in a three-phase segmented image (here called as Seg-3) containing air, salt and the rest. Then the rock phase from Figure 3.11 (c) was applied as a mask on the three-phase segmented image Seg-3, resulting in the final four-phase segmented image as shown in Figure 3.12 (d)

Similar to the three-phase segmented images, sometimes an unwanted brine layer appeared between air and the rock phases. This was corrected by applying the same image processing protocol as used in three-phase data processing described in the previous section. The final segmented data was used for qualitative analysis (3D visualization) and quantitative analysis such as phase volume fractions.

3.3.2.4 Sensitivity analysis

A sensitivity analysis of the segmentation process was performed based on variation in intensity thresholds. A subset of the data at t = 18.8 hr (Figure 3.12 (c)) was selected for this analysis. The air phase was under- and over-segmented by varying the intensity threshold

between 7524 and 7724, which resulted in difference in phase segmentation qualitatively. The resulted value of air saturation was 0.675 ± 0.017, giving an error (standard deviation) of 2.5 % of the mean value.

3.3.2.5 Brine connectivity analysis

To find the connectivity of the brine phase, the brine phase was isolated from the 3-phase and 4-phase segmented image with brine as label-1 and the rest of the phases as label-0. A label analysis algorithm was applied on the brine phase, which labelled disconnected brine clusters with different colours and label values as shown in Figure 3.14 that represents disconnected brine clusters of the brine phase of Figure 3.12 (c). Note that the brine that appears to be disconnected in this image could be connected through thin films that were not captured with the current image resolution with a voxel size of 6 µm.

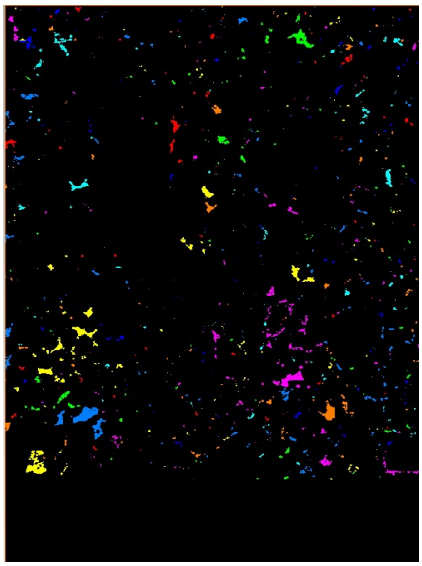


Figure 3-14 Disconnected brine cluster analysis. The brine from Figure 3.12 (c) was isolated, and the disconnected brine clusters were labelled with different colours and label values.

3.3.3 Image processing routine: 15 µm data

Figure 3.15 (a) shows a two-dimensional vertical cross-section of a non-local means filtered image with a voxel size of 15 µm, containing air (air), brine (dark grey) and rock (light grey) phases. The image was cropped to remove the outer distorted regions by applying a cylindrical mask. The tomographic images were segmented using the same image processing routine as for 6 µm datasets described in the previous section Figure 3.15 (b) shows a two-dimensional vertical cross-section of the three-phase segmented image. The segmented image was used for three-dimensional volume rendering for qualitative analysis and volume fractions for quantitative analysis.

For comparing the 15 µm and 6 µm datasets, a further subset of the 15 µm image was obtained (marked by the white dotted box in Figure 3.15 (b), the size of which was equivalent to the 6 µm dataset. Both the datasets (i.e., 6 µm the cropped 15 µm datasets) were compared quantitatively by analysing phase volume fractions and qualitatively by visual inspection. This provided information on the effect of image resolution on the findings of this study.

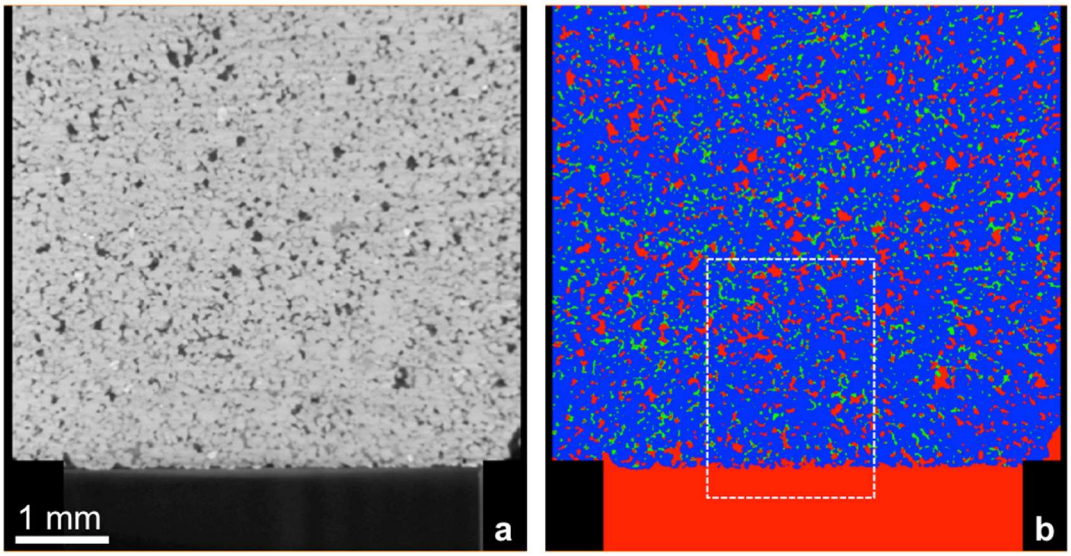


Figure 3-15 Image processing routine for 15 µm dataset. (a) Two-dimensional vertical cross-section of a filtered image containing air (black), brine (dark grey) and rock (light grey). (b) Three-phase segmented image. Here red, green and blue represent air, brine and rock phases respectively. The white dotted box indicates the region where a subset was taken for comparison with the 6 µm dataset.

Chapter 4

4 Evaporation and Salt Precipitation: Results and Discussions

This chapter describes firstly the water, brine and salt precipitation results based on the gravimetric test method. The impact of the sand particles size, sample length and CO_2 temperature on the kinetics drying curve are presented in this chapter. The analysis of the critical saturation and end effect of film connectivity are addressed. Salt precipitation effect on drying process is presented in this chapter. The X-ray CT images for different sample length which are saturated with brine are presented as well together with salt precipitation images and its impact on the sample porosity and permeability.

4.1 Gravimetric Dry-out Tests Results and Discussions

4.1.1 Gravimetric Evaporation Tests Matrix

The objectives of this series of gravimetric dry-out tests were to assess the;

1) The De-ionised water evaporation process and associated drying-out stages and that for Bentheimer sandstone and Ketton carbonate rocks.
2) The effect of circulated air temperature at sample surface approximately zero relative humidity on the De-ionised water dry-out and drying curve (rock selected was Bentheimer sandstone)
3) The effect of sample length on the evaporation process and drying stages for De-ionised water
4) Brine evaporation and associated drying-out stages and salt precipitation at sample surface and that for salt (NaCl) concentration of 3.0 Molal and 6.4 Molal

The test matrix for this series of tests is presented in Table 4-1.

Table 4-1-Gravimetric dry-out tests series

Sand stone rock types	Sample length (mm)	Sample diameter (mm)	Saturation Fluid	Brine concentration (Molal)*	Oven Air Temperature (°C)**
Bentheimer Sandstone	~20	~6	De-ionised water	-	30
					60
					90
					95
	~20	~12	De-ionised water	-	60
	40				
	82				
	242				
	40		NaCl	3.0	
				6.4	
Ketton Carbonate	80	~12	De-ionised water	N/A	
	40		NaCl	3.0	
				6.4	

**Moles of NaCl/kg of water*
*** air relative humidity (RH) is approximately zero*

CT (micro computed tomography) scans were taken at the end of the dry-out test in this study at the end of the dry-out tests to check that the precipitated salt.

4.1.2 Dry-out during Evaporation of Pure De-ionised Water Results and Discussions

4.1.2.1 Air Temperature Effect on De-ionised Water Evaporation

To study the effect of air temperature on De-ionised water dry-out, series of experimental investigations for the drying rate evolution with time was performed under different air temperatures: 30°C, 60°C, 90°C and 95°C. In this study, the used samples dimensions and Bentheimer sandstone characteristics are listed in Table.4-2 below.

Table 4-2-Bentheimer Sandstone characteristics and sample dimensions

	Bentheimer Samples			
Temperature °C	30	60	90	95
Length (mm)	19.50	20.50	21.00	20.50
Diameter (mm)	5.80	6.20	6.40	6.40
Porosity (%)	20.00	22.31	23.55	22.91

Core flooding experiments were performed using pure water on the Bentheimer sandstone samples. The samples were initially 100% saturated, with air circulation on top of the samples and desiccants were placed inside the oven to measure the humidity. The core sample was flooded with 100 pore volumes of CO_2, followed by the introduction of De-ionised water. Gravimetric measurements were recorded as a function of time at 30°C, 60°C, 90°C and 95°C.

Figure 4-1 shows the de-ionised water accumulations with time and that for different air temperature of 30°C, 60°C 80°C, 90°C and 95°C and at approximately 0% air relative humidity (RH) and that for different Bentheimer porosities and in different samples dimensions

The slope of the cumulative mass loss (g) versus time (hrs) indicates the evaporation rate. It can be observed from Figure 4-1 that the de-ionised water mass slope was nearly constant for the early stages of evaporation followed by a lower slope which corresponded to the second stage of evaporation.

At 2.0hrs, the De-ionised water cumulative loss during evaporation for air temperature of 90°C and 95°C was approximately 0.15 (g) compared with 0.13 (g) and 0.06 (g) for 60°C and 30°C, respectively. The different in the total mass loss for different air temperature was mainly due to the difference in the used Bentheimer characteristics (porosities) and samples dimensions as shown in above Table 4-2.

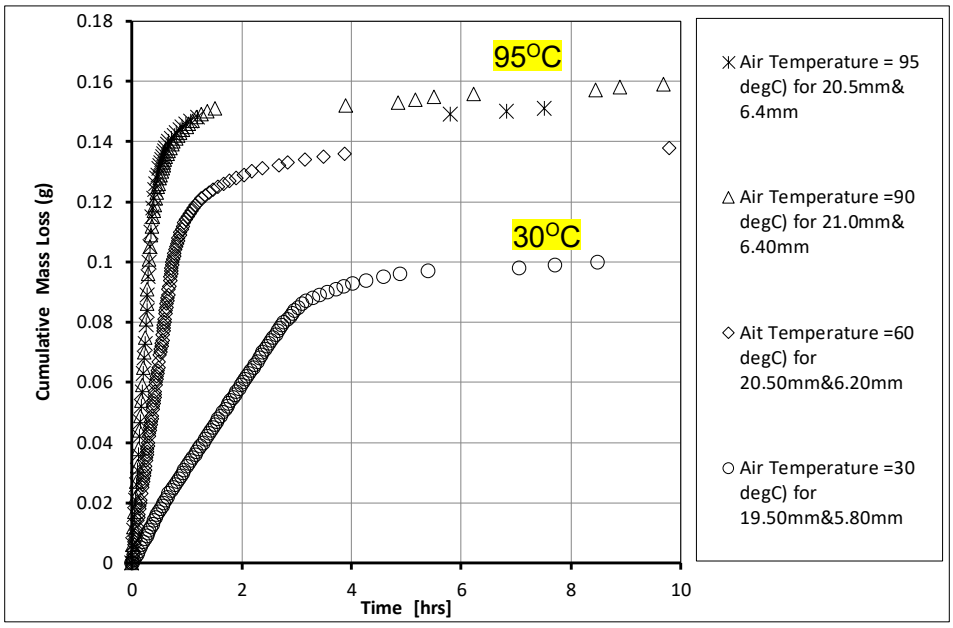


Figure 4-1 Cumulative mass loss of De-ionised water for different Bentheimer sandstones porosities with time (hrs) at different air temperatures

Figure 4-2 shows the De-ionised water saturation with time and for different air temperatures (30°C, 60°C, 90°C and 95°C) and at relative humidity (RH)~0%. At approximately zero relative humidity, the evaporation behaviour of different sample lengths consisted of two main drying regimes: first, constant rate period (CRP) which was characterised by sharp decrease in water saturation linearly with time as shown in Figure 4-2. In this drying regime or stage, the capillary forces control the flow of the liquid to the sample surface (liquid-air interface).

Due to the capillary effect, the liquid films were attached to the sample surface, this period is noted as capillary regime in Figure 4-2. The dotted line in Figure 4-2 represents the transition from the constant dry period to falling rate period and that for 30°C, 60°C, 90°C and 95°C.

In Figure 4-2, the capillary regime stage ends at 3.5hrs at S_w=0.13 and at 1.0hr at S_w=0.17 for 30°C and 60°C, respectively. This indicated that the drying out at 60°C was 3.5 times faster than at a lower temperature of 30°C. This can mostly be explained by the difference in the vapour pressure of water between the two temperatures; 4247 Pa and 19950 Pa at 30°C and 60°C, respectively. The vapour pressure ratio is 4.7. However, for 90°C, the transition occurred at 0.4hr and at S_w=0.26. For 95°C, the transition occurred at 0.4hr and at S_w=0.20. From Figure 4-2, it is shown that by increasing the air temperature further, the De-ionised water evaporation rate increased. This increase in the evaporation rate was due to the increase in the vapor pressure from 70117 Pa at 90°C to 84529 Pa at 95°C.

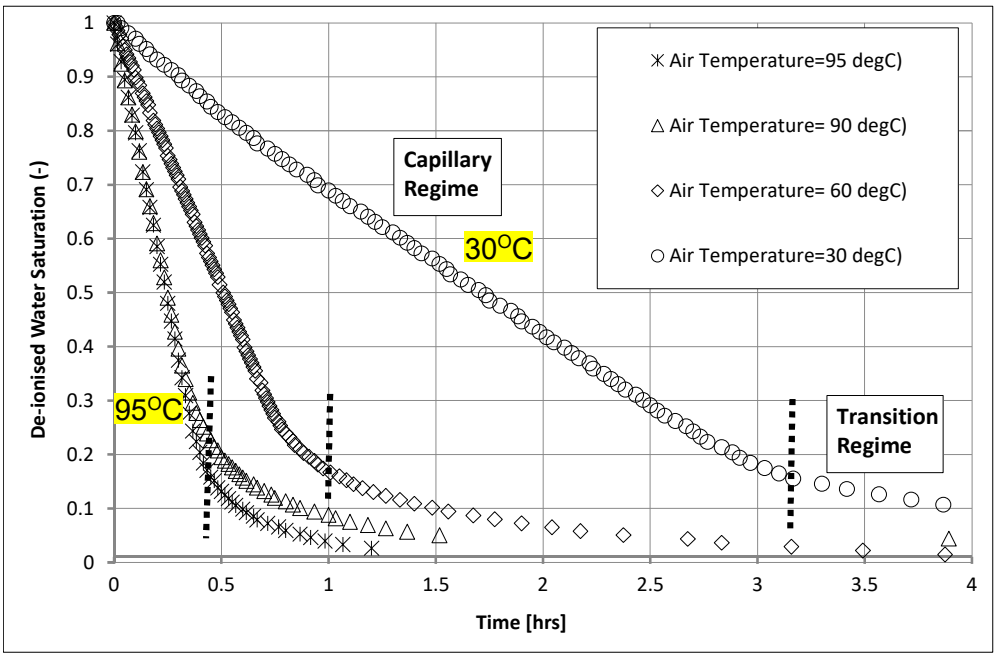
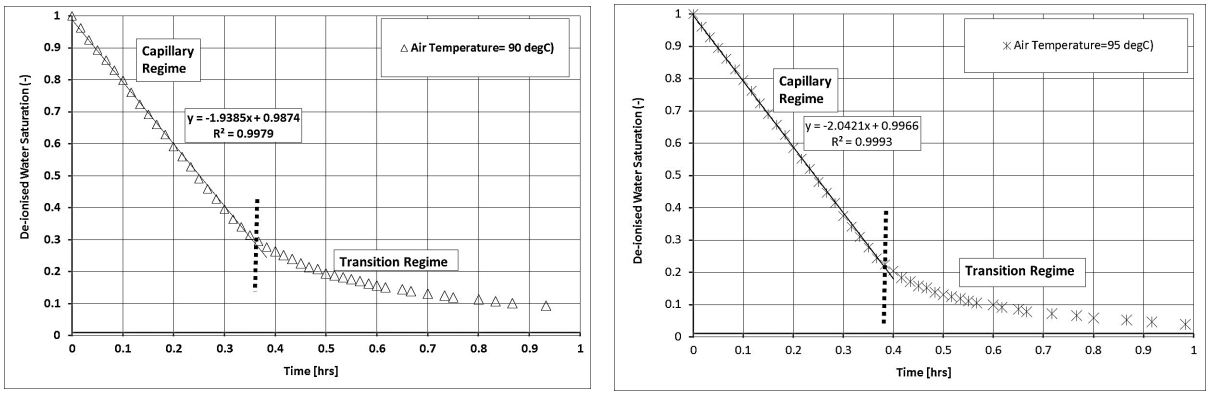


Figure 4-2 Saturation of De-ionised water for Bentheimer sandstone at different air temperatures

In Figure 4-3 (a, b) the transition from the constant rate period to the falling rate period is presented and that for 90°C and 95°C air temperatures. Figure 4-3 shows that during the capillary driven dry-out regime, the saturation decreases linearly with time, however for the diffusion driven dry-out regime the saturation decreases in square root behaviour. The observed drying regime reported in this study was aligned with the previous work presented in the literature review (Chauvet et al., 2009; Lehmann et al., 2008; Shokri et al., 2009a). As stated in literature, the extent of capillary-driven regime depends on the external mass transfer conditions (air temperature and relative humidity) and pore size and it is larger for the fine pores (Lehmann et al., 2008). This constant rate period ends when the hydraulic continuity with the surface is disrupted and that is because of the downward gravity and viscous forces which overcome capillary driven force.

During, the falling rate period (FRP), which was noted as transition regime, the saturation no longer decreases linearly in time, but follows a square root dependant. In this period, the downward gravity and viscous forces overcome the upward capillary driving force, disrupting hydraulic continuity with the surface, resulting in lower evaporation rate limited by diffusion through the porous media as stated by Shokri et al., (2009a), Lehmann et al., (2008), Shokri et al., (2010b), and Shokri et al., (2009b). This transition from capillary-driven regime to diffusion-driven regimes marks the liquid film detachment from the surface of the sample.

However, in this study in short length samples, this transition occurred due to very low water residual left in the short sample length of approximately 20mm during stage -1 of evaporation which was very low to sustain the hydraulic connectivity. The liquid film detachment will be explained later in this section.



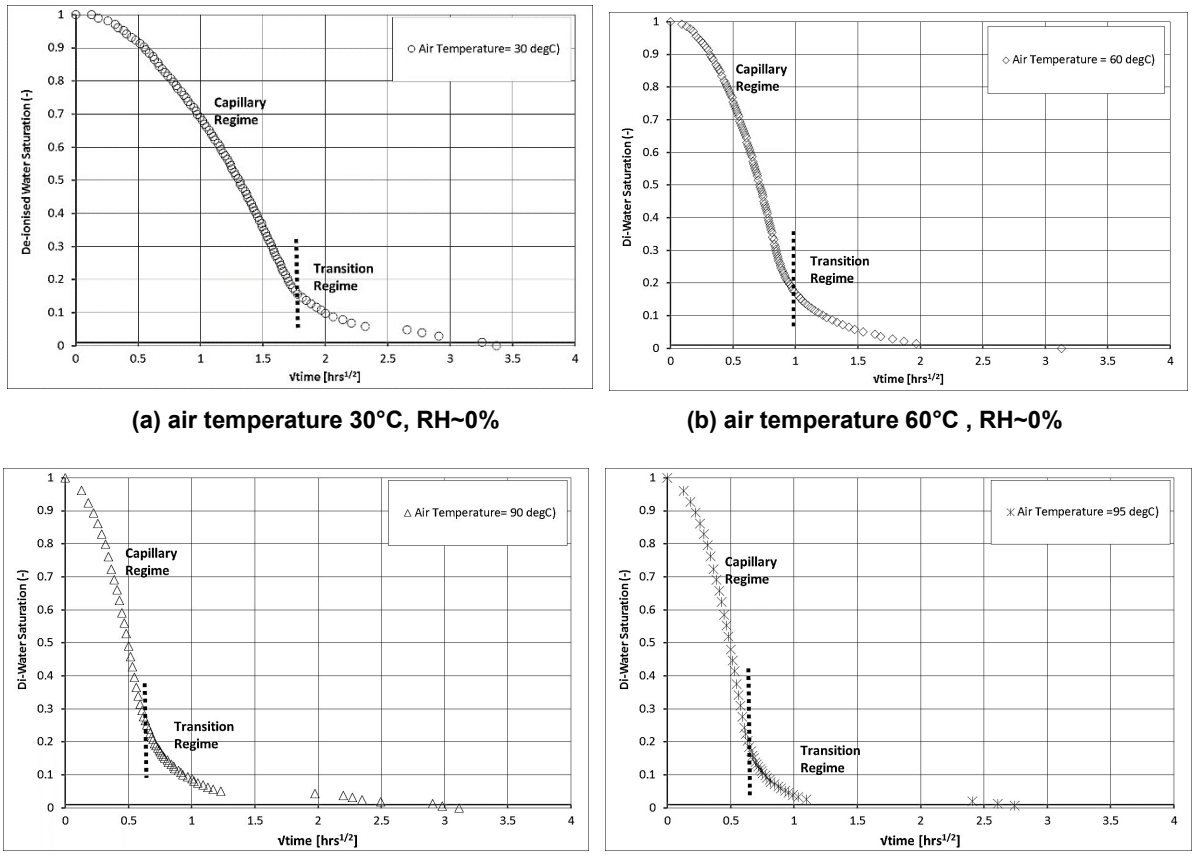
(a) air temperature 90°C, RH~0% **(b) air temperature 95°C , RH~0%**

Figure 4-3 Saturation of de-ionised water in Bentheimer sandstone at 90 °C and 95 °C air temperatures in different sample dimensions as in Table 4-2

Figure 4-4 (a, b, c, and d) shows the de-ionised water saturation with square root of time and for different air temperatures (30°C, 60°C, 90°C and 95°C) and at relative humidity (RH)~0%. The dotted line in Figure 4-4 (a, b, c, and d) represents the transition between the capillary and diffusion dry-out regimes.

It can be seen from Figure 4-4 that the transition from capillary dominant drying regime to square root behaviour were at ~[$t^{1/2}$=1.8hrs$^{1/2}$], [$t^{1/2}$ =1.0hr$^{1/2}$] for air flow temperature of 30°C and 60°C, respectively. However, for 90°C and 95°C, the transition occurred much faster and at [$t^{1/2}$ =0.60hr$^{1/2}$] and that for different sample dimensions as shown in the above Table 4-2.

Based on the experimental investigations of air temperature effect on evaporation of the De-ionised water, the effect of increasing the temperature on drying rate is evident. The value of average water saturation decreases rapidly, with consequent increase of the drying rate, when temperature increased.



(a) air temperature 30°C, RH~0% **(b) air temperature 60°C , RH~0%**

(c) air temperature 90°C , RH~0% **(d) air temperature 95°C , RH~0%**

Figure 4-4 Average saturation of de-ionised water in Bentheimer at different air temperatures in different samples dimensions as in Table 4-2

4.1.2.2 Sample Length Effect on Pure De-ionised Water Evaporation

To study the effect of sample different lengths on De-ionised water dry-out and on the liquid film detachment (CRP transition to FRP), series of experimental investigations for the drying rate evolution with time was performed under different sample length including, 19.07mm, 40mm, 82.02mm and 242mm and at air temperatures 60°C at approximately 0% air relative humidity. The samples dimensions and Bentheimer sandstone characteristics used for this study is presented in the below Table.4-3.

Table 4-3-Bentheimer Sandstone characteristics and sample dimensions

Bentheimer Samples				
Temperature °C	60 °C			
Length (mm)	19.07	40.0	82.02	242
Diameter (mm)	11.58	11.65	12.1	12.4
Porosity (%)	20.55	22.01	22.19	23.72

Figure 4-5 shows the log scale for the average De-ionised water mass accumulations with time for different sample lengths (19.07mm, 40mm, 82.02mm and 242mm) at air temperature of 60°C and at approximately 0% air relative humidity. It can be seen from Figure 4-6 that the average cumulative mass loss (g) of De-ionised water is 0.5(g) for 19.07mm sample length compared with 1.0 (g) for 40mm, 2.0 (g) for 82.02mm and 4.0 (g) for 242mm. However, for 242 mm, the mass loss increased to 7.0 (g) at the end of the drying-out test.

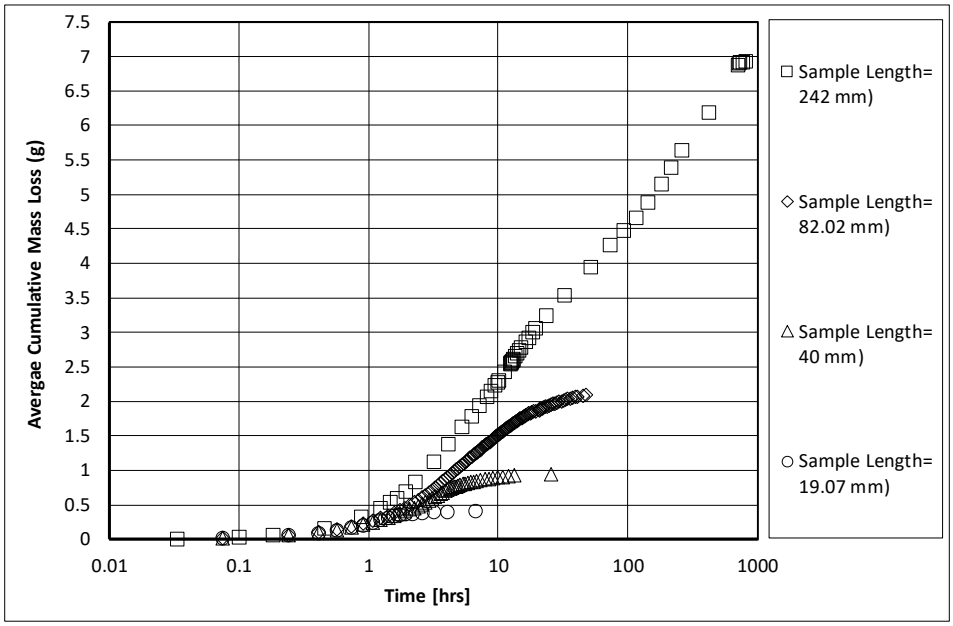


Figure 4-5 Average cumulative mass loss of De-ionised water for for Bentheimer samples of different length at temperature 60°C, RH~0%

Figures 4-7 shows the De-ionised water saturation with time at 60°C air temperature and RH~0% and that for 19.07mm, 40mm, 82.02mm and 242mm. From Figure 4-7 (a), in 19.07mm sample length and 11.58mm diameter, the average De-ionised water saturation reached S_w=0.2 after 1.50hrs. This mean that 80% of the pure water (De-ionised) sample was dried out during capillary regime, however, the left water residual in sample of 20% was unable to sustain the continuity of the hydraulic connectivity due to short sample length.

Similar drying behaviour was observed also for 40mm sample length (S_w= 0.22 average saturation at 4.0hrs, see Figure 4-7 (b). By increasing the sample length to 82.02mm, the time required to achieve average saturation of S_w=0.4 occurred at 6.0hrs, Figure 4-7 (c). For 242mm sample length, the average saturation reached S_w=0.53 when the transition to the diffusion dry-out regime occurred at 25hrs. It can be concluded that the square root behaviour regime was more distinct in 82.02mm and 242mm samples lengths.

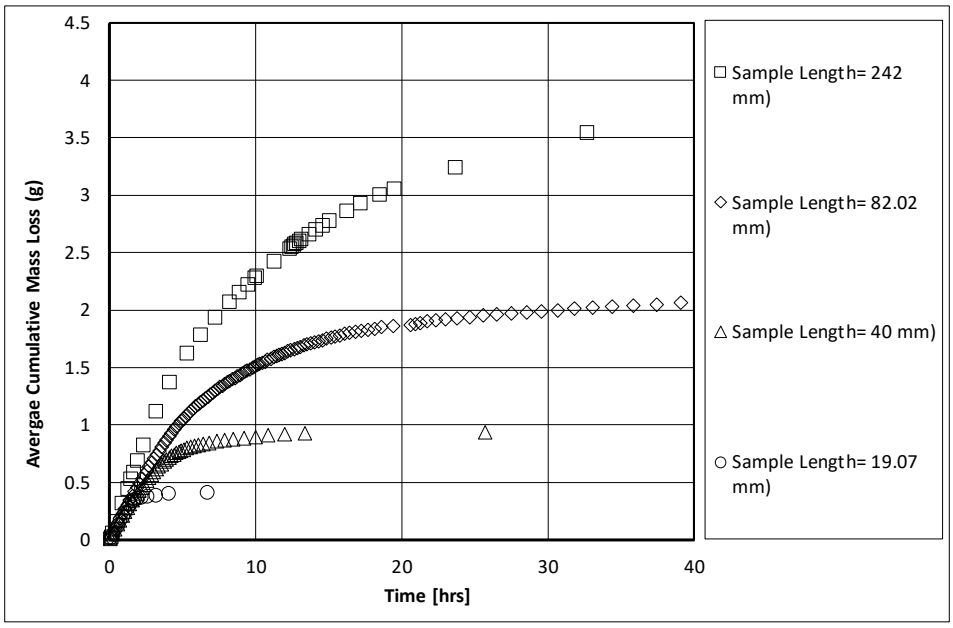
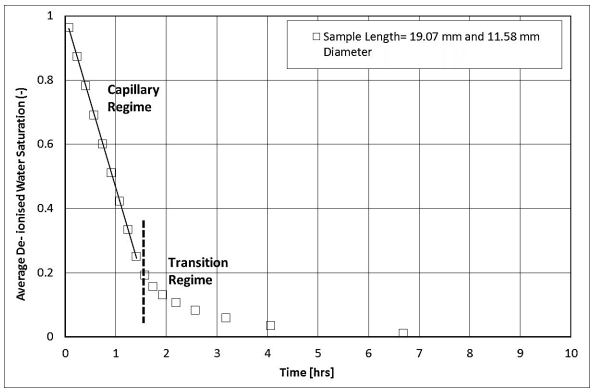
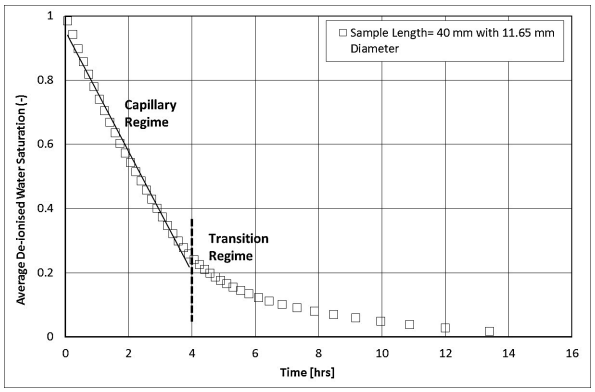


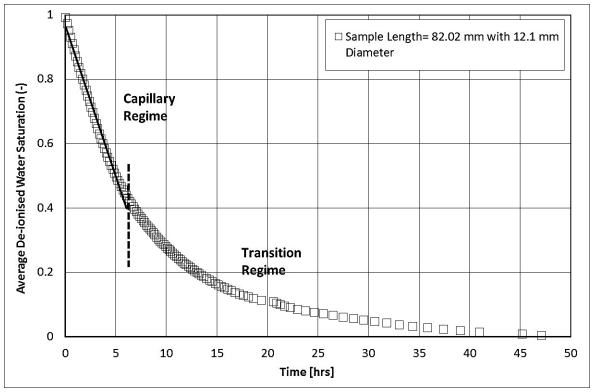
Figure 4-6 Zoom in average cumulative mass loss of De-ionised water for Bentheimer samples of different length at temperature 60°C, RH~0%



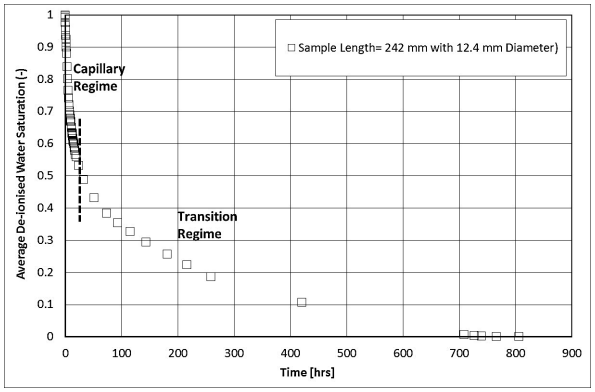
(a) 19.07mm sample length with 11.58mm diameter



(b) 40mm sample length with 11.65mm diameter



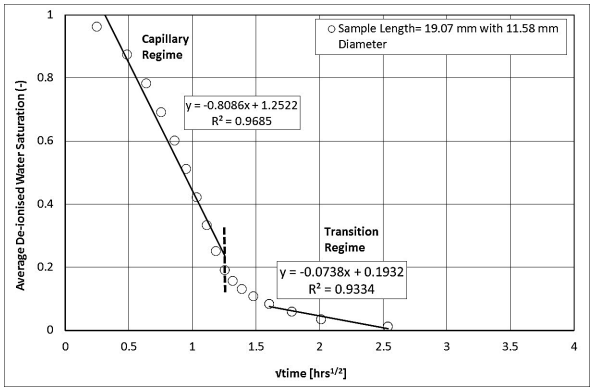
(c) 82.02mm sample length with 12.10mm diameter



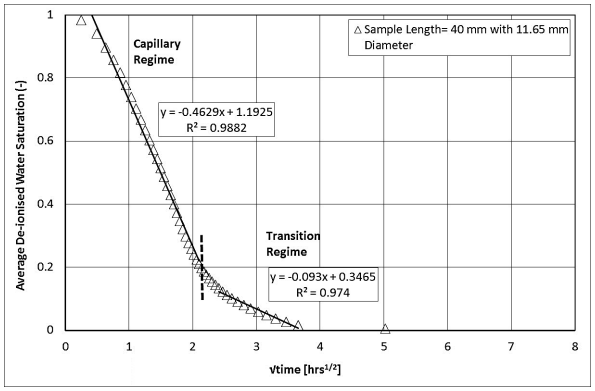
(d) 242mm sample length with 12.40mm diameter

Figure 4-7 Average saturation of de-ionised water for Bentheimer samples of different length at temperature 60°C, RH~0%

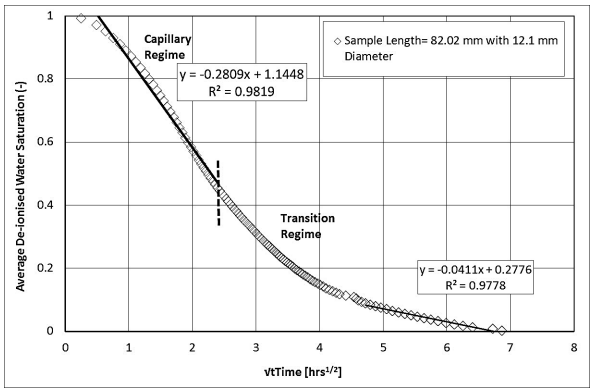
In Figure 4-8 (a, b, c, and d) shows the average evaporation plotted against the square root of time for different sample lengths 19.07, 40, 82.02 and 242mm, respectively. The dotted line shows the direct change in the dry-out regime from capillary drying regime to transition regime. From Figure 4-8 (a, b), the transition in the drying kinetics curve occurred at $t^{1/2}$=1.22hrs$^{1/2}$ and $t^{1/2}$=2.0hrs$^{1/2}$ for 19.07mm and 40mm sample lengths, respectively. However, by increasing the sample length, the liquid film detachment (CRP to FRP transition) occurred at $t^{1/2}$=2.4hrs$^{1/2}$ and $t^{1/2}$=5.0hrs$^{1/2}$ for 82.02mm and 242mm, respectively. This is a clear indication of the effect of the sample length on the drying kinetics curves as stated in the literature review by Lehmann et al., (2008) and others researchers.



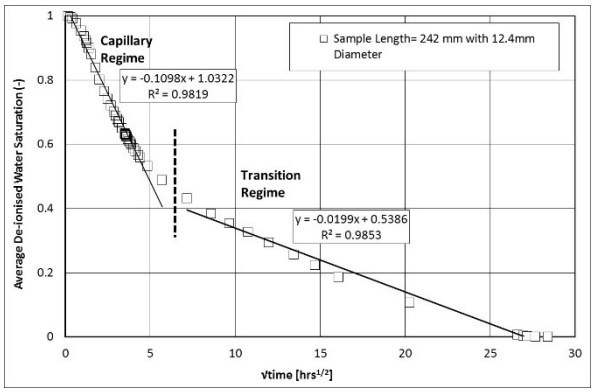
(a) 19.07mm sample length with 11.58mm diameter



(b) 40mm sample length with 11.65mm diameter



c) 82.02mm sample length with 12.10mm diameter



(d) 242mm sample length with 12.40mm diameter

Figure 4-8 Average saturation of de-ionised water for different Bentheimer porosities with square root of time (hrs) for different samples dimensions at temperature 60°C, RH~0%

4.1.2.3 Rock Types Effect on Pure De-ionised Water Evaporation

To study the effect of different types of rocks on de-ionised water dry-out and on the evaporation and liquid film detachment (CRP transition to FRP), a series of experiments for the drying rate evolution with time were performed using Bentheimer sandstone (porosity 22.19%) and Ketton carbonate (24.0%). The sample was 82.02mm in length and 12.10mm

diameter for the Bentheimer test. For Ketton carbonate the sample dimension was 80.11mm length and 11.56mm sample diameter; the air temperature was 60°C and RH ~ 0%. The Bentheimer mean pore size was 20 microns compared with Ketton which has micro porous grains and macroporosity around 20 microns.

Figures 4-9 shows the cumulative mass of water lost with time for Betheimer sandstone and Ketton carbonate. It can be seen form Figure 4-14 that for approximately same sample lengths, the cumulative mass loss for the Bentheimer sandstone was approximately 1.5 (g) at 10.0hrs compared with 1.0 (g) for Ketton carbonate at 3.90hrs. Thus, the time taken for the Bentheimer sandstone to completely dry-out was less than 60hrs, compared with 120hrs for Ketton carbonate, see Figure 4-16. This can be explained by the fact that the Bentheimer sandstone has a more continuous pose size distribution compared with Ketton which has microporosity (less than a microns) and macroporosity (20 microns). Once the Ketton macro pores emptied liquid transport would have been confined to the micro-pores, which have very low permeability, resulting in an earlier transition from the constant rate period than seen in Bentheimer as is shown in Figure 4-9.

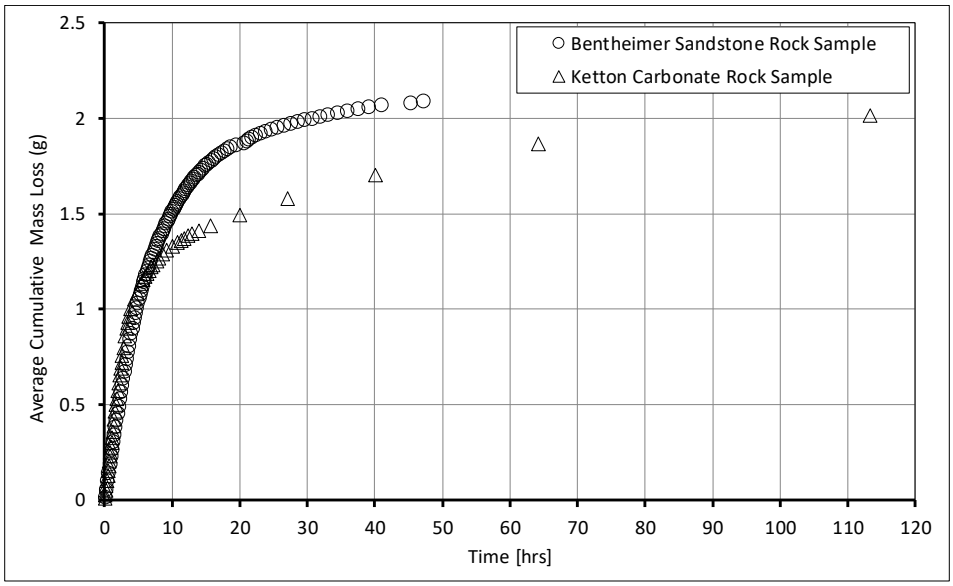
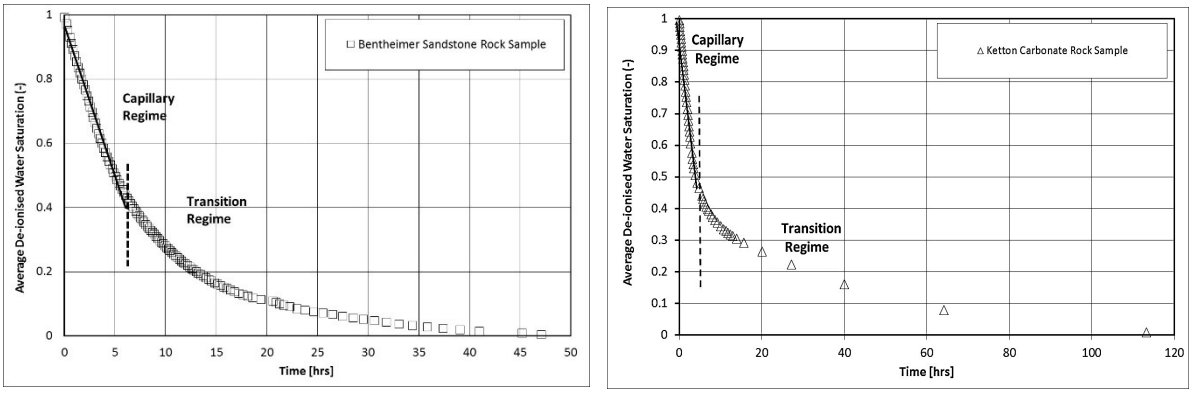


Figure 4-9 Cumulative mass loss of de-ionised water for Bentheimer sandstone and Ketton carbonate with time (hrs) for 80mm sample length at temperature 60°C and 12mm diameter, RH~0%

Figure 4-10 (a and b) shows the average evaporation for De-ionised water for Bentheimer sandstone and Ketton carbonate with time (hrs) at temperature 60°C and RH~0%. This figure shows that more than 60% evaporation occurred by 6.0hrs for Bentheimer sandstone compared with 43% evaporation for Ketton carbonate at approximately 3.0hrs. The observations in this study are aligned with previous works reported in the literature review by

other researchers such as (Scherer, 2004; Van Brakel, 1980). During evaporation from porous media saturated with water, large pores at the surface were invaded by air at the early stages of the process, while smaller pores remain water saturated due to capillarity effects.

The evaporative demand was continuously supplied by the capillary-induced liquid flow which transport the water towards the fine pores (Bentheimer sandstone case) at the surface during first stage (Scherer, 2004; Van Brakel, 1980). Also, during the stage-1, water vaporisation occurred mainly in the smaller pores filled with water at the surface and this mechanism continued if the downward resisting gravity and viscous forces were less than the upward capillary force (Lehmann et al., 2008; Or et al., 2013; Shokri et al., 2012).



(a) Bentheimer Sandston, RH~0% **(b) Ketton Carbonate, RH~0%**

Figure 4-10 Average saturation of De-ionised water for Bentheimer sandstone and Ketton carbonate with time (hrs) for 80mm sample length at temperature 60°C and 12mm diameter

Figure 4-11 (a and b) shows the evaporation flux for De-ionised water with square root time for Bentheimer and Ketton samples at temperature 60°C. The dotted line presents the change in the dry-out flow regime from capillary regime to transition regime.

From Figure 4-11, the liquid film detached from sample surface at 2.4hrs for Bentheimer sandstone compared with 1.7hrs for Ketton carbonate due to the continuity of capillarity flow cross connectivity for Bentheimer sandstone and this was due the reduction in the effective evaporation surface area. Based on Nachshon et al., (2011), the large pores at the surface dried first and then it started to feed the small pores and that happens in the heterogeneous rock porous sample.

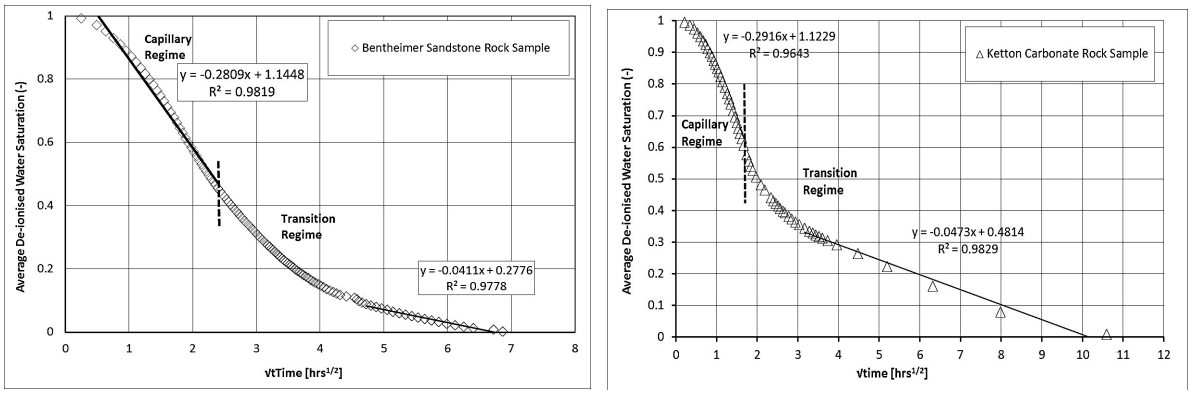


Figure 4-11 Average saturation for de-ionised water with square root of time for Bentheimer and Ketton samples for 80mm sample length at temperature 60°C, RH~0%

4.1.3 Dry-out during Evaporation of Brine Results and Discussions

4.1.3.1 Effect of Salt Concentration on Evaporation Process

In this section, the brine evaporation and the precipitation of salt in 40mm sample length and 12mm diameter. The oven flow air temperature was maintained at 60°C and at approximately 0% air relative humidity (RH). The brine (NaCl) concentrations were 3.0 Molal (moles of NaCl/kg of water) and 6.4 Molal. Initially, the core sample was flooded with 100 pore volumes of CO_2, followed by the introduction of 100 pore volume of brine.

The key objectives of the gravimetric tests were to identify the drying kinetic behaviour for the saturated sample with brine under different salt concentration and for different types of rocks including Bentheimer sandstone and Ketton carbonate, therefore, the evaporation rate, drying kinetics and precipitated salt were the main source of information in these tests. Also, µ-CT images were taken at the end of drying test to identify the salt distribution in the tested Bentheimer and Ketton samples.

As stated in the literature (Nachshon et al., 2011b; Nachshon et al., 2011a), the drying process is coupled with capillary convective flows that transport the liquid near evaporating surfaces. However, in the presence of salt, water evaporation from the fine pores at the surface results in a continuous increase of salt concentration in the evaporation areas at the surface. When salt concentration reaches the solubility limit, which is 6.4 Molal (moles of NaCl/kg of water) for NaCl at 60°C, precipitation takes place, however, the supersaturation effects on the salt nucleation in this tests was unknown. However, Desarnaud et al., (2014) stated based on experimental investigations on capillary tube that the nucleation happened at a very high

supersaturation S ~ 1.6 and was independent of the size, shape, and surface properties of the microcapillary.

Figure 4-12 illustrates the cumulative loss of de-ionised water and different brine solutions (3.0 Molal and 6.4 Molal) with time. The slope of the cumulative mass loss (g) versus time (hrs) indicates the evaporation rate.

Figure 4-12 shows the average cumulative mass (g) of liquid water removed by evaporation from the Bentheimer sandstone sample, which initially saturated with various NaCl solutions (3.0 Molal and 6.4 Molal). It can be deduced from Figure 4-12 that the liquid mass slope was nearly constant for the early stages of evaporation followed by a lower slope which corresponded to the transition to the next stage of evaporation.

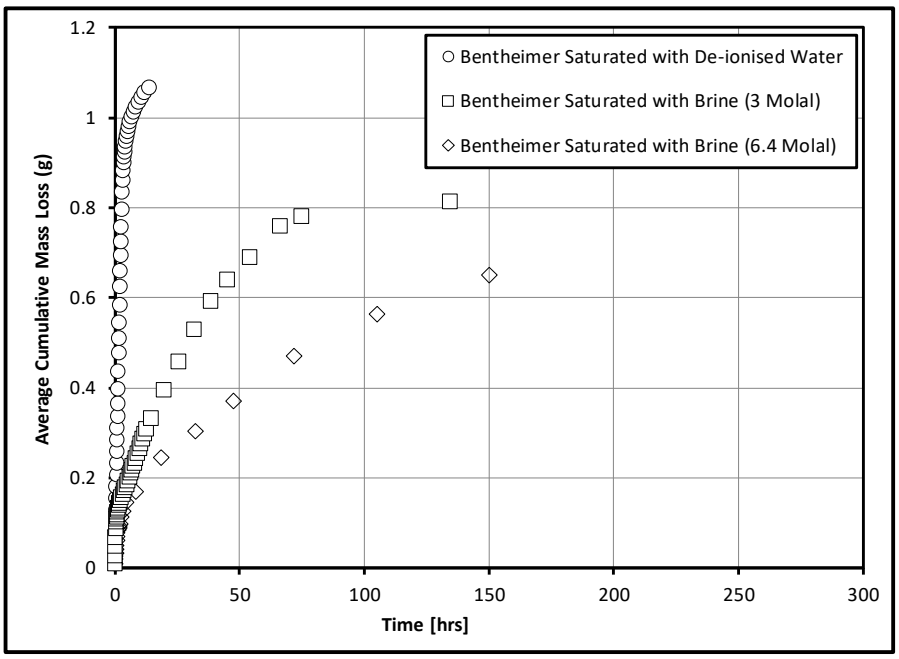


Figure 4-12 Average cumulative loss for Bentheimer for De-ionised water, Brine (3.0 Molal and 6.4 Molal) with time (hrs) for 40mm sample length at temperature 60°C and 12mm diameter, RH~0%

During the early stage evaporation of brine solution, the surface is hydraulically connected to the rest of the sample through wetting films, taking care of the transport of the salt ions to the surface of the sample. The continuous movement of the solute towards the point of evaporation at the surface causes an increase in the salt concentration at the surface until it reaches the solubility limit, resulting in the precipitation of salt at the sample surface. The first crystallisation then starts at the surface since the water evaporates there, and the formation of the first crystal acts as a seed for further salt crystallisation, leading eventually to the

efflorescence growth outwards. In parallel, the precipitation of multiple small crystals also induces a roughness of the surface that leads by capillary force to an enhanced spreading of the fluid which results in a creeping motion of the salt (Bico et al., 2002; Shahidzadeh-Bonn et al., 2008).

According to Norouzi Rad et al. (2013), the transition from the first stage of evaporation (capillary-driven drying regime) to the second stage (diffusion-driven drying regime) initiates when the precipitation of salts crust occurs and this is evidenced by a sharp decrease in the water salt evaporation rate. Prior to the transition, most the evaporation areas or spots serve as the precipitation spots, resulting in an increase in the relatively constant precipitation rate.

Figure 4-13 shows the transition from the capillary-driven drying regime to diffusion-driven drying regime for brine solutions with 3.0 Molal and 6.4 Molal concentrations. The solid symbols in Figure 4-13 represents the transition between the two drying regimes. For brine concentration of 6.4 Molal, the transition between two drying regimes occurred at the very early stage of evaporation (0.1hr) compared with 0.2hr for 3.0 Molal.

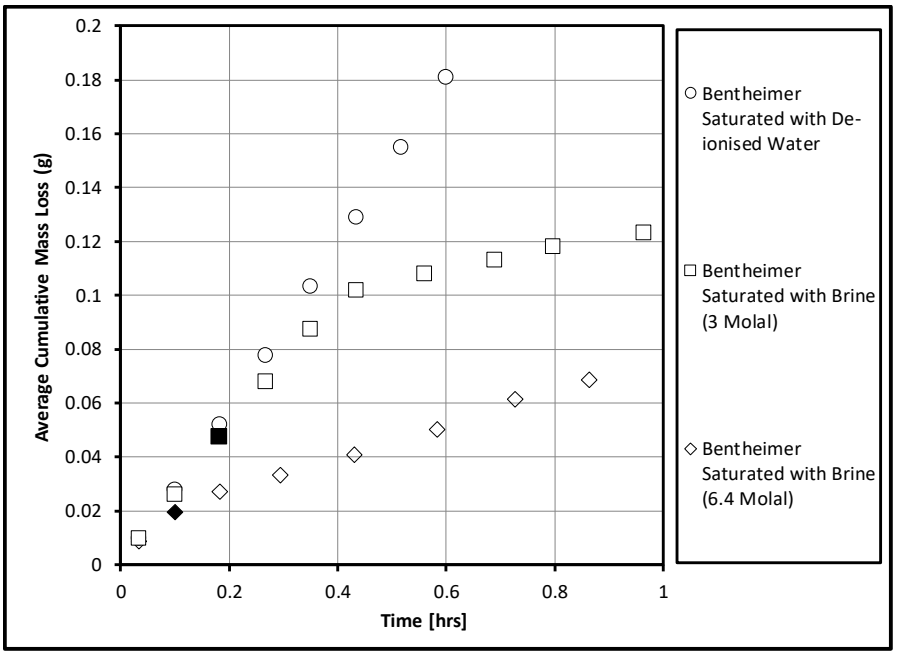
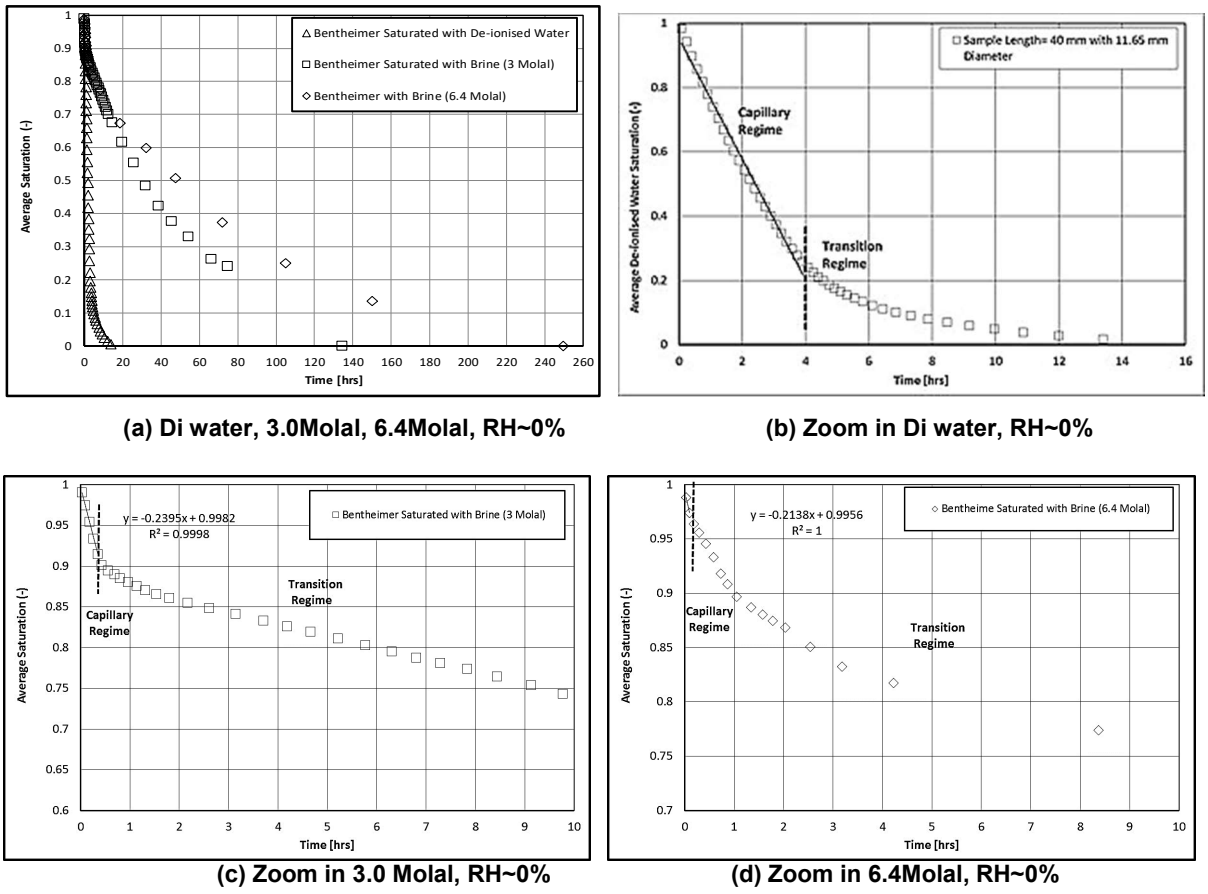


Figure 4-13 Zoom in Bentheimer cumulative loss for De-ionised water, Brine (3.0 Molal and 6.4 Molal) with time (hrs) for 40mm sample length at temperature 60°C and 12mm diameter, RH~0%

Figure 4-14 (a) shows the average saturation with time for the De-ionised water and brine solutions with 3.0 Molal and 6.4 Molal. Figure 4-14 (b), shows that the average saturation for de-ionised water. Figure 4-14 (c), shows that the average saturation for 3.0 Molal followed the

same de-ionised water saturation curve during early stage of evaporation (linear in time), however, at 0.4hr, the transition to square root behaviour occurred. For 6.4Molal, the transition occurred much faster at 0.1hr, see Figure 4-14 (c). Further the average saturation curve for 6.4 Molal deviated from the 3.0 Molal at 20hrs and this was due to the precipitated salt increase at the surface, see Figure 4-14 (a).



(a) Di water, 3.0Molal, 6.4Molal, RH~0%

(b) Zoom in Di water, RH~0%

(c) Zoom in 3.0 Molal, RH~0%

(d) Zoom in 6.4Molal, RH~0%

Figure 4-14 Average saturation for De-ionised water, 3.0 Molal and 6.4 Molal with time [hrs] for 40mm sample length at temperature 60°C and 12mm diameter

Figure 4-15 shows the evaporation flux (kg m^{-2} hr^{-1}) versus the average saturation for de-ionised water, 3.0 Molal and 6.4 Molal salt concentrations. The purpose of Figure 4-15 was to demonstrate the effect of precipitated salt on the evaporation rate.

From Figure 4-15, it shows that the evaporation flux for de-ionised water, 3.0 Molal and 6.4 Molal was same during the early stage of evaporation and at average saturation of approximately two. However, the evaporation flux rapidly dropped for highest salt concentration of 6.4 Molal whereas for 3.0 Molal, the evaporation flux maintained like water case until S_w=0.9 average saturation. This is expected since the water evaporation activity

was reduced in the presence of dissolved salt: the vapour pressure for brine solution at 6.4 Molal was 16000 Pa which was below that for pure water 19950 Pa at 60°C.

The mean values of the initial evaporation flux (kg m^{-2} hr^{-1}) for the initial drying (CRP) of de-ionised water, 3.0 Molal and 6.4 Molal brine are plotted against vapour pressure in Figure 4-16. It can be observed from the dotted line that evaporation rate was mainly vapour pressure dependant prior to salt precipitation at surface of the sample.

The evaporation flux was approximately constant for both salt concentrations, 3.0 Molal and 6.4 Molal, but with slightly lower values for 6.4 Molal and this was expected because of salinity on vapour pressure as shown in below Figure 4-16.

At 6.4 Molal, the salt precipitation starts very early at an average saturation, S_w = 0.99 and the NaCl reached critical salt concentration resulting in efflorescence salt growth. The evaporation flux decreased sharply with time as shown in Figure 4-15, however, this did not necessarily indicate that the liquid films disconnected from the outer surface. During the brine evaporation, salt ion transport was initially dominated by advection of the liquid to the surface of the sample.

This can be shown by calculating a Pelect number based on the volume of liquid required to provide the evaporative flux, a length scale which was taken to be the mean pore size of the Bentheimer (20 μm) pore and a diffusion coefficient for sodium ions of 1.10^{-9} m^2s^{-1}.

This Peclet number was initially 212 and at the end stage of drying out, the Peclet number was approximately 1. This shows that during most of the drying process diffusion would not be able to transport the dissolved salt ions away from the site of evaporation and the brine would only become locally supersaturated. The site of the salt deposition, therefore, indicates where evaporation was occurring.

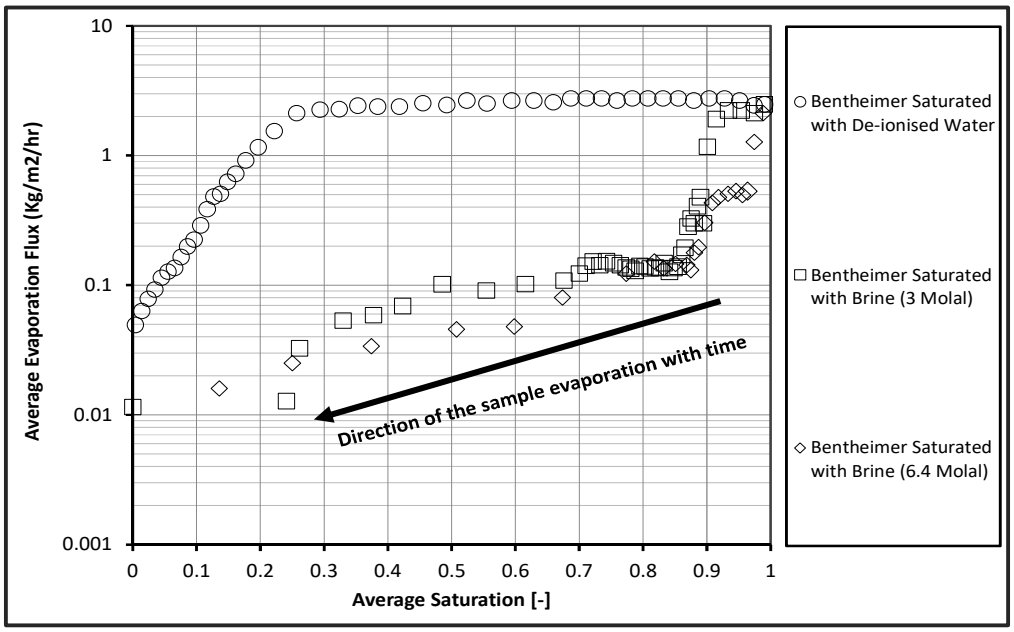


Figure 4-15 Evaporation flux for de-ionised water, Brine (3 Molal and 6.4 Molal) versus average saturation for 40mm sample length at temperature 60°C and 12mm diameter, RH~0%

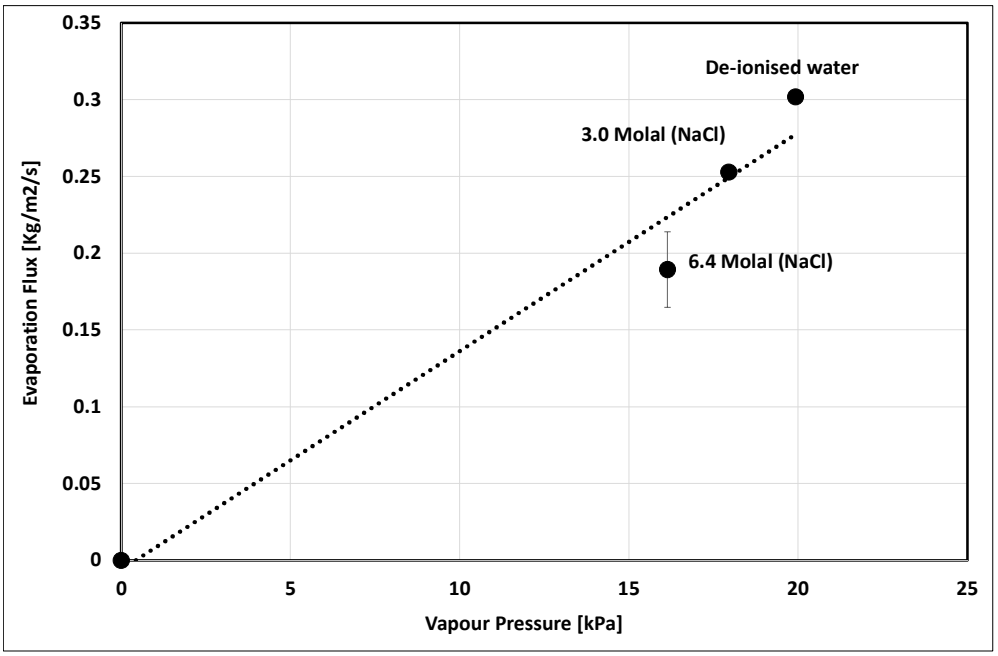


Figure 4-16 Evaporation flux for de-ionised water, Brine (3 Molal and 6.4 Molal) versus vapour pressure for 40mm sample length at temperature 60°C and 12mm diameter, RH~0%

The changes in the rates of the evaporation flux during the salt precipitation would be consistent with a transition to a diffusion dominated regime for the de-ionised water case, however, the saturations and the drying flux would also easily allow the capillary force to maintain the transport of the liquid to the surface in the original rock structure. Further, the salt

deposited is also water wet so the different drying characteristics appear to originate in the structural evolution of the precipitated salt with time during the evaporation process.

The modified structure of precipitated salt has been addressed by several researchers. For example, Norouzi Rad and Shokri (2012) stated that during stage 1 (capillary driven drying regime), the precipitated porous salt may draw the liquid to the surface where evaporation occurs, maintaining the hydraulic connections between the receding front and the evaporation surface, despite the existence of the precipitated salt at the surface.

Even at later stages of evaporation, the precipitated salt was porous. However, as the evaporation proceeds, further salt precipitation eventually blocks the pores of the efflorescence, resulting in the interruption of capillary flow to the surface. Moreover, the images taken by Rad and Shokri, (2013) confirmed the porous nature of the precipitated salt, its evolution at the evaporation surface, and its role in maintaining a relatively constant evaporation rate even when the surface was covered by the precipitated salt.

The development of the precipitated porous salt structure was investigated in this work and will be addressed later in this chapter in the section concerning µ-CT imaging of evaporation and salt precipitation. However, some µ-CT images were also obtained after completion of gravimetric tests and in those we observed salt deposited outside the sample. Figure 4-17 shows the µ-CT image of Bentheimer sandstone at 2 µm voxel size in 40 mm length with 12mm diameter. The sample was saturated with 6.4 Molal NaCl and the image was taken at the end of complete dry out in a gravimetric test. Salt deposits can be seen growing away from the rock surface with only a small amount of salt in the first few pores adjacent to the surface.

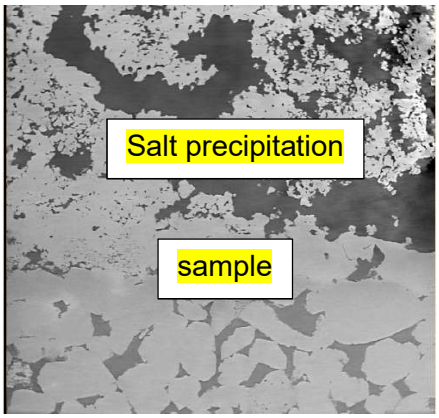
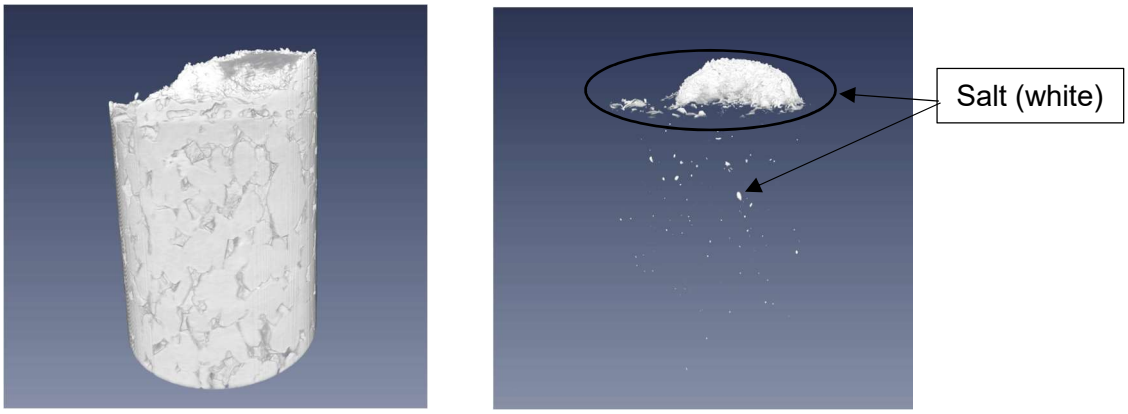


Figure 4-17- µ-CT images for Bentheimer for Brine (6.4 Molal) at the end of the Dry-out Test (250hrs) for 40mm sample length at air temperature 60°C and 12mm diameter

To investigate the precipitated salt distribution during the evaporation of brine, a µ-CT image of Bentheimer sandstone at 2 µm voxel size was obtained at the end of the dry-out process of the 40mm sample length and 12mm diameter and that is for 6.4 Molal salt concentration. Figure 4-18 (a) shows a 3D view of µ-CT image at 250hrs. Figure 4-18 (a) demonstrated that salt was precipitated at the surface of sample surface. The µ-CT image was further processed by removing the grain and only focused on salt distribution. The aim of the image process was to assess whether salt was progressed towards the interior of the Bentheimer sandstone core. Figure 4-18 (b) shows that there was some salt crystallisation within the sample matrix (white is salt).

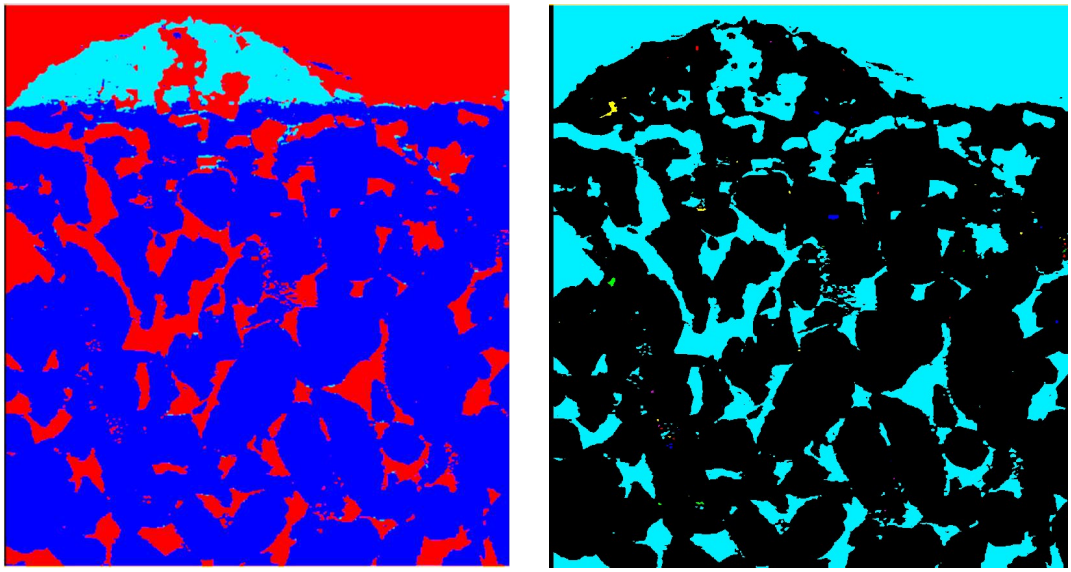


(a) µ-CT image for sample (6.4 Molal) **(b) Salt precipitation distribution (6.4 Molal)**

Figure 4-18 µ-CT raw images (at 2 µm voxel size) for precipitated salt for Bentheimer for 6.4 Molal brine concentration for 40mm sample length at temperature 60°C and 12mm diameter, RH~0% (white is salt)

Figure 4-19 (a, b) shows the µ-CT segmented images of Bentheimer sandstone at 2 µm voxel size and that for 6.4 Molal brine concentration for 40mm sample length at temperature 60°C and 12mm diameter. In Figure 4-19 (a), it is shown the precipitated salt at sample surface (in light blue), and grain in dark blue and pore phase in red. Figure 4-19 (a) demonstrates that small amount of salt was precipitated near the surface and within the core of sample.

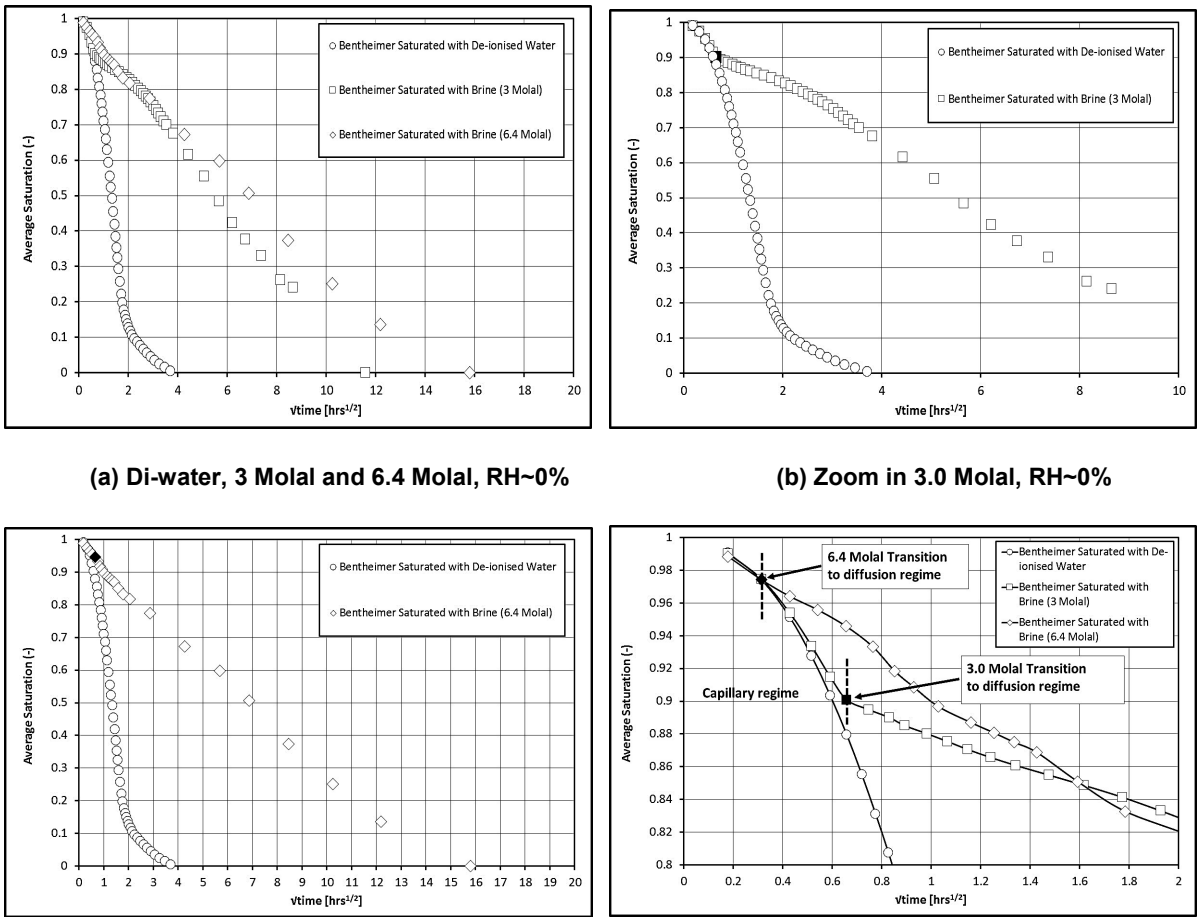
Figure 4-19 (b) shows that at the end of dry-out process, the hydraulic continuity through the sample between the liquid film and sample surface where salt precipitation occurred was maintained. In Figure 4-19 (b) and to assess the hydraulic connectivity (light blue) both grain and salt were grouped in one colour (black). The orange small spot shows the disconnected pores. Please note that further detailed assessment for hydraulic continuity during evaporation and salt precipitation was presented later in the following µ-CT (dynamic) dry-out and salt precipitation section



(a) Salt precipitation at surface of the sample (b) Hydraulic continuity through sample

Figure 4-19 µ-CT segmented images at 2 µm voxel size for Bentheimer for precipitated salt for 6.4 Molal brine concentration for 40mm sample length at temperature 60°C and 12mm diameter, RH~0%

Figure 4-20 shows the average saturation plotted against the square root of time for Bentheimer sandstone (40mm sample length with 12mm diameter) saturated with de-ionised water and two brine concentrations (3.0 Molal and 6.4 Molal NaCl) at an air temperature of 60°C and at RH~0%. The impact of different salt concentration is very clear from Figure 4-20 (a). For the 3.0 Molal brine concentration case, 10% of total liquid content was dried out at a time of approximately 0.7 $hr^{1/2}$ when a transition in drying regime occurred (Figure 4-20 (b)). At the higher initial brine concentration of 6.4 Molal, 3% of total liquid content was dried out at a time of 0.5 $hr^{1/2}$ when a transition in drying regime occurred (Figure 4-20 (c)). The transition from the constant drying rate of the capillary drying regime to square root behaviour for 3.0 Molal and 6.4 Molal is shown clearly in the zoom in Figure 4-20 (d).



(a) Di-water, 3 Molal and 6.4 Molal, RH~0%

(b) Zoom in 3.0 Molal, RH~0%

(c) Zoom in 6.4 Molal, RH~0%

(d) Zoom in Di-water, 3 Molal and 6.4 Molal, RH~0%

Figure 4-20 Average saturation for de-ionised water, Brine (3.0 Molal and 6.4 Molal) versus square root of time for 40mm sample length at temperature 60°C and 12mm diameter

4.1.3.2 Effect of Rock Type on Salt Precipitation during Dry-out

To study the effect of different types of rocks on salt precipitation during dry-out, an additional series of evaporations tests were performed using Ketton carbonate with 24.0% porosities, for comparison to the Bentheimer results reported above. The dimensions of the samples were 40mm in length and 12 mm diameter and NaCl solutions of 3.0 Molal and 6.4 Molal were used as before. Air temperature was 60°C and RH ~ 0%.

Figure 4-21 shows the cumulative mass loss with time for de-ionised water and 3.0 Molal and 6.4 Molal brine concentrations. In Figure 4-21, the slope of the cumulative mass loss versus time gives the evaporation rate. Similar to the Bentheimer sandstone results reported above in this chapter, during the first stage of evaporation for Ketton sample, the slope of the cumulative mass loss curve was nearly constant initially followed by a lower slope which corresponded to the transition to the next stage of evaporation. From Figure 4-21, the

transition between the two drying regimes occurred at the very early stage of evaporation time of 0.57hr compared with 0.62hr for the 3.0 Molal salt concentration.

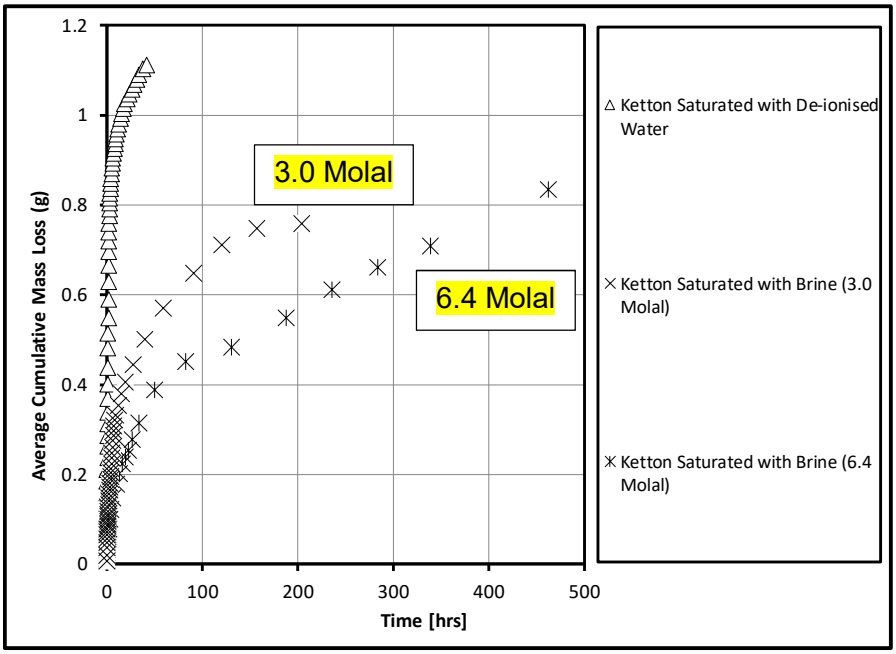


Figure 4-21 Average cumulative loss for Ketton for De-ionised water, Brine (3.0 Molal and 6.4 Molal) with time (hrs) for 40mm sample length at temperature 60°C and 12mm diameter, RH~0%

Figure 4-22 shows the average saturation with time for the De-ionised water and NaCl solutions with 3.0 Molal and 6.4 Molal. For 3.0 Molal, the reduction in average saturation was linear in time during the early stage of evaporation, which was close to De-ionised water case, but at 0.62hr and 10% dried-out sample. At average saturation of S_w=0.9, the transition to square root behaviour occurred. However, for 6.4Molal, the transition occurred at 0.57hr and S_w=0.95 average saturation as shown in the zoomed in Figure 4-23.

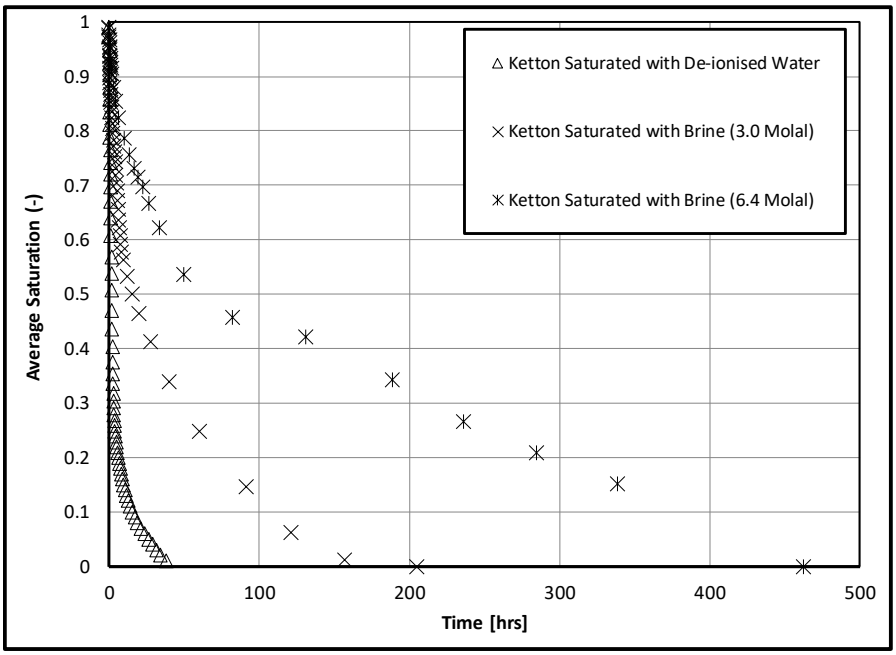


Figure 4-22 Average saturation for Ketton for De-ionised water, Brine (3.0 Molal and 6.4 Molal) with time (hrs) for 40mm sample length at temperature 60°C and 12mm diameter, RH~0%

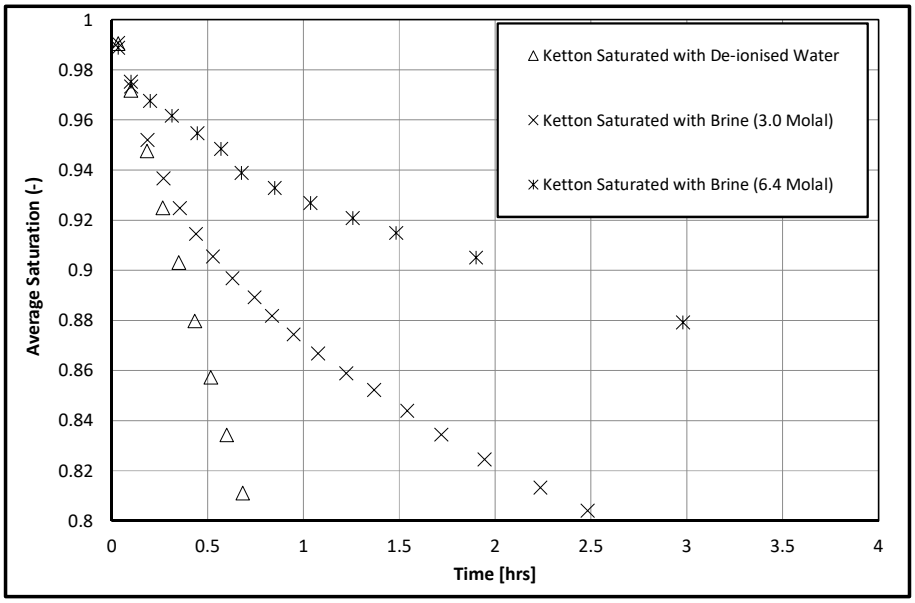


Figure 4-23 Zoom in average saturation for Ketton for De-ionised water, Brine (3.0 Molal and 6.4 Molal) with time (hrs) for 40mm sample length at temperature 60°C and 12mm diameter, RH~0%

Figure 4-24 shows the average saturation plotted against the square root of time for Ketton carbonate for de-ionised water and brine (3.0 Molal and 6.4 Molal). The square root beahviour regime due to the presence of the salt is shown in Figure 4-24. This was similar to Bentheimer sandstone sample case reported previously however, due to the dual pore structures of the Ketton carbonate, the evaporation period was longer than the period taken for the Bentheimer case to complete the sample dry-out and as shown in 4-25.

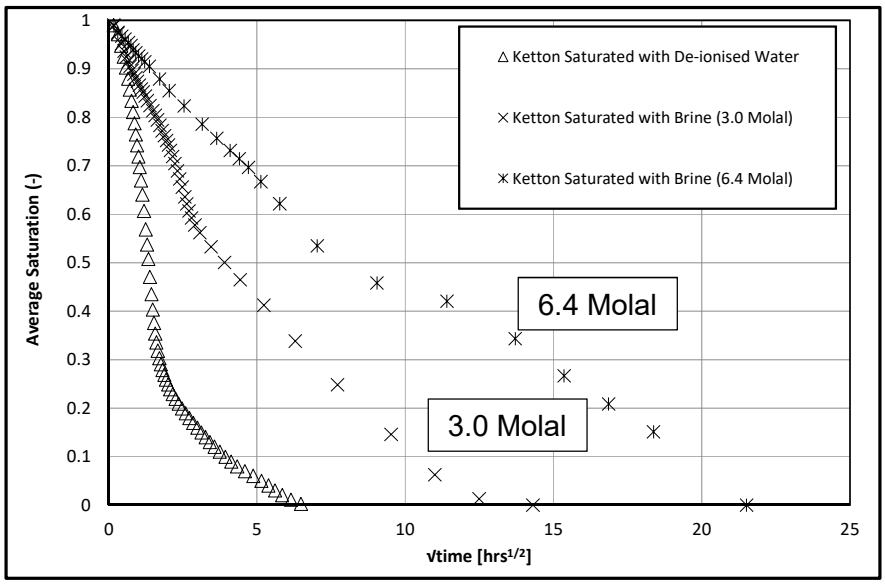


Figure 4-24 Average saturation for Ketton for de-ionised water, Brine (3.0 Molal and 6.4 Molal) with square root of time (hrs) for 40mm sample length at temperature 60°C and 12mm diameter, RH~0%

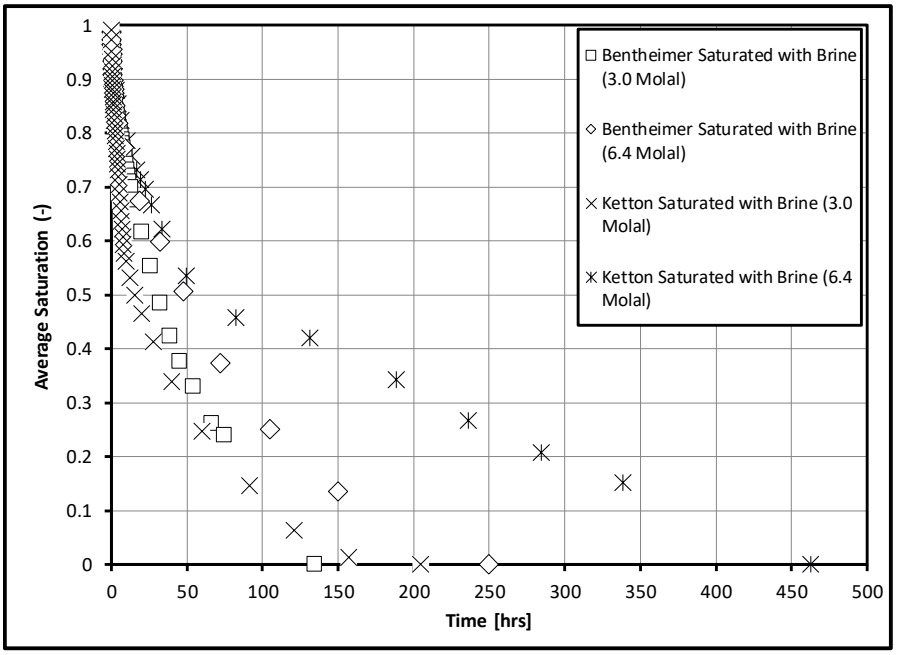
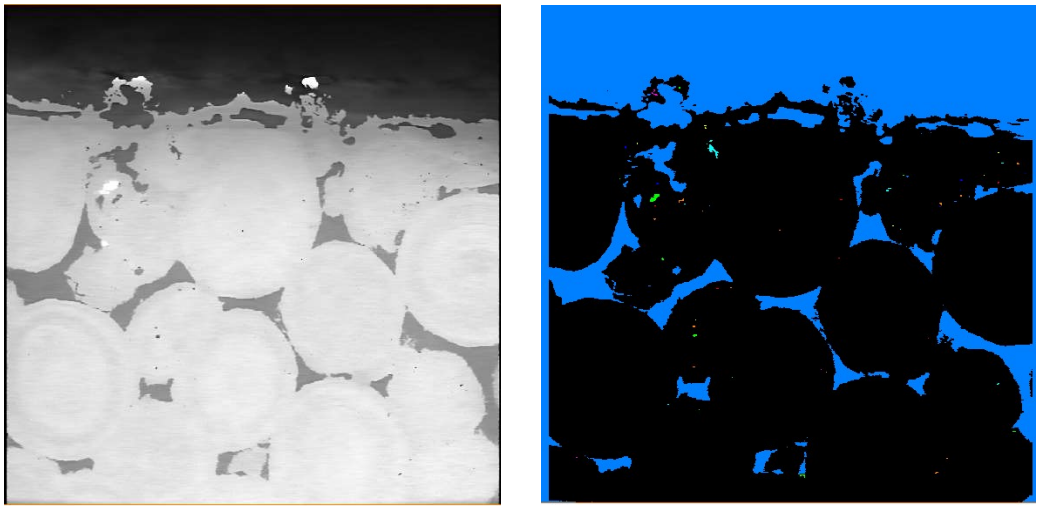


Figure 4-25 Average saturation for Ketton and Bentheimer for Brine (3.0 Molal and 6.4 Molal) with time (hrs) for 40mm sample length at temperature 60°C and 12mm diameter, RH~0%

Figure 4-26 (a) shows the raw µ-CT image for Ketton carbonate at 2.5 µm voxel size was obtained at the end of the dry-out process of the 40mm sample length and 12mm diameter and that for 6.4 Molal salt concentration. This figure demonstrated that salt was precipitated at the surface of the sample at 460hrs. Figure 4-26 (b) shows the hydraulic connectivity (light blue) both grain and salt were grouped in one colour (black) at the end of dry-out. The different colour spots show the disconnected pores.



(a) Salt precipitation at surface of the sample (b) Hydraulic continuity through sample

Figure 4-26 µ-CT segmented images at 2 µm voxel size for Ketton carbonate for precipitated salt for 6.4 Molal brine concentration for 40mm sample length at temperature 60°C and 12mm diameter, RH~0%

From the brine gravimetric tests for 3.0 Molal and 6.4 Molal brines, the following can be concluded;

- During the very early stage of evaporation, the drying curves for de-ionised water and NaCl solutions of 3.0 Molal and 6.4 Molal were similar, therefore it was observed that the present of salt has only a small impact on initial drying rate through vapour pressure reduction.

- Hydraulic connectivity was the main transport pathway for the salt ions from the core of the sample to the surface of the sample.

- For both 3.0 and 6.4 Molal NaCl solution, the precipitated salt was mostly on the surface of the sample.

- During the brine evaporation, salt ion was advective to the surface of the sample and with Pelect number values of initial 212, however, at the end stage of drying out, the Peclet number was 1.05.

- The precipitation of salt occurred at much earlier time during the first stage of the evaporation for 6.4 Molal NaCl solution as expected due to it being nearer to the solubility limit. However, the effect of supersaturation on the salt nucleation in this work was unknown. However, Desarnaud et al., (2014) stated based on experimental investigations on capillary tube that the nucleation happened at a very high supersaturation ~1.6 and was independent of the size, shape, and surface properties of the microcapillary.

- The effect of the precipitated salt on the surface of the sample was to strongly reduce the drying rate.

- The capillary drying regime was initially linear in time for a short period, followed by approximately square root behaviour for the second drying regime. Salt precipitation continued on the outwards of the surface of the sample even during the square root drying regime. This indicated that capillary effect was still present, but this is to be confirmed in the following μ-CT imaging analysis in the following section.

- The μ-CT images obtained at the end of the dry-out test showed that salt was mainly precipitated at the surface of the sample. However, minor salt precipitation was observed in the interior of the sample.

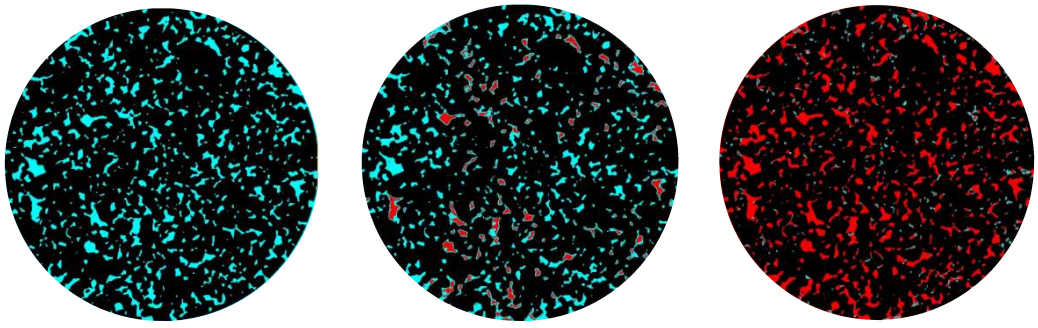
- The structural image of the precipitated salt demonstrated that the salt crust formed at the surface of the sample had a low porosity, but connectivity was maintained through the salt pores to the outside.

4.2 In situ μ-CT Images Analysis for Dry-out and Salt Precipitation

In this section a set of experiments are described where the drying was carried out inside the μ-CT scanner allowing the development of the salt deposit to be followed during the process. The water or brine saturation in the rock pore space was also measured at the pore scale during drying. The μ-CT images were used to verify the dry-out results obtained from the gravimetric tests and which were presented in above section in this chapter and to provide additional evidence for the mechanism of salt transport and deposition. The in situ μ-CT experiments were carried out for Bentheimer, 40mm sample length with 12mm diameter using De-ionised water and a brine solution with 6.4 Molal concentration and a temperature of 60°C and RH above the core approaching 0%.

4.2.1 µ-CT Image Analysis for De-ionised Water Dry-out at 6 µm voxel size

Figure 4-27 shows the same slice (at the sample surface) through the 6 µm voxel size µ-CT Images at three different times during the dry-out for De-ionised water for at 60°C air temperature and RH~0%. In Figure 4-27, the black, blue and red colours represent grains, de-ionised water and air/vapour filled pores, respectively. It can be seen from Figure 4-27 that water saturation decreased with time and sample was mostly dried-out at 8.0hrs, and the remained residual water could be due to the end effect caused by the short sample. Also, it can be seen at 4.0hrs that large pores dried first whereas small pores remained fully saturated and this time coincided with the end of linear regime. This is aligned with the works presented in the literature review by different researchers. Shokri, (2014) stated that during the early stage of evaporation, air preferentially invades large pores at the surface while finer pores remain saturated and connected to the wet zone at bottom via capillary-induced liquid flow acting as evaporating spots



a) time = 0 hr (b) time = 4 hrs (c) time = 8 hrs

Figure 4-27 Dynamic 6 µm voxel size Image with time for Bentheimer for De-ionised water in 40mm sample length with 12mm diameter at 60°C air temperature and RH~0% near the surface

Figure 4-28 (a, b) shows the de-ionised water saturation versus sample depth (up to the 3.5mm maximum depth visible in the images) from the sample surface with time. The segmented images were processed by slicing the 3D data parallel to the exposed sample face and then calculating the de-ionised water saturation of each slice sequentially away from the exposed face.

Figure 4-28 (a) shows the changes in the de-ionised water saturation profile with time [hrs]. From this figure, it is obvious that the saturation decreased with time. Figure 4-28 (b) shows the same data on a log scale. The saturation remained almost constant with depth, indicating that the dominant drying regime was capillary-driven regime (Figure 4-28 (a)). The saturation of de-ionised water estimated from the images was aligned with the reported gravimetric test

results presented above and the comparison is shown in Figure 4-29. However, a small discrepancy at later times the CT images gave a lower saturation than the gravimetric. This could be due to a slightly higher saturation deeper in the core outside the image used for the analysis which only shows ~ 1/3 of the full length of the core.

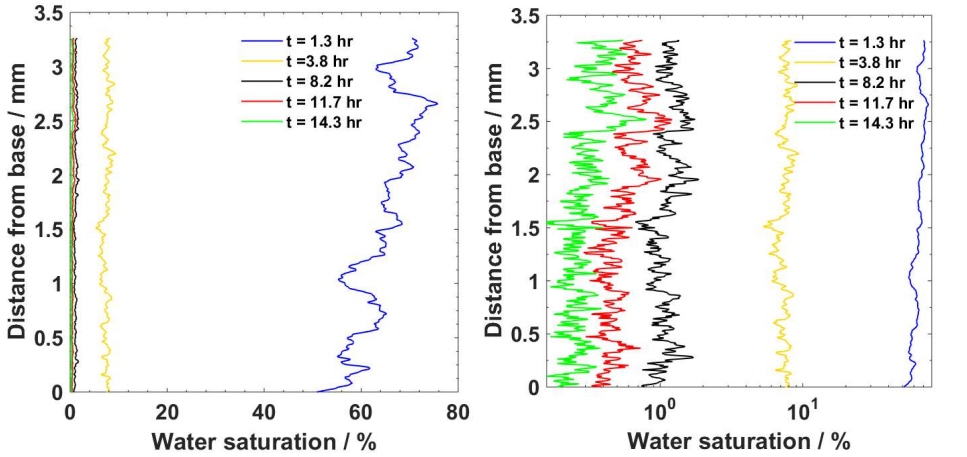


Figure 4-28 Saturation profile versus sample distance from the surface with time [hrs] using μ-CT dynamic images for De-ionised water for Bentheimer in 40mm sample length with 12mm diameter at 60°C air temperature and RH~0%

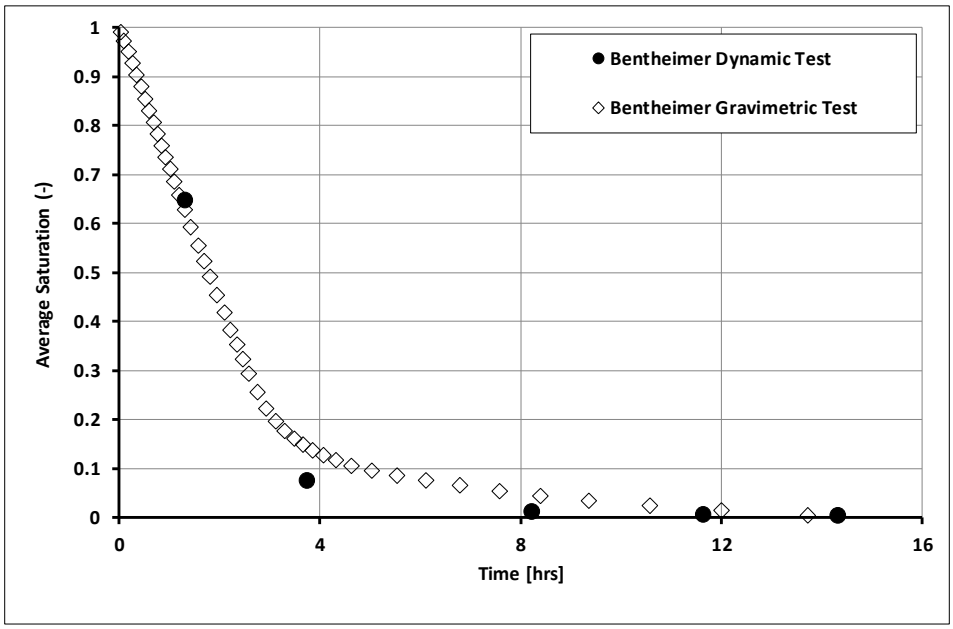


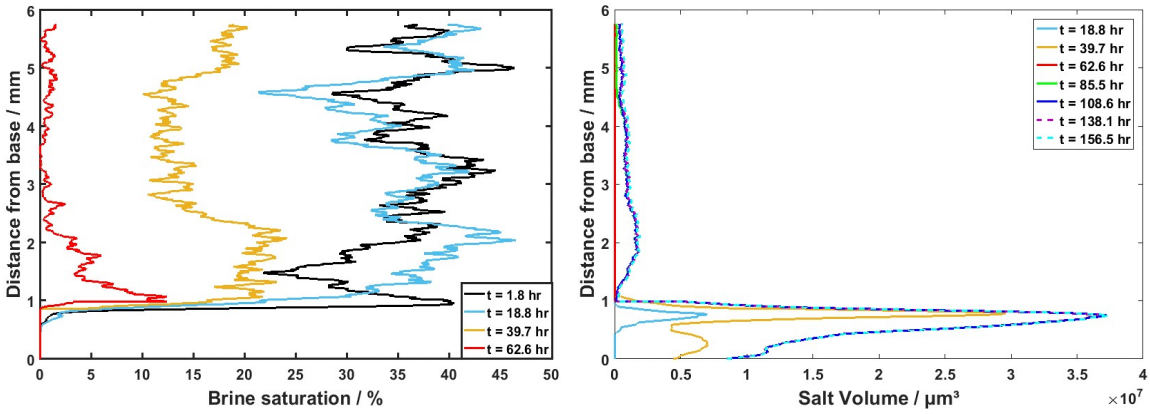
Figure 4-29 Average saturation comparison between μ-CT images and gravimetric test for Bentheimer for De-ionised water with time [hrs] in 40mm sample length with 12mm diameter at 60°C air temperature and RH~0%

4.2.2 µ-CT Image Analysis for Brine with 6.4 Molal at 6 µm voxel size

Figure 4-30 (a, b) shows µ-CT dynamic imaging analysis at 6 µm voxel size for the average saturation and precipitated salt volume versus sample depth at different times for the Bentheimer. The Bentheimer sandstone was initially saturated with NaCl of 6.4 Molal. The µ-CT dynamic images for brine saturation were captured at first four scanning steps (1.8hrs, 18.8hrs, 39.7hrs and 62.6hrs). From, Figure 4-30, it can be observed that brine saturation decreased with time. From Figure 4-30 (b), between 18 hrs and 62hrs, the salt precipitate continued to grow at the surface of the sample.

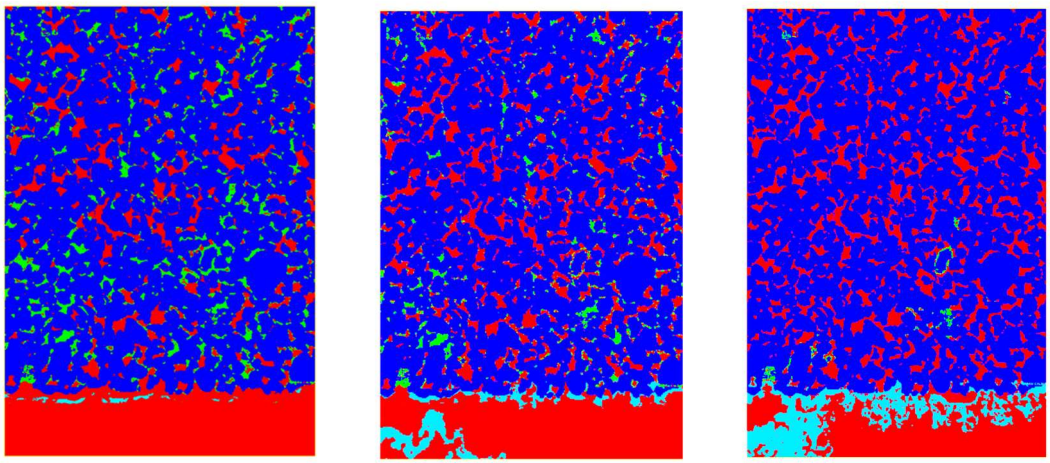
The reported average brine saturations were approximately 30% at 18hrs, 20% at 39.7hrs and 10% at 62hrs at surface of the sample, however, the average brine saturation deeper in the sample matrix at 62hrs was less than 10%.

Figure 4-31 shows the µ-CT images for the 6.4 Molal NaCl dry-out between 18 hrs and 62hrs. From Figure 4-31, it can be observed that salt continuously deposited at the surface of the sample as the water content decreased and the total volume occupied by precipitated salt in each slice.



a) brine saturation **(b) precipitated salt volume**

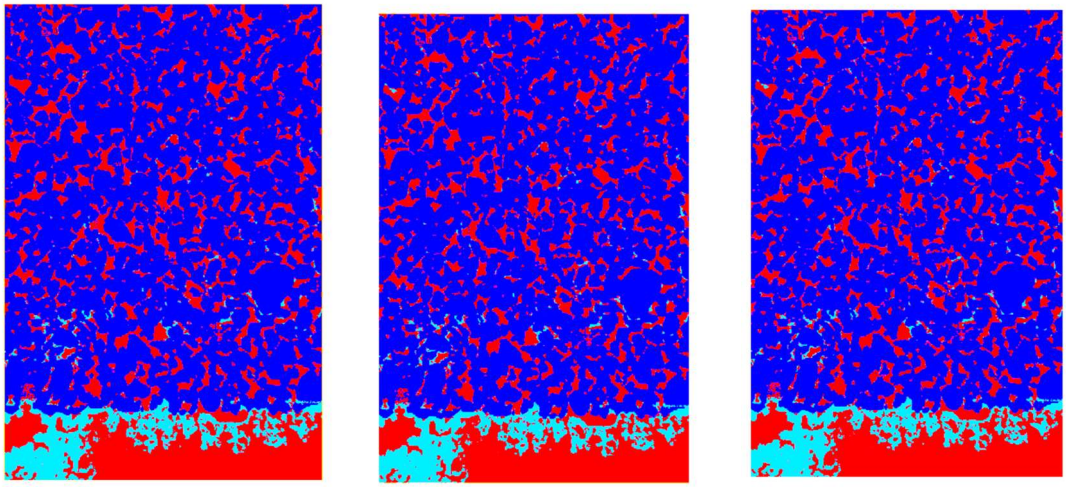
Figure 4-30 Brine (6.4 Molal) saturation and salt precipitation volume versus distance from exposed face with time using µ-CT dynamic images at 6 µm voxel size for Bentheimer in 40mm sample length with 12mm diameter at 60°C air temperature and RH~0%



time=18.8hrs time=39.7hrs time=62.6 hrs

Figure 4-31 Precipitated salt of 6.4 Molal NaCl solution at different time steps using µ-CT dynamic images at 6 µm voxel size for Bentheimer at 60°C air temperature and RH~0%. (Dark blue: grains, Red: pore phase, light blue: salt and green: brine solution)

At 85.5hrs scan brine was not captured as shown in Figure 4-32. Also, for the same figure, no further salt precipitation was observed at the surface of the sample. However, at later times salt precipitation progressed with time towards the interior of the sample core with small amount of salt (less than 5% of the total precipitated salt). This can be explained by the complete detachment between the liquid film and the sample surface. However, due to the µ-CT image resolution of 6 µm, the liquid films which must have transported brine to the sites of evaporation cannot be identified.



time=85.5 hrs time=108.6 hrs time=138.1 hrs

Figure 4-32 Precipitated salt of 6.4 Molal NaCl solution at different time steps using µ-CT dynamic images at 6 µm voxel size for Bentheimer at 60°C air temperature and RH~0%. (Dark blue: grains, Red: pore phase, light blue: salt and green: brine solution)

Figure 4-33 shows the μ-CT image at 6 μm voxel size of the precipitated salt distribution at cross sectional area of the face of the sample surface exposed to the drying region. In this figure, the dark blue, light blue, red, green colours represent the grains, salt, pore phase and brine solution, respectively. From Figure 4-33, the salt precipitation (light blue) started at 18.8hrs at the surface of the sample. The precipitated salt increased with time as shown in Figure 4-33 at 85.5hrs. The increase in the precipitated salt resulted in a change of the pore structure close to the surface of the sample, consequently resulting in a reduction the brine drying-rate.

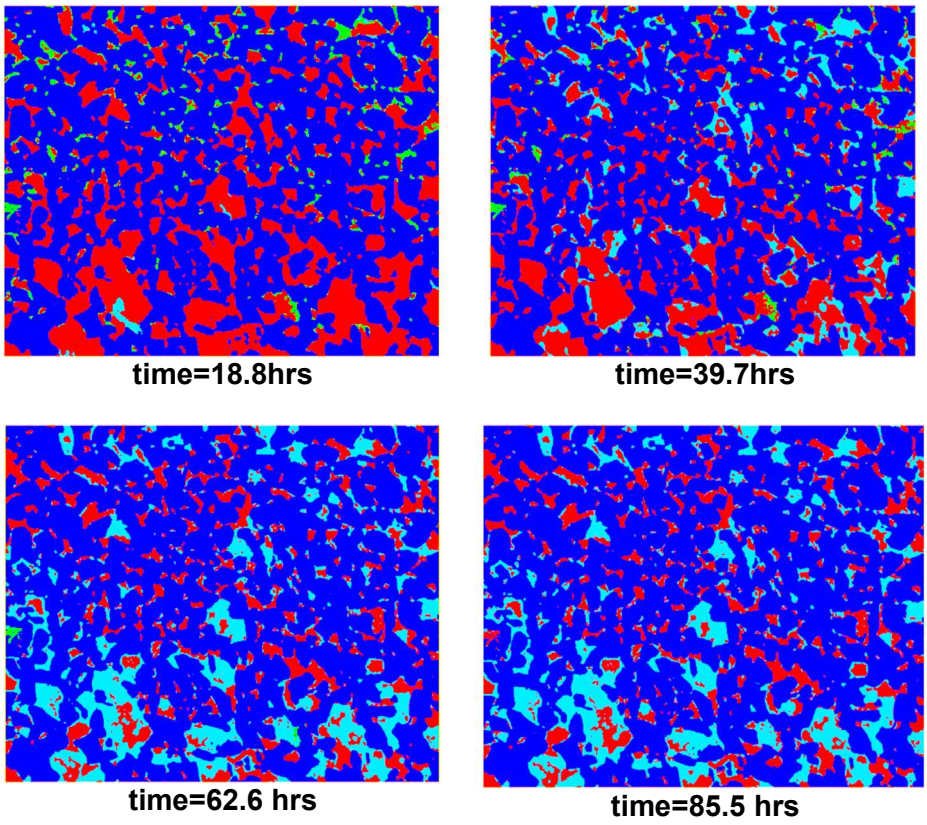


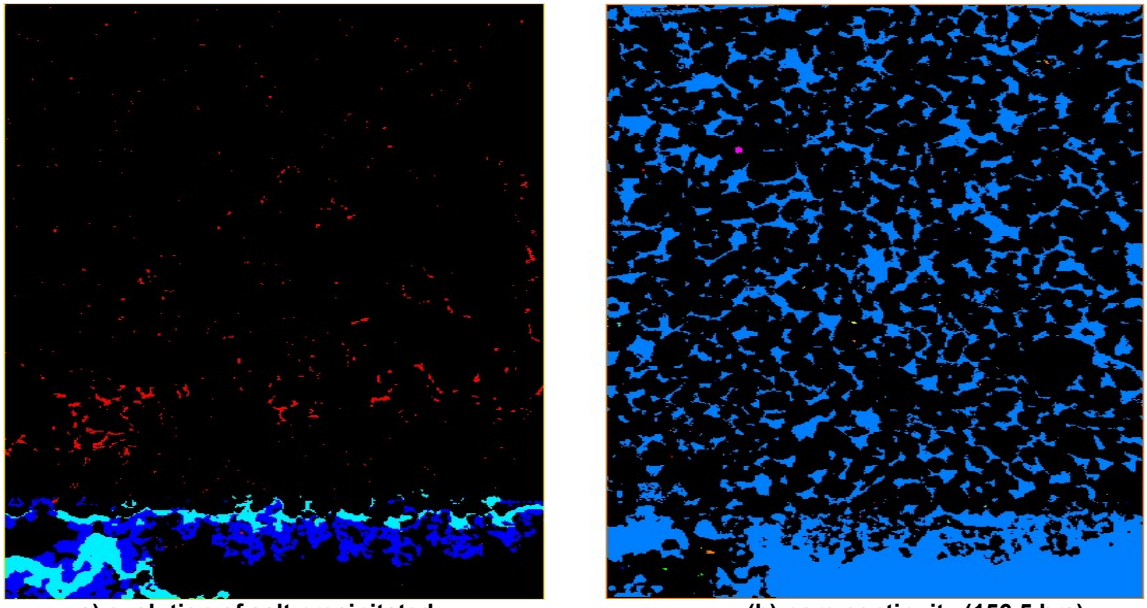
Figure 4-33 Precipitated salt of 6.4 Molal NaCl solution at the surface of the sample with different time steps using μ-CT dynamic images at 6 μm voxel size for Bentheimer in 40mm sample length with 12mm diameter at 60°C air temperature and RH~0%. (Dark blue: grains, Red: pore phase, light blue: salt and green: brine solution)

Figure 4-34 (a) focused on the changes of the salt distribution with time during the brine dry-out. In order to identify the progressive locations of precipitated salt in the sample with time, the μ-CT images were processed with time by grouping the grains, brine and pore space (black colour) and calculating the differences between subsequent images. It shows from this figure that salt was initially precipitated at the surface of the sample (light blue at 39.7 hrs). Due to the continuity of capillary connection to the surface, brine continued to transport through the pores to the surface where evaporation took place, resulting in an increase in the quantity of

the precipitated salt at the surface and this can be seen in dark blue at 62.6 hrs.

After 85.5 hrs (red colour), the drying-out salt was progressed towards the core of the sample, however, the amount of salt precipitated within the matrix at the end of the dry-out test was small. This indicates that during most of the square root time drying behaviour, the hydraulic connectivity between the surface of the sample and the liquid films in the core of the sample was maintained.

The observations regarding continuity of the connectivity through the pores can be seen in Figure 4-34 (b) where separated pore spaces have been labelled in different colours. This shows that almost all the pore space remains connected to the outside as blue is present in nearly all pores. The coloured spots seen in the Figure 4-34 (b) represent the disconnected pores. The observation from this study from Figures 4-34 (a, b) demonstrated that even though the drying regime was square root behaviour and salt was precipitated at the surface, the capillarity effect was still large enough to sustain brine transport to the sample surface, although the resolution of the CT images was not sufficient to observe the thin films making the connection directly



a) evolution of salt precipitated **(b) pore continuity (156.5 hrs)**

Figure 4-34 µ-CT images at 6 µm voxel size for the evolution of salt precipitated (light blue 39.7hrs, dark blue 67 and red & 85.5 hrs) and pore continuity for 6.4 Molal NaCl solution for Bentheimer

Desarnaud et al., (2015), studied the mechanisms of salt precipitation from porous media, specifically the primary or secondary nucleation. They reported three different regimes including; capillary regime which characterised by a constant evaporation rate, second regime

in which the evaporation rate decreases exponentially due to the crystal growth that reduces the evaporative surface area and diffusive regime, in which the evaporative flux scales as square root behaviour. They reported that in the square root regime, the porous medium is almost completely covered with salt and the speed of the capillary flow through the small pores of the crust was insufficient to compensate the evaporation. At this stage, Desarnaud suggested that the pores through the salt crust become dry initiating the diffusion control. This also implies that the salt crystallisation must progress from underneath the salt crust towards the interior of the stone core during the diffusion-controlled period.

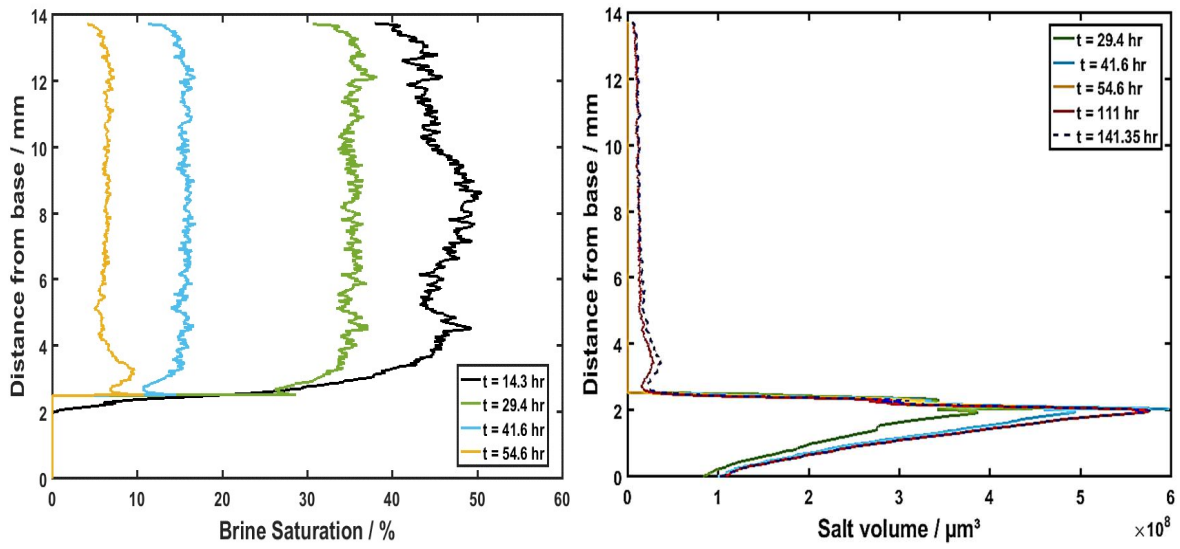
However, in this study, the μ-CT imaging analysis demonstrated that salt deposition during the square root drying regime occurred at the surface of the sample. As discussed previously, this indicated liquid was present at this location, supplying the evaporation and therefore that hydraulic connectivity was maintained to transport salt from the sample core to the surface. The pores through the salt deposit cannot have been dry in these experiments. Note that some quantity of salt was precipitated in the sample core and that is during the later stage of the square root drying regime.

4.2.3 μ-CT Image Analysis for Brine with 6.4 Molal at 15 μm voxel size

The objective of the μ-CT images at 15 μm was to cover the entire surface of the sample (which can be seen in the higher resolution images) and provide a more global view of the drying-out process.

Figure 4-35 (a) illustrates the average brine saturation versus sample depth and that at different time steps for Bentheimer. A brine solution of 6.4 Molal NaCl was used for this test. During the early stage of evaporation, brine solution was evaporated at sample surface and that between 0hr and 14.3hrs. Also, salt precipitation was not observed at the surface of the sample.

From Figure 4-35 (b), during the period between 29.4 hrs and 54.6hrs, salt deposition occurred at the sample surface with an average brine saturation of approximately 35% at 29.4hrs, 15% at 41.6hrs and less than 10% at 54.6 hrs. From Figure 4-35 (b), it can be observed that salt continuously deposited at surface of the sample with time implying continuity of the hydraulic connectivity between sample surface and liquid film. Only after 56 hrs some salt began to deposit within the matrix indicating that the liquid films could not maintain saturated water vapour in those pores.



a) brine saturation **(b) precipitated salt volume**

Figure 4-35 Brine (6.4 Molal) saturation and salt precipitation volume versus distance from exposed face with time using µ-CT dynamic images at 15 µm for Bentheimer in 40mm sample length with 12mm diameter at 60°C air temperature and RH~0%

Figure 4-36 shows the change of the sample surface structure because of precipitated salts which resulted in a reduction in the drying rate. Based on Figure 4-36, it can be deduced that liquid film detachment was maintained even during the square root behaviour. From above Figure 4-35 (b) and Figure 4-36, it can be observed that between 111hrs and 141.35hrs that brine saturation was no longer evident in the images, and as a result, salt precipitation was no longer occurring at the surface of the sample. Similar to µ-CT 6 µm observation salt precipitation occurred within the matrix, but it was less than 5% of the total precipitated salt.

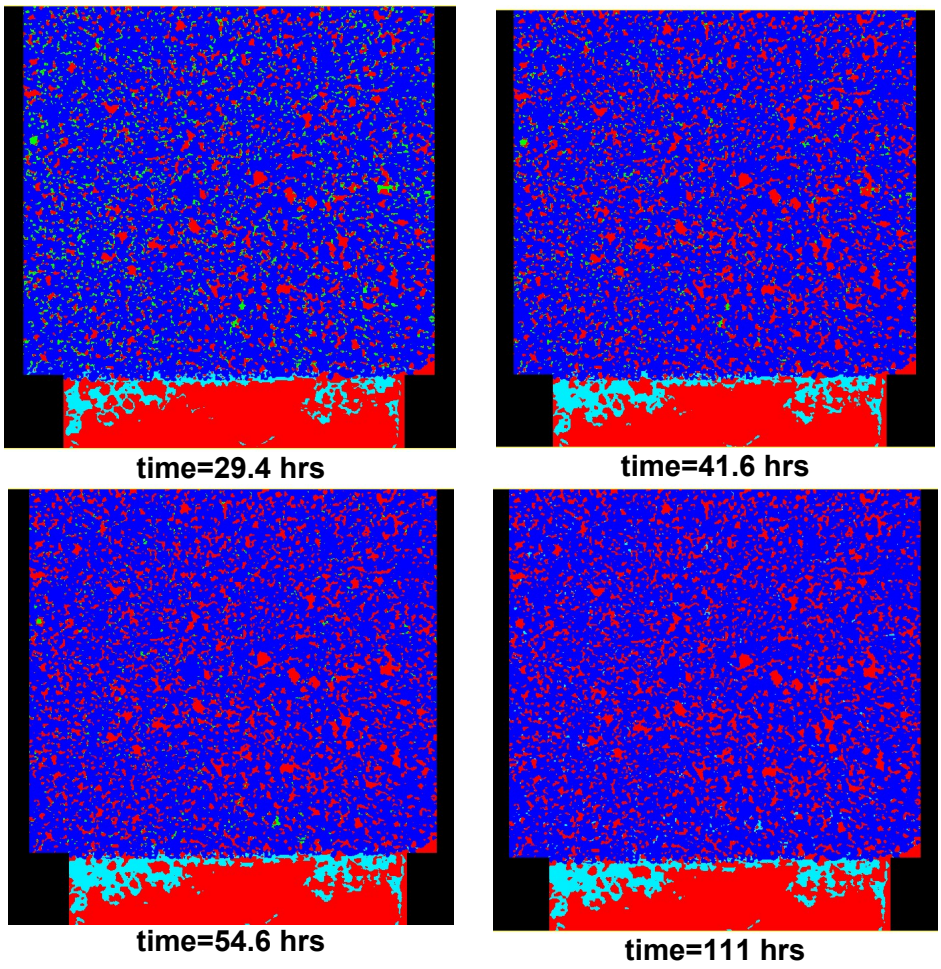


Figure 4-36 Precipitated salt of 6.4 Molal NaCl solution different time steps using µ-CT dynamic images at 15 µm voxel size for Bentheimer in 40mm sample length with 12mm diameter at 60°C air temperature and RH~0%. (Dark blue: grains, Red: pore phase, light blue: salt and green: brine solution)

Figure 4-37 shows the difference images of the salt at the surface sample developing with time. It shows that salt was initially precipitated at the surface of the sample (light blue at 29.4 hrs). Further in the drying, the precipitated salt continued to increase outwards at 41.6hrs (dark blue). At 54.6hrs (in red) the picture was more complicated with salt growing on the outer surface in some places and within the larger salt pores in other places. After that liquid film was completely detached from the surface and at 111hrs salt started to appear inside the matrix (in green) and no further salt was deposited on the outside of the sample.

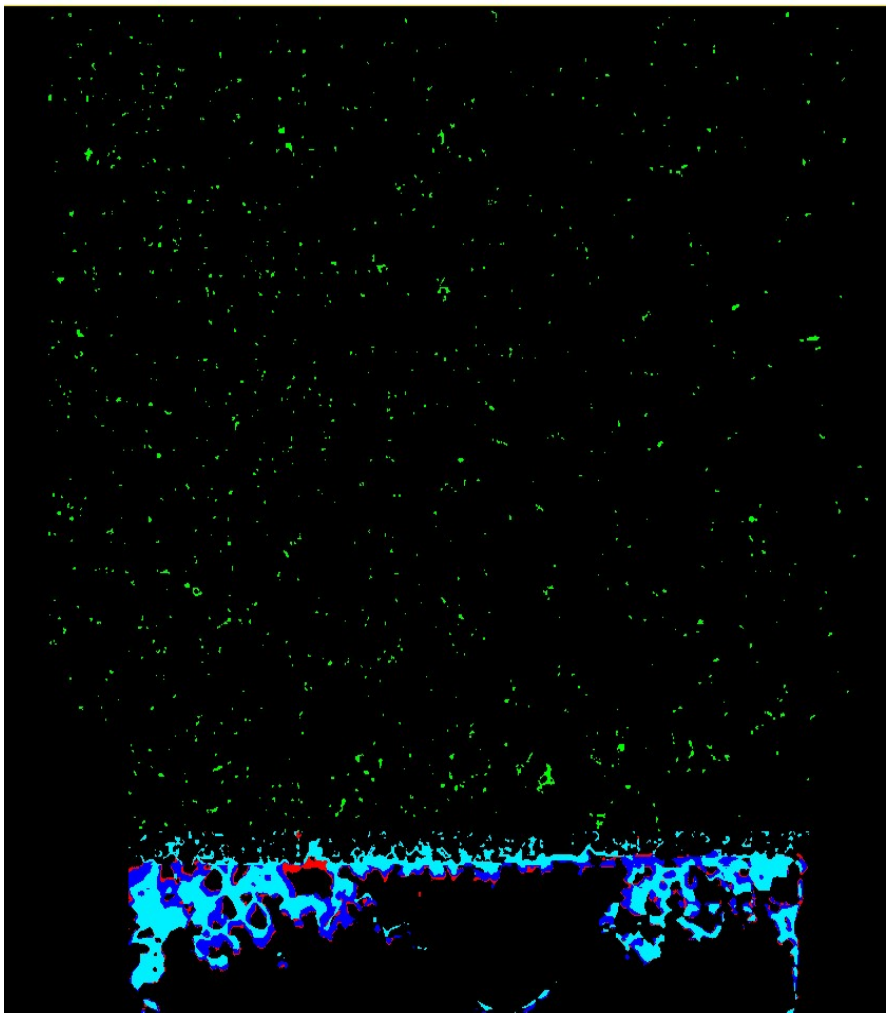


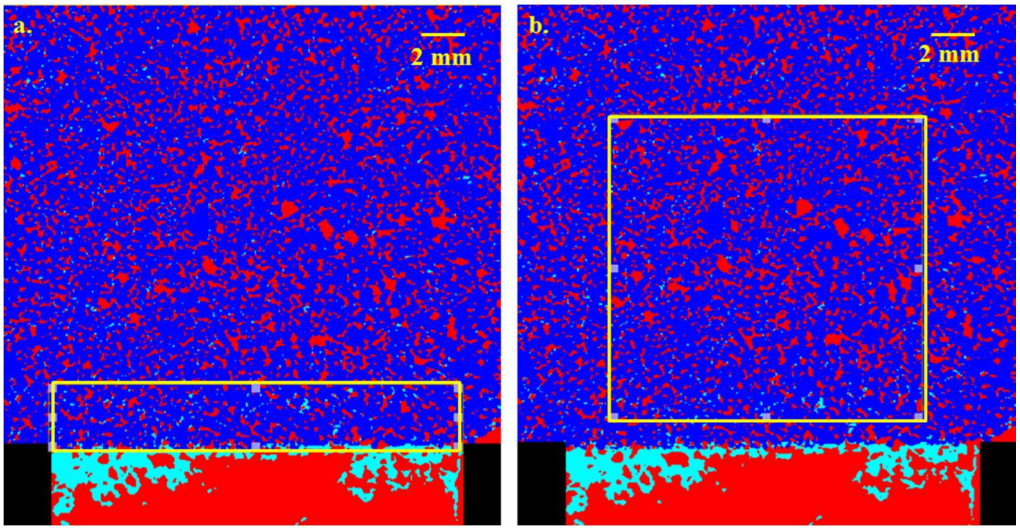
Figure 4-37 The evolution of salt Precipitated 6.4 Molal NaCl solution at the surface of the sample with different time steps using µ-CT dynamic images at 15 µm voxel size for Bentheimer. At 29.4hrs (light blue), at 41.6hrs (dark blue), at 54.6hrs (in red) and at 111hrs (in green)

From the dynamic µ-CT imaging at both resolutions, it was apparent that the location of the evaporation was on the outside of the salt deposit for much of the process and loss of the capillary connection cannot have been responsible for the development of the square root relationship between evaporation and time, in contradiction to the observations by Desarnaud et al., (2015). We propose that drying rate becomes low due to the development of dry patches at the sample surface reducing the area available for evaporation. Unfortunately, this cannot be directly confirmed in this study due to the wetting layers being below the resolution of the images, therefore, as a way forward, it is recommended to perform further investigation in this area using a higher imaging resolution and a longer core sample. A higher time resolution would also be useful in demonstrating the sequence of deposition on the sample surface.

4.3 Pore-scale modelling

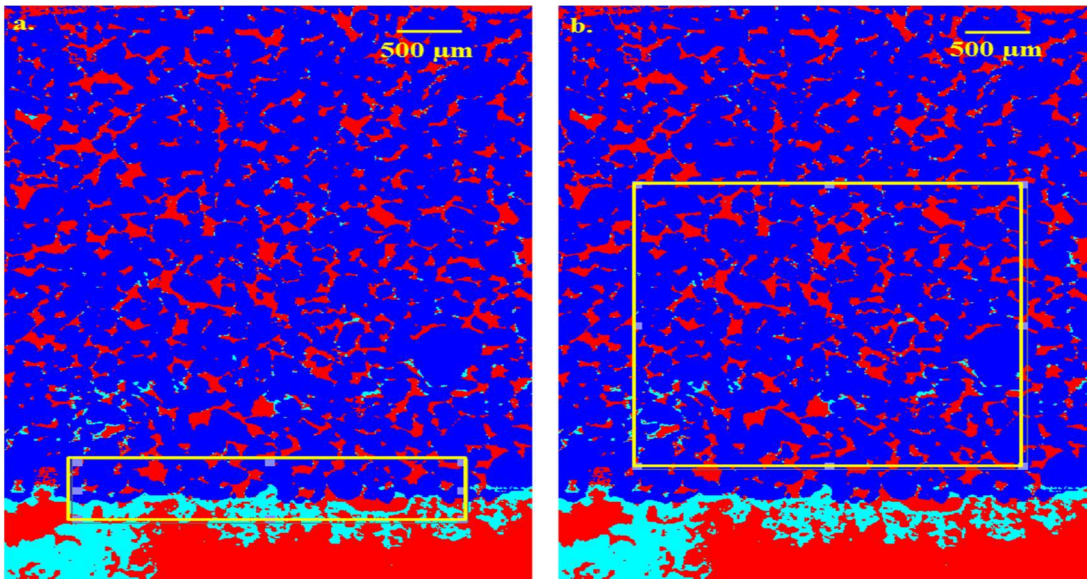
A model developed by Yang & Boek (2013) was used to calculate the permeability reduction in porous media due salt precipitation. It was a lattice Boltzmann method based simulator which can calculate the flow field directly on binary images of a pore space. The viscosity, density and magnitude of pressure gradient/body force should be set before the simulation. The velocity field was calculated and the permeability of the sample can be predicted using the velocity field. This will allow estimation of the permeability of the salt deposit directly from the micro-CT image.

In this study, LB simulations were done on two sets of acquired 3D pore scale images obtained at 15 µm and 6 µm voxel resolution. The different 3D simulation boxes (sub-volumes) for the respective voxel resolutions were selected using Avizo to fulfil the purpose of calculating salt layer and matrix permeability of the sample during the dry-out experiment are shown in Figures 4-38 and 4-39.



(a) Sub-volume at the salt layer (b) Sub-volume at the matrix

Figure 4-38 2D segmented (xz orientation) slice of 3D pore-scale image of Bentheimer sandstone acquired at 15 µm voxel resolution during the dry-out experiments. (a) Sub-volume (668 x 128 x 110 voxels) to calculate salt layer LB single phase permeability. (b) Sub-volume (500 x 500 x 500 voxels) to calculate matrix LB single phase permeability. The dark blue represents grain phase, light blue represents salt deposition and red colour represents pore phase.



(a) Sub-volume at the salt layer (b) Sub-volume at the matrix

Figure 4-39 2D segmented (xz orientation) slice of 3D pore-scale image of Bentheimer sandstone acquired at 6 µm voxel resolution during the dry-out experiments. (a) Sub-volume (500 x 500 x 110 voxels) to calculate salt layer LB single phase permeability. (b) Sub-volume (500 x 500 x 500 voxels) to calculate matrix LB single phase permeability. The dark blue represents grain phase, light blue represents salt deposition and red colour represents pore phase.

The resulting 3D sub-volumes were segmented into binary images (pore phase as black and grain + salt deposition phase as white) as shown in Figure 4-40 to calculate the single-phase LB permeability. The lattice Boltzmann algorithm developed by Yang & Boek (2013) was used for simulating single phase flow directly on micro-CT images of porous media.

The fluid flow was driven by applying a constant body force (pressure gradient) in the direction parallel to the axis of the core and periodic boundary conditions in all directions; periodic means that the fluid exiting the simulation domain at the outlet enters the system at the inlet. The LB calculation was run on an NVIDIA Tesla K20 GPU with a 5GB global memory.

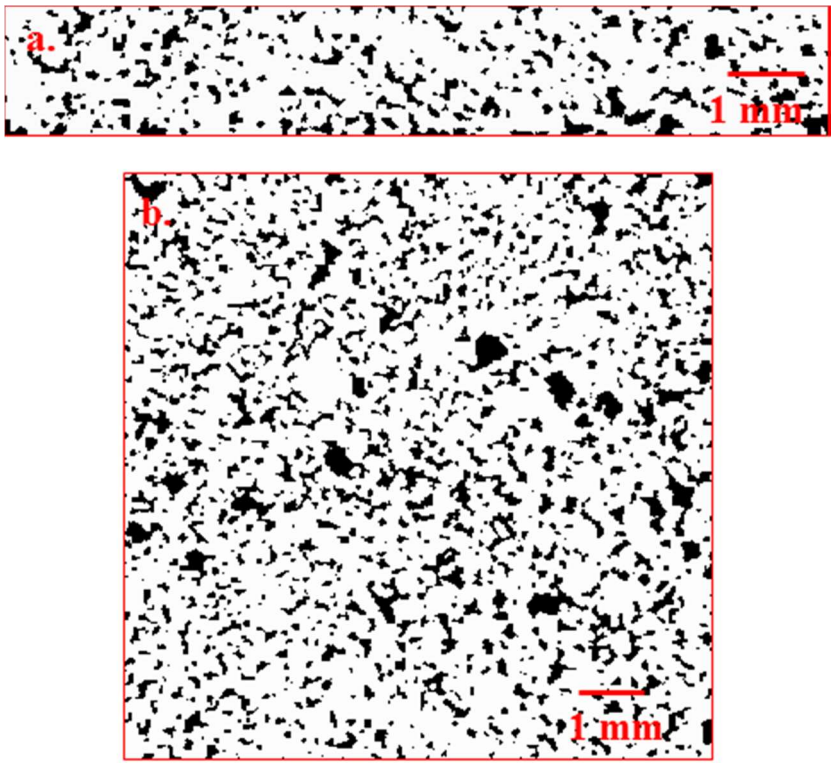
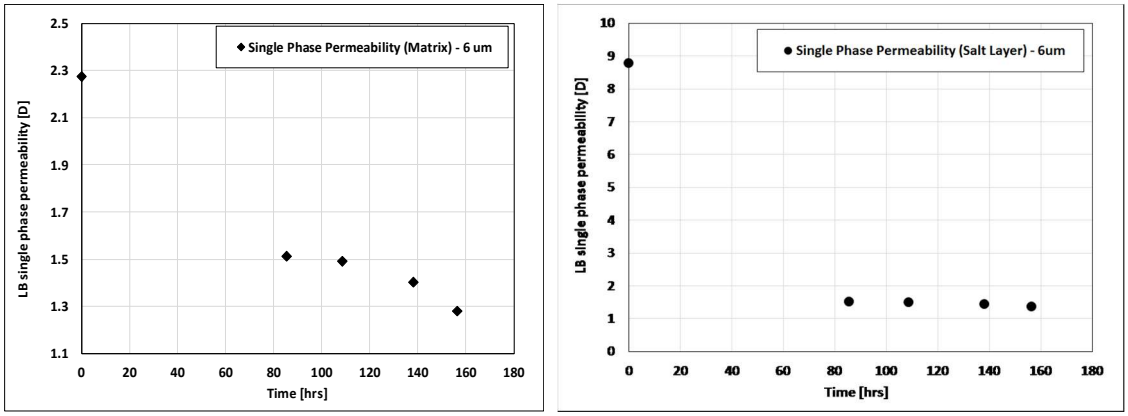
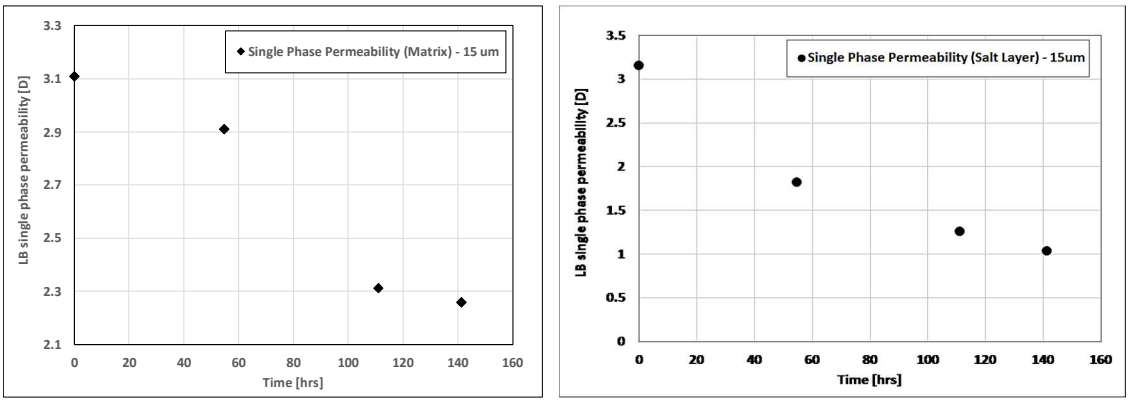


Figure 4-40 2D binary (xz orientation) slice of 3D pore-scale image of Bentheimer sandstone acquired at 15 µm resolution for LB single phase permeability simulation. (a) Sub-volume to calculate salt layer permeability (b) Sub-volume to calculate matrix permeability. The black colour represents pore space and white colour represents grain + salt deposited.



(a) Matrix **(b) salt layer**

Figure 4-41 Calculated LB single phase permeability for Bentheimer sandstone scanned at 6 µm voxel resolution. (a) Matrix permeability and (b) Salt layer permeability



(a) Matrix **(b) Salt Layer**

Figure 4-42 Calculated LB single phase permeability for Bentheimer sandstone scanned at 15 µm voxel resolution. (a) Matrix permeability and (b) Salt layer permeability.

The initial dry condition sub-volume was selected to calculate salt layer LB single phase permeability as the reference permeability. The dry condition salt layer LB permeability is overestimated due to the inclusion of the open space in the sub-volume representing pore phase in the flow. As the dry-out takes place over the time, the salt starts to deposit around the open space of the fracture and LB single phase permeability is predicted for different time for the same sub-volume size selected for the initial dry case. However, the total permeability is calculated taking the sum of both the matrix and salt layer permeability. This can be calculated by doing the harmonic-average permeability as shown in the equation below:

$$k_{avg} = \frac{L_T}{\frac{L_1}{k_1} + \frac{L_2}{k_2}} \qquad \text{Equation (6)}$$

where L_T = total length of all sub-volumes $L_1 + L_2$

k_1 and k_2 : absolute permeability of sub-volumes

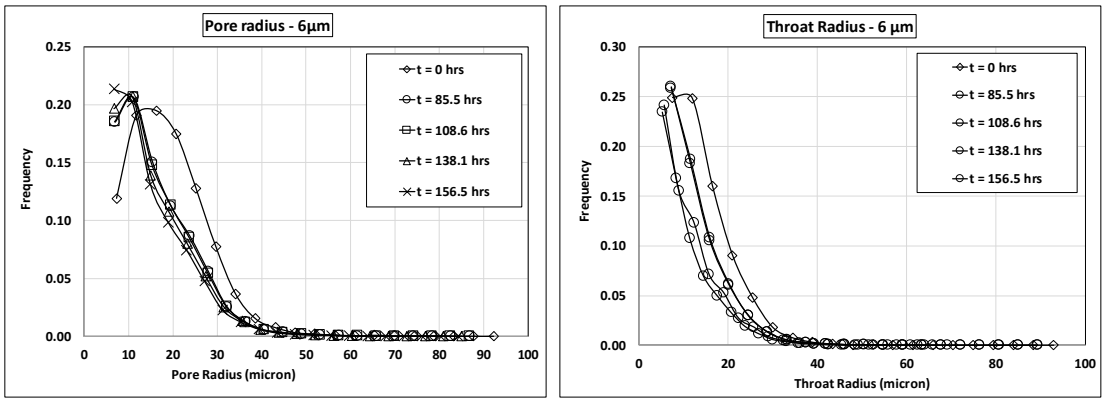
The experimental absolute permeability through the core and later the salt/core system was measured before and after the dry-out experiment by flowing CO_2 at different flow rates and using Darcy's law to estimate the permeability. The experimental permeability was reduced by 81 % from 2.2 D to 0.41 D by the salt deposition. The calculated LB single phase permeability shows a reduction by 54% from 2.27 D to 1.28 D at 6 µm scanned voxel resolution and 54% from 2.7D to 1.48D at 15um scanned voxel resolution. The results were similar to the observation made by Peysson (2011), who saw a reduction in the permeability by 90% in his experiments. Therefore, in all cases it seems that the sample retained significant permeability to allow CO_2 to flow into matrix.

4.3.1 Network modelling

The network extracted pore space properties give additional insight into dry-out phenomena taking place at pore-scale. The network geometry from the brine dry-out in situ CT sub-volume data used for LB flow simulation scanned at 6 µm voxel resolution is shown in Table 4-4 and Figure 4-43 (a) and (b) while network extracted from 15 µm voxel resolution is shown in Table 4-5 and Figure 4-44 (a) and (b). Referring to Table 4-4 and Table 4-5, the average coordination number goes on decreasing as the salt starts to get deposited over the time and hence we observe decrease in matrix permeability for 6 µm and 15 µm voxel resolution scans (refer Figure 4-41 and 4-42). The number of pores and throats have approximately doubled from initial to final conditions for 6 µm resolution (see Table 4-4) due to salt deposits producing new throats inside large pores which were then divided into two or more bodies. Figure 4-43 (a) and (b) shows the shift in the pore and throat radius distribution decreasing from initial to final conditions. In contrast, referring to Table 4-5 for 15 µm resolution, the number of pore and throats have decrease insignificantly and does not follow the same trend as in the 6 µm resolution scan due to the coarser resolution scan which only captures pores and throats greater than 15 µm.

Table 4-4 Pore space network properties of Bentheimer sandstone for selected matrix sub-volume scanned at 6 µm voxel resolution.

Time (hours)	Number of pores	Number of throats	Average coordination number
0	13779	24490	3.52
85.5	21339	35060	3.28
108.6	21485	35363	3.27
138.1	23118	37624	3.23
156.5	25318	40765	3.20

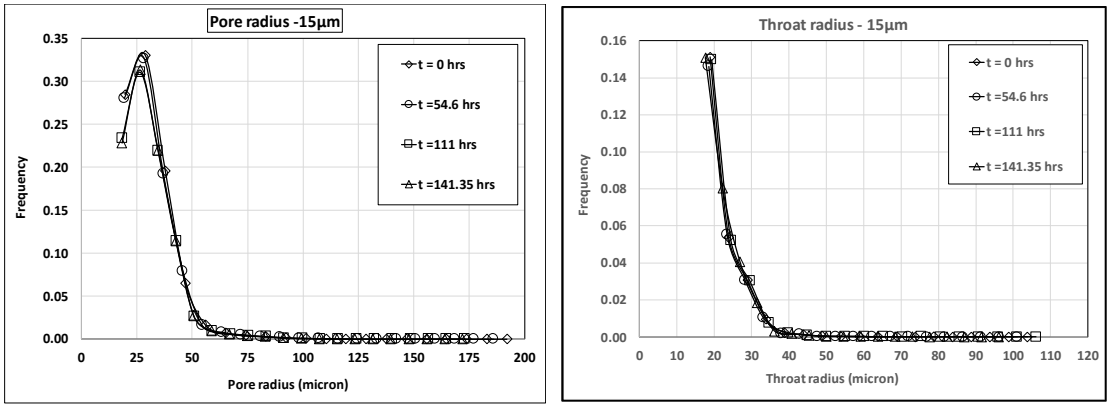


(a) Pore radius **(b) Throat radius**

Figure 4-43 Frequency distribution of Bentheimer sandstone scanned at 6 µm voxel resolution. (a) Pore radius and (b) Throat radius.

Table 4-5 Pore space network properties of Bentheimer sandstone for selected matrix sub-volume scanned at 15 µm voxel resolution.

Time (hours)	Number of pores	Number of throats	Average coordination number
0	55269	107666	3.67
54.63	55490	108456	3.63
111.03	53382	93283	3.43
141.35	52982	90657	3.41



(a) Pore radius **(b) Throat radius**

Figure 4-44 Frequency distribution of Bentheimer sandstone scanned at 15 µm voxel resolution. (a) Pore radius and (b) Throat radius.

Chapter 5

5 Conclusions and Recommendations

5.1 Conclusions

The existing CO_2 storage projects have provided the research into CCS with vast operational experience in aquifer reservoir modelling and multiphase flow dynamic behaviour during CO_2 injection. However, gaps still exist in the understanding of the fluid dynamics, fluid interaction with the rocks and salt precipitation phenomena inherent to the CO_2 storage process. The reason for this is mainly because the process and the implementation of CCS projects often follows the methods used for oil and gas recovery, without detailed consideration of the interactions of the injected CO_2 with brine and the rock in the aquifer. For example, the projects where dry CO_2 was injected, e.g. Snøhvit and In Salah, met with challenges due to severe injectivity decline (Eiken et al., 2011; Hansen et al., 2013).

However, core plugs from Snøhvit were experimentally investigated. They showed that CO_2 injection resulted in precipitated salt at the pore throats resulted in a noticeable reduction in permeability and well injectivity (Grude et al., 2013).

Further experimental investigations and pore network modelling have confirmed the salt precipitation during CO_2 injection, resulting in reduction in formation permeability. However, whether a reduction in formation permeability may lead to impairment in well injectivity still remains to be further assessed. Muller et al., (2009) and Peysson et al., (2014) reported that during evaporation periods the capillary-driven backflow could lead to salt precipitation in the vicinity of well injection point, resulting in a sharp reduction in the injectivity.

Selective detailed reviews from previous experimental investigations and numerical simulations of the evaporation process and salt precipitation during dry-out in porous media were presented in this thesis. The research covered the kinetics and stages of drying for water and saline conditions during evaporation from porous media. Also, the effect of capillarity, viscosity and gravity forces on the different stages of the dry-out stages was addressed through the magnitudes of the dimensionless Bond number, capillary effect and Peclet numbers. The study covered the loss of porosity, permeability, and well injectivity caused by the salt precipitation during formation dry-out which eventually results in well clogging. Previous work showed that the location of the precipitate depends on the competition of

advective and capillary forces on the aqueous fluid phase transporting brine to the drying front. Here we considered the drying process of reservoir brine in fractured porous media by the injection of sub-saturated CO_2. In the case of a heavily fractured reservoir, the injected CO_2 started drying the fracture-matrix interface, which resulted in capillary driven transport of brine and salt to the fracture-matrix interface, where it precipitated.

In this research, dry-out evaporation tests were performed. The objective of the experimental study in this thesis was to investigate the effect of injecting CO_2 into the fracture and to study the mass transfer between matrix and fracture orthogonal to the flow direction in the fracture. Also, to investigate the dry-out that occurs due to the transport of water from the brine saturated region of the matrix to the fracture (assumed dry and filled with CO_2) and the deposition of salt in the matrix or the fracture.

The evaporative drying kinetics and salt precipitation were investigated through the use of a combination of gravimetric and X-ray µ-CT techniques to measure the water and brine saturation distribution and salt precipitation in various rock test samples.

The gravimetric tests were focused on the kinetics of drying for pure water and for NaCl solutions of 3.0 and 6.4 Molality. In the gravimetric tests the only data available were the mass loss due to evaporation as a function of time and the emphasis therefore was on investigating the transitions between the drying regimes. To assess the effect of temperature on the drying periods different air temperatures were used, including 30°C, 60 °C, 90 °C and 95 °C, operating at approximately relative air humidity. The effect of sample size on the evaporation rate and drying kinetics was assessed for short sample (20mm), medium samples (40mm and 80mm) and long sample (242mm), all at 12mm diameter. Also, the effect of different types of rock on the characteristics of the drying out periods was assessed using Bentheimer sandstone and Ketton carbonate.

µ-CT dynamic imaging experiments were also performed; the key objectives of the µ-CT dynamic imaging analysis were to understand the drying regime behaviour during the salt precipitation and assess the effect of the precipitated salt on the continuity of the hydraulic connectivity and liquid film detachment. Also, the µ-CT dynamic images were used to identify the location of salt precipitation during the dry-out and estimate the impact of the precipitated salt on the permeability of the system by flow modelling in the segmented CT images.

Based on the gravimetric results presented above for De-ionised water and 3.0 Molal and 6.4 Molal NaCl solutions, the following can be concluded:

- Initially, before solid salt was deposited, the drying curves for de-ionised water and NaCl solutions of 3.0 Molal and 6.4 Molal were similar, therefore at this stage the presence of salt acts only through the depression of vapour pressure.
- However, during the constant period of evaporation rate, capillary forces keep the liquid connected to the outer surface of the core and this resulted in the transport of salt ions towards the that location. When this salt ion accumulation exceeded the saturation concentration, crystallisation occurred resulting in the formation of an efflorescence. The Peclet number was estimated to be ~212 during the early stage of evaporation indicating that the diffusion of ions away from the surface was very limited. Towards the end of the dry-out the Peclet number reached approximately one, however this was based on a length scale taken from the pore size. This indicated that salt continued to be transported to the location of evaporation and deposited locally.
- For Bentheimer sandstones, deviation of the drying rate from the initial constant rate period began at an earlier time for 6.4 Molal NaCl solution compared with 3.0 Molal, as expected. This was a consequence of the salt precipitated at the surface of the sample reducing the drying rate.
- During the evaporation of brine, the drying began with a linear mass loss as a function of time, followed by square root behaviour for the drying regime shortly after salt deposition began, with a short transition between the two regimes.
- The μ-CT images obtained at the end of gravimetric dry-out tests, showed that salt was mainly precipitated at the surface of the sample. However, minor amounts of salt were observed precipitated in the interior of the sample.
- The precipitated salt layer at the surface of the sample imaged at the end of the dry-out tests remained porous and the pores remained hydraulically connected through the salt to the rock matrix below, despite a low porosity.

Based on the evaporation tests for Bentheimer sandstone using the in situ μ-CT method for de-ionised water and NaCl solutions 6.4 Molal, the following can be concluded;

- It was observed that during most of the dry-out periods, salt was continuously deposited at the surface of the sample indicating that evaporation occurred mostly at this position and advective salt ion transport regime in the liquid phase dominated diffusive transport deeper into the matrix, as expected from the large Peclet number estimate given above.

- The amount of precipitated salt increased with time and this resulted in a change of the pore structure at the surface of the sample, consequently reducing the brine drying rate. This observation agreed with the gravimetric tests results.
- Unfortunately, the μ-CT images were of insufficient resolution to directly observe the thin liquid layers maintaining the hydraulic conductivity to the point of evaporation inferred from the location of the expanding salt deposit.
- Towards the end of evaporation, the precipitated salt progressed towards the core of the sample. However, the amount of salt precipitated within the matrix at the end of the dry-out test was small. This indicated that for the sample size used, the hydraulic connectivity between the surface of the sample and the liquid films was only interrupted at a low saturation, approaching the completely dry state.

Based on the permeability measurements and LB single-phase permeability predictions, it was concluded that;

- From the permeability measurement on the entire rock/salt deposit system, it was demonstrated that the permeability was reduced by 81 % from 2.2 D to 0.41 D.
- However, the calculated LB single phase permeability of the two sets of acquired 3D pore scale images obtained at 15 μm and 6 μm voxel resolution showed a reduction by 54% from 2.27 D to 1.28 D at 6 μm scanned voxel resolution and 54% from 2.7 D to 1.48 D at 15 μm scanned voxel resolution.

Therefore, it can be concluded that the sample at the end of the drying out tests maintained good permeability to allow CO_2 to flow into matrix.

Based on the experimental investigations in this research for the dry-out under saline conditions, it can be concluded that for a CCS project in a fractured formation, salt precipitation would occur initially in the fractures, resulting in a reduction of permeability of both fracture and the near fracture matrix. However, this reduction would be limited and would not result in the loss of connection between matrix and fracture. On the contrary, the reduced fracture permeability could be an advantage and force the CO_2 to migrate through regions that would not otherwise be swept with a highly permeably fracture network.

5.2 Recommendations

Based on the above concluded dry-out experimental investigations, further research work is recommended to be undertaken to investigate further the CCS drying out and dynamic salt precipitation mechanism in aquifer reservoir, including;

- Conduct μ-CT dynamic imaging experiments at higher resolutions near the sample surface to better understand the liquid hydraulic connectivity during the salt precipitation at the interface between the fracture and formation matrix. Also, more frequent images should be obtained during the initial drying of the sample when salt starts to form. This requires a better time resolution with more scans to capture the evolution of salt precipitation. The limitations due to μ-CT apparatus used in this study could be overcome by using alternative facilities such as synchrotron μ-CT which has a much more rapid image acquisition.
- This study focused on using simple NaCl brine solutions. A careful analysis of the influence of complex brines on the structure of the salt deposits should be undertaken to represent potential CCS aquifers where injection could be of interest to oil and gas companies.
- Using the μ-CT dynamic imaging processing test, conduct further assessments to better understand the effect of the fracture width (the empty upper part of the sample) on the permeability reduction, the evaporation regimes and the dynamic salt precipitation mechanism.
- Similarly to Shokri & Or (2011), where they used rectangular glass columns, extensive μ-CT dynamic experiments could be done on other rock types with a wider range of permutabilities and heterogeneity. Much longer samples than those used in the current work could be used to estimate the depth of desaturation at which the capillary connection to the surface breaks and hence predict the transition to diffusion controlled evaporation rate.
- To understand further the impact of this research findings on CCS process in aquifer reservoir, field trial tests will be recommended so as to assess the impact of salt precipitation on the formation permeability and well injectivity. Alternatively, longer sample test will be recommended to be used.

6 Bibliography

André, L., Audigane, P., Azaroual, M., & Menjoz, A. (2007). Numerical modeling of fluid–rock chemical interactions at the supercritical CO2–liquid interface during CO2 injection into a carbonate reservoir, the Dogger aquifer (Paris Basin, France). *Energy conversion and Management, 48*(6), 1782-1797. doi: http://dx.doi.org/10.1016/j.enconman.2007.01.006

André, L., Peysson, Y., & Azaroual, M. (2014). Well injectivity during CO2 storage operations in deep saline aquifers – Part 2: Numerical simulations of drying, salt deposit mechanisms and role of capillary forces. *International journal of greenhouse gas control, 22*, 301-312. doi: http://dx.doi.org/10.1016/j.ijggc.2013.10.030

Andrew, M., Bijeljic, B., & Blunt, M. J. (2013). Pore-scale imaging of geological carbon dioxide storage under in situ conditions. *Geophysical Research Letters, 40*(15), 3915-3918.

Andrew, M. G. (2015). *Reservoir-Condition Pore-Scale Imaging of Multiphase Flow.* Imperial College London.

Babalis, S. J., & Belessiotis, V. G. (2004). Influence of the drying conditions on the drying constants and moisture diffusivity during the thin-layer drying of figs. *Journal of Food Engineering, 65*(3), 449-458. doi: http://dx.doi.org/10.1016/j.jfoodeng.2004.02.005

Bachu, S. (2000). Sequestration of CO 2 in geological media: criteria and approach for site selection in response to climate change. *Energy conversion and Management, 41*(9), 953-970.

Bachu, S., & Adams, J. (2003). Sequestration of CO 2 in geological media in response to climate change: capacity of deep saline aquifers to sequester CO 2 in solution. *Energy conversion and Management, 44*(20), 3151-3175.

Bachu, S., Gunter, W., & Perkins, E. (1994). Aquifer disposal of CO 2: hydrodynamic and mineral trapping. *Energy conversion and Management, 35*(4), 269-279.

Beauheim, R. L., & Roberts, R. M. (2002). Hydrology and hydraulic properties of a bedded evaporite formation. *Journal of Hydrology, 259*(1), 66-88.

Bickle, M. J. (2009). Geological carbon storage. *Nature Geosci, 2*(12), 815-818.

Bico, J., Thiele, U., & Quéré, D. (2002). Wetting of textured surfaces. *Colloids and Surfaces A: Physicochemical and Engineering Aspects, 206*(1), 41-46.

Blunt, M. (2010). Carbon dioxide storage. *Grantham Institute Briefing Paper, 4*.

Bradshaw, J., Bachu, S., Bonijoly, D., Burruss, R., Holloway, S., Christensen, N. P., & Mathiassen, O. M. (2007). CO 2 storage capacity estimation: issues and development of standards. *International journal of greenhouse gas control, 1*(1), 62-68.

Buades, A., Coll, B., & Morel, J.-M. (2005). *A non-local algorithm for image denoising.* Paper presented at the 2005 IEEE Computer Society Conference on Computer Vision and Pattern Recognition (CVPR'05).

Buades, A., Coll, B., & Morel, J.-M. (2008). Nonlocal image and movie denoising. *International journal of computer vision, 76*(2), 123-139.

Buffiere, J.-Y., Maire, E., Adrien, J., Masse, J.-P., & Boller, E. (2010). In situ experiments with X ray tomography: an attractive tool for experimental mechanics. *Experimental mechanics, 50*(3), 289-305.

Burger, W., Burge, M. J., Burge, M. J., & Burge, M. J. (2009). *Principles of Digital*

Image Processing: Springer.
Casas, E., & Lowenstein, T. K. (1989). Diagenesis of saline pan halite; comparison of petrographic features of modern, Quaternary and Permian halites. *Journal of Sedimentary Research, 59*(5), 724-739. doi: 10.1306/212f905c-2b24-11d7-8648000102c1865d
Chauvet, F., Duru, P., Geoffroy, S., & Prat, M. (2009). Three Periods of Drying of a Single Square Capillary Tube. *Physical Review Letters, 103*(12), 124502.
Desarnaud, J., Derluyn, H., Carmeliet, J., Bonn, D., & Shahidzadeh, N. (2014). Metastability limit for the nucleation of NaCl crystals in confinement. *The journal of physical chemistry letters, 5*(5), 890-895.
Desarnaud, J., Derluyn, H., Molari, L., de Miranda, S., Cnudde, V., & Shahidzadeh, N. (2015). Drying of salt contaminated porous media: effect of primary and secondary nucleation. *Journal of Applied Physics, 118*(11), 114901.
Eiken, O., Ringrose, P., Hermanrud, C., Nazarian, B., Torp, T. A., & Høier, L. (2011). Lessons learned from 14 years of CCS operations: Sleipner, In Salah and Snøhvit. *Energy Procedia, 4*, 5541-5548.
El-Maghraby, R. M. N. A. (2013). *Measurements of CO_2 trapping in carbonate and sandstone rocks.* Imperial College London.
Eloukabi, H., Sghaier, N., Ben Nasrallah, S., & Prat, M. (2013). Experimental study of the effect of sodium chloride on drying of porous media: The crusty–patchy efflorescence transition. *International Journal of Heat and Mass Transfer, 56*(1–2), 80-93. doi: http://dx.doi.org/10.1016/j.ijheatmasstransfer.2012.09.045
Eloukabi, H., Sghaier, N., Prat, M., & Ben Nassrallah, S. (2011). Drying Experiments in a Hydrophobic Model Porous Medium in the Presence of a Dissolved Salt. *Chemical Engineering & Technology, 34*(7), 1085-1094. doi: 10.1002/ceat.201100064
Ennis-King, J., & Paterson, L. (2002). *Engineering aspects of geological sequestration of carbon dioxide.* Paper presented at the SPE Asia Pacific Oil and Gas Conference and Exhibition.
Falkowski, P., Scholes, R., Boyle, E., Canadell, J., Canfield, D., Elser, J., Gruber, N., Hibbard, K., Högberg, P., & Linder, S. (2000). The global carbon cycle: a test of our knowledge of earth as a system. *science, 290*(5490), 291-296.
Farifteh, J., Van der Meer, F., Atzberger, C., & Carranza, E. J. M. (2007). Quantitative analysis of salt-affected soil reflectance spectra: A comparison of two adaptive methods (PLSR and ANN). *Remote Sensing of Environment, 110*(1), 59-78. doi: http://dx.doi.org/10.1016/j.rse.2007.02.005
Fonseca, P. C., & Scherer, G. W. (2015). An image analysis procedure to quantify the air void system of mortar and concrete. *Materials and Structures, 48*(10), 3087-3098. doi: 10.1617/s11527-014-0381-9
Fuller, R. C., Prevost, J. H., & Piri, M. (2006). Three-phase equilibrium and partitioning calculations for CO2 sequestration in saline aquifers. *Journal of Geophysical Research: Solid Earth, 111*(B6), n/a-n/a. doi: 10.1029/2005JB003618
Gharbi, O., & Blunt, M. J. (2012). The impact of wettability and connectivity on relative permeability in carbonates: a pore network modeling analysis. *Water Resources Research, 48*(12).
Giorgis, T., Carpita, M., & Battistelli, A. (2007). 2D modeling of salt precipitation during the injection of dry CO2 in a depleted gas reservoir. *Energy conversion and Management, 48*(6), 1816-1826. doi: http://dx.doi.org/10.1016/j.enconman.2007.01.012

Goldberg, P., Chen, Z.-Y., O'Connor, W., Walters, R., & Ziock, H. (2001). CO2 mineral sequestration studies in the US: National Energy Technology Laboratory, Pittsburgh, PA (United States).

Gonzales, R. C., & Wintz, P. (1987). Digital image processing.

Grude, S., Dvorkin, J., Clark, A., Vanorio, T., & Landrø, M. (2013). Pressure effects caused by CO2 injection in the Snøhvit field. *first break, 31*(12).

Gunter, W., Wiwehar, B., & Perkins, E. (1997). Aquifer disposal of CO2-rich greenhouse gases: extension of the time scale of experiment for CO2-sequestering reactions by geochemical modelling. *Mineralogy and Petrology, 59*(1-2), 121-140.

Hansen, O., Gilding, D., Nazarian, B., Osdal, B., Ringrose, P., Kristoffersen, J.-B., Eiken, O., & Hansen, H. (2013). Snøhvit: the history of injecting and storing 1 Mt CO 2 in the Fluvial Tubåen Fm. *Energy Procedia, 37*, 3565-3573.

Hoffert, M. I., Caldeira, K., Benford, G., Criswell, D. R., Green, C., Herzog, H., Jain, A. K., Kheshgi, H. S., Lackner, K. S., & Lewis, J. S. (2002). Advanced technology paths to global climate stability: energy for a greenhouse planet. *science, 298*(5595), 981-987.

Hurter, S., Berge, J. G., & Labregere, D. (2007). *Simulations for CO2 injection projects with Compositional Simulator*.

Idso, S. B., Reginato, R. J., Jackson, R. D., Kimball, B. A., & Nakayama, F. S. (1974). The Three Stages of Drying of a Field Soil1. *Soil Science Society of America Journal, 38*(5), 831-837. doi: 10.2136/sssaj1974.03615995003800050037x

Jones, A. C., Arns, C. H., Hutmacher, D. W., Milthorpe, B. K., Sheppard, A. P., & Knackstedt, M. A. (2009). The correlation of pore morphology, interconnectivity and physical properties of 3D ceramic scaffolds with bone ingrowth. *Biomaterials, 30*(7), 1440-1451.

Knackstedt, M., Arns, C., Ghous, A., Sakellariou, A., Senden, T., Sheppard, A., Sok, R., Averdunk, H., Pinczewski, W. V., & Padhy, G. S. (2006). 3D imaging and flow characterization of the pore space of carbonate core samples.

Lanczos, C. (1950). *An iteration method for the solution of the eigenvalue problem of linear differential and integral operators*: United States Governm. Press Office Los Angeles, CA.

Laurindo, J. B., & Prat, M. (1996). Numerical and experimental network study of evaporation in capillary porous media. Phase distributions. *Chemical Engineering Science, 51*(23), 5171-5185. doi: http://dx.doi.org/10.1016/S0009-2509(96)00341-7

Laurindo, J. B., & Prat, M. (1998). Numerical and experimental network study of evaporation in capillary porous media. Drying rates. *Chemical Engineering Science, 53*(12), 2257-2269. doi: http://dx.doi.org/10.1016/S0009-2509(97)00348-5

Lehmann, P., Assouline, S., & Or, D. (2008). Characteristic lengths affecting evaporative drying of porous media. *Physical Review E, 77*(5), 056309.

Leung, D. Y. C., Caramanna, G., & Maroto-Valer, M. M. (2014). An overview of current status of carbon dioxide capture and storage technologies. *Renewable and Sustainable Energy Reviews, 39*, 426-443. doi: http://dx.doi.org/10.1016/j.rser.2014.07.093

Li, W. (1990). Mutual information functions versus correlation functions. *Journal of statistical physics, 60*(5-6), 823-837.

Lide, D. R. (2004). *CRC handbook of chemistry and physics* (Vol. 85): CRC press.

McPherson, B., & Lichtner, P. C. (2001). *CO2 sequestration in deep aquifers.* Paper presented at the Proceedings: first national conference on carbon sequestration, Washington, DC.

Metz, B., Davidson, O., de Coninck, H., Loos, M., Meyer, L., & Change, W. G. I. o. t. I. P. o. C. (2005). IPCC, 2005: IPCC special report on carbon dioxide capture and storage.

Moore, T. F., & Slobod, R. L. (1955). *Displacement of Oil by Water-Effect of Wettability, Rate, and Viscosity on Recovery*.

Morrow, N., Chatzis, I., & Taber, J. (1988). Entrapment and mobilization of residual oil in bead packs. *SPE Reservoir Engineering, 3*(03), 927-934.

Muller, N., Qi, R., Mackie, E., Pruess, K., & Blunt, M. J. (2009). CO2 injection impairment due to halite precipitation. *Energy Procedia, 1*(1), 3507-3514.

Nachshon, U., Shahraeeni, E., Or, D., Dragila, M., & Weisbrod, N. (2011b). Infrared thermography of evaporative fluxes and dynamics of salt deposition on heterogeneous porous surfaces. *Water Resources Research, 47*(12), n/a-n/a. doi: 10.1029/2011WR010776

Nachshon, U., Weisbrod, N., Dragila, M. I., & Grader, A. (2011a). Combined evaporation and salt precipitation in homogeneous and heterogeneous porous media. *Water Resources Research, 47*(3), n/a-n/a. doi: 10.1029/2010WR009677

Norouzi Rad, M., & Shokri, N. (2012). Nonlinear effects of salt concentrations on evaporation from porous media. *Geophysical Research Letters, 39*(4), n/a-n/a. doi: 10.1029/2011GL050763

Norouzi Rad, M., Shokri, N., & Sahimi, M. (2013). Pore-scale dynamics of salt precipitation in drying porous media. *Physical Review E, 88*(3), 032404.

Or, D., Lehmann, P., Shahraeeni, E., & Shokri, N. (2013). Advances in Soil Evaporation Physics—A Review. *Vadose Zone Journal, 12*(4). doi: 10.2136/vzj2012.0163

Orr Jr, F. M. (2004). Storage of carbon dioxide in geologic formations. *Journal of Petroleum Technology, 56*(09), 90-97.

Ott, H., de Kloe, K., van Bakel, M., Vos, F., van Pelt, A., Legerstee, P., Bauer, A., Eide, K., van der Linden, A., Berg, S., & Makurat, A. (2012). Core-flood experiment for transport of reactive fluids in rocks. *Review of Scientific Instruments, 83*(8), 084501. doi: doi:http://dx.doi.org/10.1063/1.4746997

Ott, H., & Oedai, S. (2015). Wormhole formation and compact dissolution in single- and two-phase CO2-brine injections. *Geophysical Research Letters, 42*(7), 2270-2276.

Ott, H., Roels, S. M., & de Kloe, K. (2015). Salt precipitation due to supercritical gas injection: I. Capillary-driven flow in unimodal sandstone. *International journal of greenhouse gas control, 43*, 247-255. doi: http://dx.doi.org/10.1016/j.ijggc.2015.01.005

Perona, P., & Malik, J. (1990). Scale-space and edge detection using anisotropic diffusion. *IEEE Transactions on pattern analysis and machine intelligence, 12*(7), 629-639.

Peysson, Y., Andre, L., & Azaroual, M. (2014). Well injectivity during CO 2 storage operations in deep saline aquifers—Part 1: Experimental investigation of drying effects, salt precipitation and capillary forces. *International journal of greenhouse gas control, 22*, 291-300.

Peysson, Y., Fleury, M., & Blázquez-Pascual, V. (2011). Drying Rate Measurements in Convection- and Diffusion-Driven Conditions on a Shaly Sandstone Using

Nuclear Magnetic Resonance. *Transport in Porous Media, 90*(3), 1001-1016. doi: 10.1007/s11242-011-9829-3

Philip, J. R. (1957). EVAPORATION, AND MOISTURE AND HEAT FIELDS IN THE SOIL. *Journal of Meteorology, 14*(4), 354-366. doi: doi:10.1175/1520-0469(1957)014<0354:EAMAHF>2.0.CO;2

Porter, M. L., & Wildenschild, D. (2010). Image analysis algorithms for estimating porous media multiphase flow variables from computed microtomography data: a validation study. *Computational Geosciences, 14*(1), 15-30.

Pruess, K., & García, J. (2002). Multiphase flow dynamics during CO2 disposal into saline aquifers. *Environmental Geology, 42*(2), 282-295. doi: 10.1007/s00254-001-0498-3

Pruess, K., & Müller, N. (2009). Formation dry-out from CO2 injection into saline aquifers: 1. Effects of solids precipitation and their mitigation. *Water Resources Research, 45*(3).

Questiaux, J. M., Couples, G. D., & Ruby, N. (2010). Fractured reservoirs with fracture corridors. *Geophysical Prospecting, 58*(2), 279-295.

Reichle, D., Houghton, J., Kane, B., & Ekmann, J. (1999). Carbon sequestration research and development: Oak Ridge National Lab., TN (US); National Energy Technology Lab., Pittsburgh, PA (US); National Energy Technology Lab., Morgantown, WV (US).

Roels, S. M., El Chatib, N., Nicolaides, C., & Zitha, P. L. J. (2016). Capillary-Driven Transport of Dissolved Salt to the Drying Zone During $$\hbox {CO}_{2}$$ CO 2 Injection in Homogeneous and Layered Porous Media. *Transport in Porous Media, 111*(2), 411-424. doi: 10.1007/s11242-015-0601-y

Roels, S. M., Ott, H., & Zitha, P. L. J. (2014). μ-CT analysis and numerical simulation of drying effects of CO2 injection into brine-saturated porous media. *International journal of greenhouse gas control, 27*, 146-154. doi: http://dx.doi.org/10.1016/j.ijggc.2014.05.010

Scherer, G. W. (2004). Stress from crystallization of salt. *Cement and Concrete Research, 34*(9), 1613-1624. doi: http://dx.doi.org/10.1016/j.cemconres.2003.12.034

Sghaier, N., & Prat, M. (2009). Effect of Efflorescence Formation on Drying Kinetics of Porous Media. *Transport in Porous Media, 80*(3), 441. doi: 10.1007/s11242-009-9373-6

Sghaier, N., Prat, M., & Nasrallah, S. B. (2007). On Ions Transport during Drying in a Porous Medium. *Transport in Porous Media, 67*(2), 243-274. doi: 10.1007/s11242-006-9007-1

Shah, S., Gray, F., Crawshaw, J., & Boek, E. (2015). Micro-computed tomography pore-scale study of flow in porous media: Effect of voxel resolution. *Advances in Water Resources*.

Shahidzadeh-Bonn, N., Rafaı, S., Bonn, D., & Wegdam, G. (2008). Salt crystallization during evaporation: impact of interfacial properties. *Langmuir, 24*(16), 8599-8605.

Sheppard, A. P., Sok, R. M., & Averdunk, H. (2004). Techniques for image enhancement and segmentation of tomographic images of porous materials. *Physica A: Statistical mechanics and its applications, 339*(1), 145-151.

Sherwood, T. K. (1930). The Drying of Solids—III1 Mechanism of the Drying of Pulp and Paper. *Industrial & Engineering Chemistry, 22*(2), 132-136. doi: 10.1021/ie50242a009

Shokri, N. (2014). Pore-scale dynamics of salt transport and distribution in drying

porous media. *Physics of Fluids, 26*(1), 012106. doi: doi:http://dx.doi.org/10.1063/1.4861755

Shokri, N., Lehmann, P., & Or, D. (2009a). Critical evaluation of enhancement factors for vapor transport through unsaturated porous media. *Water Resources Research, 45*(10), n/a-n/a. doi: 10.1029/2009WR007769

Shokri, N., Lehmann, P., & Or, D. (2009b). Characteristics of evaporation from partially wettable porous media. *Water Resources Research, 45*(2), n/a-n/a. doi: 10.1029/2008WR007185

Shokri, N., Lehmann, P., & Or, D. (2010a). Liquid-phase continuity and solute concentration dynamics during evaporation from porous media: Pore-scale processes near vaporization surface. *Physical Review E, 81*(4), 046308.

Shokri, N., Lehmann, P., & Or, D. (2010b). Evaporation from layered porous media. *Journal of Geophysical Research: Solid Earth, 115*(B6), n/a-n/a. doi: 10.1029/2009JB006743

Shokri, N., Lehmann, P., Vontobel, P., & Or, D. (2008b). Drying front and water content dynamics during evaporation from sand delineated by neutron radiography. *Water Resources Research, 44*(6), n/a-n/a. doi: 10.1029/2007WR006385

Shokri, N., & Or, D. (2011). What determines drying rates at the onset of diffusion controlled stage-2 evaporation from porous media? *Water Resources Research, 47*(9), n/a-n/a. doi: 10.1029/2010WR010284

Shokri, N., Sahimi, M., & Or, D. (2012). Morphology, propagation dynamics and scaling characteristics of drying fronts in porous media. *Geophysical Research Letters, 39*(9), n/a-n/a. doi: 10.1029/2012GL051506

Solomon, S., Qin, D., Manning, M., Chen, Z., Marquis, M., Averyt, K., Tignor, M., & Miller, H. (2007). Contribution of working group I to the fourth assessment report of the intergovernmental panel on climate change, 2007.

Stephanie, V.-T., Manuel, M., & Marc, P. (2012). Salt crystallisation at the surface of a heterogeneous porous medium. *EPL (Europhysics Letters), 98*(3), 34005.

Taber, J. (1969). Dynamic and static forces required to remove a discontinuous oil phase from porous media containing both oil and water. *Society of Petroleum Engineers Journal, 9*(01), 3-12.

Tans, P., & Keeling, R. (2010). Noaa/esrl. *Retrieved January, 30*, 2011.

Valvatne, P. H., & Blunt, M. J. (2004). Predictive pore-scale modeling of two-phase flow in mixed wet media. *Water Resources Research, 40*(7).

Van Brakel, J. (1980). Mass transfer in convective drying.

Veran-Tissoires, S., & Prat, M. (2014). Evaporation of a sodium chloride solution from a saturated porous medium with efflorescence formation. *Journal of Fluid Mechanics, 749*, 701-749. doi: 10.1017/jfm.2014.247

Verma, A., & Pruess, K. (1988). Thermohydrological conditions and silica redistribution near high-level nuclear wastes emplaced in saturated geological formations. *Journal of Geophysical Research: Solid Earth, 93*(B2), 1159-1173. doi: 10.1029/JB093iB02p01159

Walters, R. H., Bhatnagar, B., Tchessalov, S., Izutsu, K.-I., Tsumoto, K., & Ohtake, S. (2014). Next Generation Drying Technologies for Pharmaceutical Applications. *Journal of Pharmaceutical Sciences, 103*(9), 2673-2695. doi: http://dx.doi.org/10.1002/jps.23998

Wennberg, O. P., Malm, O., Needham, T., Edwards, E., Ottesen, S., Karlsen, F., Rennan, L., & Knipe, R. (2008). On the occurrence and formation of open fractures in the Jurassic reservoir sandstones of the Snøhvit Field, SW

Barents Sea. *Petroleum Geoscience, 14*(2), 139-150.

Wigley, T. M., Richels, R., & Edmonds, J. A. (1996). Economic and environmental choices in the stabilization of atmospheric CO2 concentrations.

Wollenweber, J., a Alles, S., Kronimus, A., Busch, A., Stanjek, H., & Krooss, B. M. (2009). Caprock and overburden processes in geological CO 2 storage: An experimental study on sealing efficiency and mineral alterations. *Energy Procedia, 1*(1), 3469-3476.

Yang, J., & Boek, E. S. (2013). A comparison study of multi-component Lattice Boltzmann models for flow in porous media applications. *Computers & Mathematics with Applications, 65*(6), 882-890.

Yiotis, A. G., Salin, D., Tajer, E. S., & Yortsos, Y. C. (2012). Analytical solutions of drying in porous media for gravity-stabilized fronts. *Physical Review E, 85*(4), 046308. doi: 10.1103/PhysRevE.85.046308

Yiotis, A. G., Tsimpanogiannis, I. N., Stubos, A. K., & Yortsos, Y. C. (2006). Pore-network study of the characteristic periods in the drying of porous materials. *Journal of Colloid and Interface Science, 297*(2), 738-748. doi: http://dx.doi.org/10.1016/j.jcis.2005.11.043

Zhao, P., Ge, S., Ma, D., Areeprasert, C., & Yoshikawa, K. (2014). Effect of Hydrothermal Pretreatment on Convective Drying Characteristics of Paper Sludge. *ACS Sustainable Chemistry & Engineering, 2*(4), 665-671. doi: 10.1021/sc4003505